VILNIUS UNIVERSITY

CENTER FOR PHYSICAL SCIENCE AND TECHNOLOGY

Irmantas Ratas

Algorithms for inhibition and desynchronization of neural systems

Doctoral dissertation

Physical sciences
Physics (02P)

Vilnius, 2015

The doctoral disertation is prepared in 2011–2015 at the Center for Physical Sciences and Technology

Scientific supervisor:

Prof. habil. dr. Kęstutis Pyragas (Center for Physical Sciences and Technology, physical sciences, physics – 02P, semiconductor physics – P265)

VILNIAUS UNIVERSITETAS

FIZINIŲ IR TECHNOLOGIJOS MOKSLŲ CENTRAS

Irmantas Ratas

Neuroninių sistemų slopinimo ir desinchronizavimo algoritmai

Daktaro disertacija

Fiziniai mokslai
Fizika (02P)

Vilnius, 2015

Daktaro disertacija rengta 2011–2015 metais Fizinių ir technologijos mokslų centro Puslaidininkių fizikos institute

Mokslinis vadovas:

prof. habil. dr. Kęstutis Pyragas (Fizinių ir technologijos mokslų centras, fiziniai mokslai, fizika – 02P)

Contents

Introduction

This dissertation deals with excitable and oscillatory neural systems. Although we use simplified mathematical models for real neural networks, we believe that the new insights made in this thesis might lead to novel therapeutic approaches in neuroscience.

Neurons are cells which are able to communicate between themselves through electrical and chemical signals. A prominent feature of neural activity is oscillations. Through the electrical and chemical interaction, neurons tend to synchronize their rhythms and approach a coherent behaviour. On the one hand synchronous neural behaviour relates with such crucial brain functions as vision, memory and movement coordination, while on other hand pathological synchronization may lead to epileptic seizures, essential tremor or symptoms of the Parkinson's disease.

Note that the synchrony is not only inherent for the neural systems. Groups of blinking fireflies or seduction dances of fiddler crabs reveals the visual beauty of synchronization, while in other physical systems it is not so obvious. The swaying of a bridge leading to the coherent pedestrian movement, like it happened for the London's Millennium bridge or the problem of power grid synchronization enforces engineers to interest in this phenomenon too. As it can be seen from the submitted examples, synchronization control is a relevant and significant topic.

In this dissertation, when we speak about synchronized system we usually have in mind a system with a partial phase entrainment – the situation when the part of the oscillator's phases are bounded within a fixed length. Our goal is to switch the system from the coherent (synchronized) to the incoherent (desynchronized) state, while in general the notion of synchronization control may include the inverse process as well. In the thesis, we analyse the systems by the methods of nonlinear dynamics. There is a number of powerful methods developed in the field of nonlinear dynamics, for example, the phase reduction or normal forms theories. Using these methods various complicated mathematical models can be reduced to a simple universal equations.

At the early stages of Parkinson's disease, undesired synchronous neural activity may be suppressed by pharmacological therapy, but as the illness evolves efficacy of this treatment rapidly decreases. At this stage some patients find an alternative in electrical deep brain stimulation – a procedure, when high-frequency (compared to neural cycles) electrical pulses are delivered to specific brain areas through implanted electrodes. Despite long and successful history of using of the deep brain stimulation its mechanisms are still not fully understood. Here we investigate some effects of the high-frequency stimulation on the neurons.

High-frequency deep brain stimulation is a non-feedback control method. It was observed that its efficacy varies from patient to patient and, moreover, decreases with time. Control signal continuously acts on tissues independently of patient's state, not only shortening the stimulator's battery life but also increasing the probability to damage the tissues. Therefore, there is a great interest in designing a control algorithm with feedback. The main advantages of the feedback versus non-feedback control are as follows. The feedback reduces sensitivity to parameter's variations, it does not require detailed knowledge of the system's model and one of the most important point is that it allows a noninvasive design, in the sense that the control force may vanish when the targeted state is reached.

As the brain is a vital organ, an extreme precaution of the possible interventions must be taken into account. First of all, the acting on the cells are imposed by several restrictions: i) the amplitude of applied current can not exceed a particular range, ii) applied current should not accumulate charge in the cell – this is the charge balance requirement. Moreover, only one variable, the membrane potential, can be measured, thus the full state of the system is not known. In neural network the knowledge about the system is yet more reduced as only mean field potential generated by several neurons membranes can be measured. Bellow, these restrictions will be discussed in more details, when desynchronization algorithms will be presented.

The main goals of the research work

1. To adopt the averaging and other singular perturbation methods for high-frequency stimulated neurons.

2. To investigate an influence of high-frequency stimulation on pulse propagation in the unmyelinated and myelinated neurons.

3. To develop an act-and-wait control algorithm for the stabilization of an

incoherent state in oscillatory network.

4. To analyze control strategies for elimination of synchronization in bistable networks.

Scientific novelty

1. Exploiting the averaging method and geometrical singular perturbation theory, the main characteristics of the traveling pulse in the FitzHugh-Nagumo unmyelinated axon under the action of high-frequency stimulation are derived in an analytical form. It is shown that the effect of high-frequency stimulation on the axon is determined by the parameter equal to the ratio of the amplitude to the frequency of the stimulation current. There is a critical threshold of this parameter at which the pulse stops to propagate.

2. The effect of a homogeneous high-frequency stimulation on a one-dimensional chain of coupled excitable elements governed by the FitzHugh-Nagumo equations (model of a myelinated axon) is analyzed. It is shown that, depending on the amplitude, the high-frequency stimulation may either suppress or enhance the pulse propagation through the axon. This differs essentially from the case of unmyelinated axons described by spatially continuous FitzHugh-Nagumo equations, where the high-frequency stimulation can cause only suppression.

3. The act-and-wait control algorithm is proposed to suppress synchrony in globally coupled oscillatory networks in the situation when the simultaneous registration and stimulation of the system is not possible. The efficacy of the algorithm is demonstrated analytically and numerically for globally coupled Stuart-Landau oscillators as well as synaptically coupled FitzHugh-Nagumo and Hodgkin-Huxley neurons.

4. The problem of controlling synchrony in bistable networks, which possess coherent and incoherent attractors in a certain range of parameters, is analyzed. The act-and-wait as well as the multisite coordinated reset stimulation algorithms are proposed in order to switch the bistable networks from the stable coherent state to the stable incoherent state.

Scientific statements

1. In the limit of high frequencies, the threshold amplitude, that prevents the pulse propagation in myelinated and unmyelinated axons, increases linearly with the frequency of stimulation current.

2. The excitability threshold of a neuron can be efficiently controlled by a high-frequency stimulation current. As a result, the high intensity stimulations suppress the pulse propagation in the myelinated and unmyelinated axons, while the low intensities may enhance the pulse propagation in the myelinated axons.

3. The act-and-wait control algorithm can efficiently stabilize the incoherent state in monostable oscillatory networks with the constraints typical for real-world neural networks.

4. The act-and-wait as well as multisite coordinated reset stimulation methods are able to switch the bistable oscillatory networks from the stable coherent to the stable incoherent states. The second algorithm works even for the networks with the complex scale-free topology.

Structure of the work

Chapter 1 provides an introduction to the neuron models and neural networks, as well as introduces the definitions. Also a survey of the literature is presented.

Chapter 2 describes the averaging method and its application for the analysis of the pulse propagation in high-frequency stimulated continuous and discrete excitable media.

Chapter 3 presents the application of act-and-wait control algorithm for the stabilization of the incoherent state in various oscillatory networks.

Chapter 4 considers the control of synchronization in bistable oscillatory networks. Two different algorithms to switch the bistable networks from the stable coherent state to the stable incoherent states are analyzed.

List of publications

Scientific papers

[A1] I. Ratas and K. Pyragas, Effect of high-frequency stimulation on nerve pulse propagation in the FitzHugh–Nagumo model, *Nonlinear Dyn.* **67**, 2899-2908 (2012)

[A2] I. Ratas and K. Pyragas, Pulse propagation and failure in the discrete FitzHugh-Nagumo model subject to high-frequency stimulation, *Phys. Rev. E* **86**, 046211 (2012)

[A3] I. Ratas and K. Pyragas, Controlling synchrony in oscillatory networks via an act-and-wait algorithm, *Phys. Rev. E* **90**, 032914 (2014)

[A4] I. Ratas and K. Pyragas, Eliminating synchronization in bistable networks, *Nonlinear Dyn.*, DOI:10.1007/s11071-015-2393-6

International conferences[1]

[A5] I. Ratas, K. Pyragas, Desynchronization of oscillatory networks by intermittent delayed feedback control, *The 5th International Conference (CHAOS 2012) on Chaotic modelling, Simulation and Applications (Athens, 2012.06.12-15). Book of Abstracts,* p. 131 (oral presentation)

[A6] I. Ratas, K. Pyragas, Enhancement and suppression of pulse propagation in a discrete FitzHugh-Nagumo model subjected to a high-frequency stimulation, *XXXII Dynamic Days Europe (Gothenburg, 2012.09.2-7). Book of Abstracts*, p. 216 (poster)

[A7] I. Ratas, K. Pyragas, Application of act and wait control to oscillatory network desynchronization, *XXXIII Dynamic Days Europe (Madrid, 2013.07.3-7). Book of Abstracts*, p. 251 (oral presentation)

[A8] I. Ratas, K. Pyragas, Search for optimal signals to suppress synchronization in oscillatory networks, *8th European Nonlinear Dynamics Conference (Vienna, 2014.07.6-11). Proceedings of 8th European Nonlinear Dynamics Conference* (oral presentation)

[1] Presented by the first author in the list

[A9] I. Ratas, K. Pyragas, Control of synchronization bistability in oscillatory networks, *XXXIV Dynamic Days Europe (Bayreuth, 2014.09.8-12). Book of Abstracts*, p. 158 (oral presentation)

[A10] K. Pyragas, I. Ratas, Controlling synchrony in oscillatory networks via act-and-wait algorithm, *XXXIV Dynamic Days Europe (Bayreuth, 2014.09.8-12). Book of Abstracts*, p. 157

[A11] K. Pyragas, I. Ratas, Cancelling synchronization in bistable oscillatory networks, *The 8th International Conference (CHAOS 2015) on Chaotic modelling and Simulation (Paris, 2015.05.26-29). Book of Abstracts,* p. 108

Local conferences

[A12] I. Ratas and K. Pyragas, Aukštadažnės stimuliacijos poveikis Fitzhugh-Nagumo modelio neuronui, *39-oji Lietuvos nacionalinė fizikos konferencija (Vilnius, 2011.10.6-8). Programa ir pranešimų tezės,* p. 118 (poster)

[A13] I. Ratas and K. Pyragas, Desinchronizacijos signalo optimizavimas, *40-oji Lietuvos nacionalinė fizikos konferencija (Vilnius, 2013.06.10-12). Programa ir pranešimų tezės,* p. 122 (poster)

[A14] I. Ratas and K. Pyragas, Sinchronizacijos valdymas bistabiliuose osciliatorių tinkluose, *41-oji Lietuvos nacionalinė fizikos konferencija (Vilnius, 2015.06.17-19). Programa ir pranešimų tezės,* p. 360 (poster)

Personal contribution of the author

Author of the thesis has performed most of the analytical derivations of the equations as well as numerical simulations.

Acknowledgements

My sincere gratitude goes to my supervisor, Prof. Habil. Dr. Kęstutis Pyragas, for his patience, numerous helpful discussions, suggestions and for invaluable guidance throughout these years.

I am very grateful to my colleague Dr. Viktoras Novičenko for great discussions, which have broadened my knowledge, as well as for all the funny and relaxed moments we shared.

Also I would like to express my appreciation to Aloyzas Lukavičius, my teacher of physics. His enthusiasm and support inspired me to get interested in physics.

Finally, I would like to thank my family and friends for their encouragement and support during the time I worked on this dissertation.

1. Neurons, neural systems and synchrony

The purpose of this chapter is to familiarize the reader with methodology and terminology of the problem investigated in the thesis and to overview the literature of the relevant research field. In Sec. 1.1 a short introduction to neurons and neural network models used in the thesis is presented. Section 1.2 is dedicated to phase oscillators, a paradigmatic model in the field of the research on coupled oscillators behaviour. Here we also give the definition of the synchronization. In Sec. 1.3 the problem of pathological neurons synchronization is discussed. The currently accessible treatment of the synchronization related diseases as well as the treatment improvements are presented.

1.1 Modelling of neurons and neural systems

Single cell: Neuron is a cell, which main feature is an electrical excitability. Due to cell's structure it is able to generate and broadcast electrochemical signals. Despite the fact that there exist different types and shapes of the neurons, a typical neuron (see Fig. 1.1) consists of the following parts [1]:

- *Soma* – it accommodates nucleus and is the main part of the cell.
- *Dendrites* – they form a tree-shaped structure, with their trunks directed towards the soma. Dendrites act as receivers, as they collect signals from other neurons, which later can effect the transmembrane potential of the initial axons segment.
- *Axon* – acts as a transmitter, which conducts a signal generated at the joining point of the soma and axon. The axon usually has the same diameter across its length while eventually branches in a tree-like manner, allowing the impulse train on the trunk to be directed toward a variety of locations

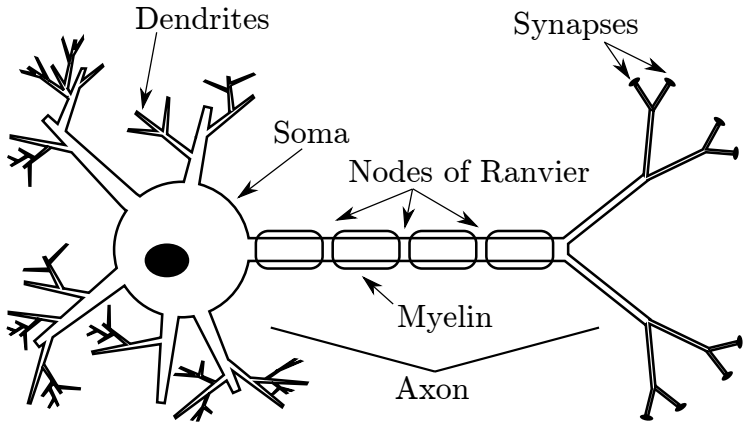

Figure 1.1: Schematic drawing of the neuron.

on muscle cells or other neurons [1]. The walls of the axon have molecular structures, which for particular ions acts as pumps or gates, i.e. it regulates ions concentrations between inner and outer sides of the neuron in this way also regulating difference of the electric potential. Some axons are covered by insulating material called *myelin*. Myelin covers axon not continuously but with some gaps called *Ranvier nodes*. Such structure of the axon allows to increase the speed of travelling pulses.

- *Synapses* – inject electric pulses into the dendrites or the cell body of other neurons. In terms of neuroscince, the cell that is sending the signal is called the *presynaptic neuron* and the cell that is receiving the signal is called the *postsynaptic neuron*. According to injecting material type synapses can be divided in two categories: i) *Chemical synapse* – electrical activity in the presynaptic neuron releases molecules called neurotransmitters. The neurotransmitters in postsynaptic neurons dendrites opens ion channels what induce an electrical current; ii) *Electrical synapse* – neurons are connected by special junctions which enables to flow electric current from one cell to another directly. Although the first one synapses are more common in the brain, the second one ensure a faster signal transfer.

The modelling of neural processes is not a trivial task as the neuron is an intricate dynamic system that should be described on several length scales [1] ranging from few nanometres to centimetres. This statement can be illustrated by the following chain, where different subsystems of neuron dynamics are laid by the order of increasing size: **Biomolecural dynamics → Patches of nerve membrane → Synapses → Axonal and dendritic fibers → Branching regions of fibers → Neuron**. The size difference between the biomolecules and

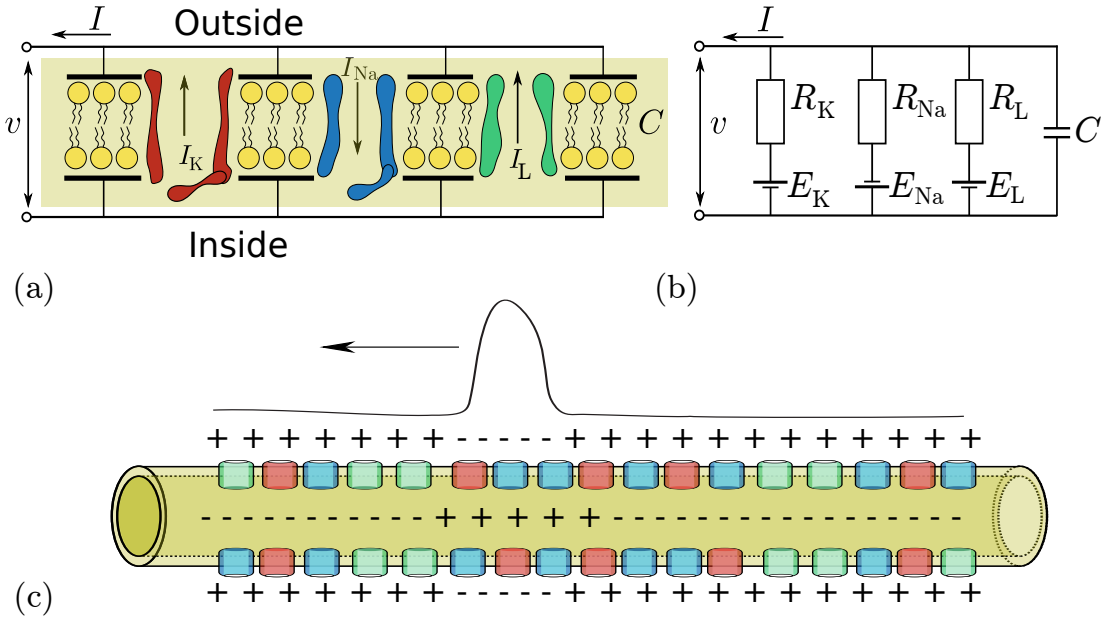

Figure 1.2: (a) Schematic drawing of the neurons membrane patch. Red, blue and green structures represents K^+ and Na^+ ion channels and other possible leakage sources respectively; (b) Circuit analogue of the neurons membrane; (c) The propagation of the ions concentration disturbance in the axon.

neuron is comparable to that between a saucer and the diameter of the continent of Europe [2]. However, one would typically not exclusively ascribe processes that happen on the length scale of Europe (e.g.tectonic plate movement) to objects of the size of a saucer. But this is what happens in the models for nerve pulse propagation.

In 1952, Hodgkin and Huxley wrote a series of papers where they determined the laws of the ions movement in the nerve cell by experimenting with a squid axon. In the final paper [3] they submitted a mathematical model. They were able to create a circuit model that seemed to match how the squid axon membrane responded to various stimulus. Here we will represent the main ideas behind the Hodgkin-Huxley (HH) model, later we will give its detailed description and finally the FitzHugh-Nagumo simplification will be presented.

The axons membrane is considered as a capacitor that becomes transiently charged and discharged via the local voltage changes. These changes are conditioned by the ions flow through ion's channel (see Fig. 1.2). Under favourable circumstances the local membrane excitation leads to a cascade effect, where excited membrane part induce voltage change in neighbour medium allowing the pulse of voltage change propagation (see Fig. 1.2c).

According to Hodgkin and Huxley [3] the dynamics of the membrane potential in axon is proportional to the sum of currents generated by Na^+, K^+ ions and leakage:

$$C\frac{\partial v}{\partial t} = -I_{\mathrm{Na}} - I_{\mathrm{K}} - I_{\mathrm{L}} + D\frac{\partial^2 v}{\partial x^2}. \tag{1.1}$$

Here v is the membrane potential, C is the membrane capacity and the last term appears due to diffusion. The currents generated by ions can be expressed as

$$I_{\mathrm{Na,K,L}} = \bar{g}_{\mathrm{Na,K,L}}(v - v_{\mathrm{Na,K,L}}) \tag{1.2}$$

where $\bar{g}_{\mathrm{Na,K,L}}$ are conductances and $v_{\mathrm{Na,K,L}}$ are the rest membrane potentials created by the given ions. The conductances $\bar{g}_{\mathrm{Na,K}}$ depend on the probabilities $p_{\mathrm{Na,K}}$ that the Na^+ or K^+ ion gates would be open. The dynamics of the probabilities $p_{\mathrm{Na,K}}$ are governed by kinetic equations:

$$\frac{\mathrm{d}p^{(i)}}{\mathrm{d}t} = \alpha_i(v)(1 - p^{(i)}) - \beta_i(v)p^{(i)}, \tag{1.3}$$

where i can stand for Na or K. The factors $\alpha_i(v)$ and $\beta_i(v)$ are called the *transition rate constants*. The variable $\alpha_i(v)$ is the number of times per second that a gate which is in the shut state opens, while $\beta_i(v)$ represents the number of times per second that a gate in the open state shuts. If at the given moment there is a portion $p^{(i)}$ of ith type open gates, then at this moment the fraction of shutting gates is equal to the product $\beta_i p^{(i)}$, while the fraction of the opening gates will be equal to $\alpha_i(1 - p^{(i)})$.

Each ion channel may have a several different kind of the ion gates, thus the conductances $\bar{g}_{\mathrm{Na,K}}$ will be proportional (with assumption that each gate operates independently) to the product of the probabilities $p_{\mathrm{Na,K}}$. If the conductances $\bar{g}_{\mathrm{Na,K}}$ would be constants then dynamics of the membrane potential would be boring, because after perturbation it will exponentially return to the rest point. But since $\bar{g}_{\mathrm{Na,K}}$ can change, the actual system dynamics is determined by probabilities $p_{\mathrm{Na,K}}$ [1].

In the myelinated axons, the diffusion component becomes discrete as the active media (uncovered ion's channels) are placed just at the Ranvier nodes [1]:

$$C\frac{\mathrm{d}v_n}{\mathrm{d}t} = F(v_n, p_n^{(i)}) + D\left(v_{n+1} + v_{n-1} - 2v_n\right). \tag{1.4}$$

The given equation describes the potential of n-th Ranvier node. The function $F(v_n, p_n^{(i)})$ includes currents generated by the ions, which are the same as

in Eq. (1.1).

Hodgkin-Huxley neuron model: After the consideration of the principles of neuron model construction, we present a model described by the Hodgkin–Huxley equations [3]:

$$
\begin{aligned}
C\dot{v} &= -g_{Na}m^3h(v-v_{Na}) - g_K n^4(v-v_K) - g_L(v-v_L) + I, && \text{(1.5a)}\\
\dot{m} &= \alpha_m(v)(1-m) - \beta_m(v)m, && \text{(1.5b)}\\
\dot{h} &= \alpha_h(v)(1-h) - \beta_h(v)h, && \text{(1.5c)}\\
\dot{n} &= \alpha_n(v)(1-n) - \beta_n(v)n. && \text{(1.5d)}
\end{aligned}
$$

Here due to simplification only the local model of membrane potential is presented, i.e. the effect of diffusion is neglected. The overdot marks the time derivative $\dot{v} \equiv \mathrm{d}v/\mathrm{d}t$. Variable v is the membrane potential measured in mV. The standard values of the parameters that have been obtained by fitting this model to the experimental data on the giant axon of the squid [3] are: $C = 1\ \mu\mathrm{F/cm^2}$, $(v_L, v_K, v_{Na}) = (10.6, -12, 115)$ mV, $(g_L, g_K, g_{Na}) = (0.3, 36, 120)$ mS/cm^2.

As one can see from the product m^3h in the first member of equations (1.5a) right hand side, the flow of sodium ions is governed by four gates – three activation m and one inactivation h. Equivalently the conduction of potassium ions is governed by four single type gates, which dynamics are represented by variable n. The rate parameters defining the dynamics of the gating variables m, h and n are measured in ms^{-1} and are the following functions of the membrane potential:

$$
\begin{aligned}
\alpha_m(v) &= (2.5 - 0.1v)/\left[\exp(2.5 - 0.1v) - 1\right], && \text{(1.6a)}\\
\beta_m(v) &= 4\exp(-v/18), && \text{(1.6b)}\\
\alpha_h(v) &= 0.07\exp(-v/20), && \text{(1.6c)}\\
\beta_h(v) &= 1/\left[\exp(3 - 0.1v) + 1\right], && \text{(1.6d)}\\
\alpha_n(v) &= (0.1 - 0.01v)/\left[\exp(1 - 0.1v) - 1\right], && \text{(1.6e)}\\
\beta_n(v) &= 0.125\exp(-v/80). && \text{(1.6f)}
\end{aligned}
$$

The influence of external stimulation in this model is represented by current I. The voltage scale in this model is shifted in such a way that the membrane resting potential (i.e., the steady state value of the membrane potential) without external stimulation $I = 0$ is zero.

If neuron is not effected by constant external current, i.e. $I = 0$, then it is in excitable regime. Excitability is a system's ability to generate large responses

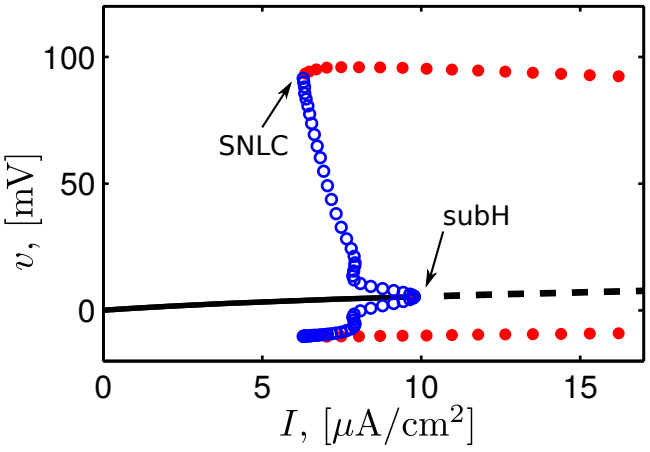

Figure 1.3: Bifurcation diagram of HH model described by (1.5) equations. Continuous line shows value of stable, dashed line – unstable rest points. Solid and hollowed circles represents minimal and maximal values of potential for stable and unstable limit cycles respectively. Abbreviations "subH" means subcritical Hopf bifurcation, "SNLC" – saddle node bifurcation of limit cycle.

compared to a small stimulations. For the neurons this property means that they can generate high amplitude electrical impulse in response to small external perturbations. From the point of view of nonlinear dynamics, the excitable system is a system with a stable rest point and generated response is just consequence of the transient processes. Excitable systems have a threshold value, i.e. there exists some critical value of the external stimuli below which the response is small. In theoretical models this threshold can be defined precisely, while in real neurons it is not always possible, because only one variable, i.e. membrane potential, is measured. Due to the existence of the threshold value the excitable cells act as noise filters [4].

The constant external current I can control dynamical properties of the system. Illustration of this statement can be seen in bifurcation diagram in Fig. 1.3. Neuron has only one stable stationary point (in figure shown by continuous line), until current does not exceed 6.3μA/cm^2. At this value, the system undergoes saddle node bifurcation of limit cycle, thus stable and unstable limit cycles appears. Further increase of current values induce subcritical Hopf's bifurcation, when unstable limit cycle shrinks and collide with stable stationary point at $I \approx 9.8\mu$A/cm^2. After this bifurcation, stable stationary point become unstable, while unstable limit cycle disappears.

The HH neuron model defines biophysical processes in a cells membrane with four differential equations. Therefore, only projections of four-dimensional phase trajectories can be observed and a geometrical explanation of important biophys-

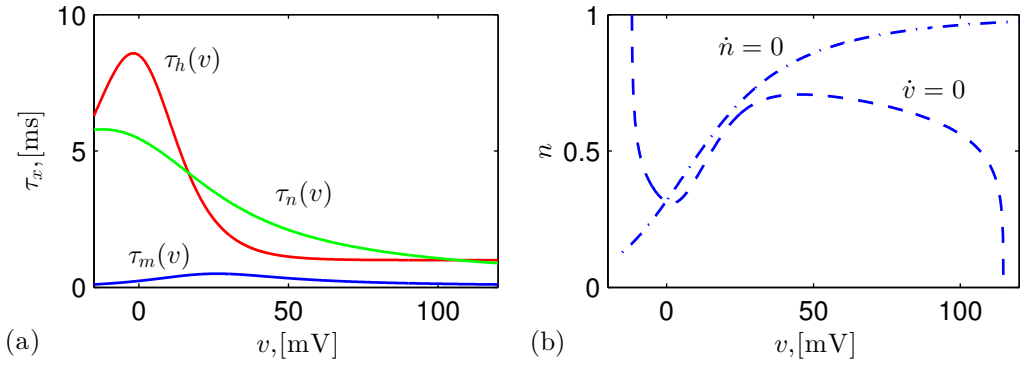

Figure 1.4: (a) The time constants $\tau_h(v)$, $\tau_n(v)$, $\tau_m(v)$ for HH model (1.5). (b) The isoclines of reduced slow-fast HH model.

ical phenomena is not available. It is useful to study systems of equations that are simpler than the Hodgkin-Huxley model, but retain many of their qualitative features.

The rates at which the dynamics of m, n and h variables evolves can be estimated by rewriting Eqs. (1.5b)–(1.5d) to the form of

$$\tau_x(v)\dot{x} = x_\infty(v) - x, \tag{1.7}$$

where the letter x stands for the gating variables m, n or h, the rate $\tau_x(v)$ can be calculated by $\tau_x(v) = 1/\left[\alpha_x(v) + \beta_x(v)\right]$. If the system had the constant potential v, then function $x_\infty(v)$ would represent the stationary value of the gating variable. Its value can be calculated according to $x_\infty(v) = \alpha_x(v)/\left[\alpha_x(v) + \beta_x(v)\right]$.

FitzHugh-Nagumo model: One of the most popular HH model simplification is FitzHugh-Nagumo (FHN) equations. This model isolates such mathematical properties as excitation and propagation from the electrochemical properties of sodium and potassium ion flow [5]. The idea behind construction of this model lies in observation that sodium activation variable m acts on much faster time scales than any others variable (see Fig. 1.4a) in Eqs. (1.5), thus it follows dynamics according to $m = m_\infty(v)$. Moreover, the sum of gating variables n and h remains approximately the same, $h(v) + n(v) \approx 0.8$. The reduction of the system (1.5) will contains one fast variable v and one slow variable n.

The nullclines of this slow-fast system is shown in Fig. 1.4b. It can be seen that the $\dot{v} = 0$ nullcline has a "cubic like" shape, while the $\dot{n} = 0$ nullcline for particular range can be approximated by linear function. Nullclines intersect just at one point. With these observations in mind the FitzHugh-Nagumo model for

dimensionless variables was constructed [6, 7]:

$$\dot{v} = v - v^3/3 - w + I, \tag{1.8a}$$

$$\dot{w} = \varepsilon(v + \beta - \gamma w). \tag{1.8b}$$

Here the variable v represents the membrane potential and w is called the recovery variable. The constant $\varepsilon > 0$ is the ratio between the characteristic time scales of v and w variables. Typical parameters set for this model is as follows: $\epsilon = 0.08$, $\beta = 0.7$, $\gamma = 0.8$.

The external influence is represented by current I. The given FHN model for the small values of I successfully mimics bifurcation diagram of HH case, i.e., it undergoes a saddle node bifurcation of a limit cycle and a subcritical Hopf bifurcation.

The "cubic like" $\dot{v} = 0$ nullcline could be approximated by other functions, like various types of piecewise functions. The choice of the cubic polynomial for Jin-Ichi Nagumo was more appropriate, because for equations (1.8) modelling he was using tunnel diodes. These diodes have a current-voltage curve similar to the cubic shape used in (1.8) equations [5].

Network of cells: The complex tasks like shape recognition, language processing are accomplished not by a single neuron, but by the neural network. For example, human brain has approximately 20 billion of neocortical neurons, that are responsible for our language. Typically the number of neuron junctions varies from 1000 to 10000, with an average of 7000 synaptic links [8]. The combinatorial possibility could give rise to enormously complex neuronal circuits or network topologies, which might be very difficult to understand. Moreover the network of the neurons is not static, it changes during the time due to neurons property called *synaptic plasticity* – a synapse's ability to strengthen or weaken connectivity dependently on its activity [9].

The dynamics of neural network is the result of three components [10]: i) The intrinsic properties of cells within the network; ii) The synaptic properties of connections between neurons; iii) The topology of network connectivity.

To simplify the modelling we will assume that neuron has no structure, i.e. it is a point. Then the dynamics of nth neuron is governed by the equation similar to (1.1) or (1.4)

$$C\frac{\mathrm{d}v_n}{\mathrm{d}t} = F(v, p_n^{(i)}) + I_{\mathrm{syn},n}. \tag{1.9}$$

The difference is that the diffusion term in Eqs. (1.9) is removed and an additional term is added, which represents the synaptic current I_{syn}. The same logic as for

currents generated by Na^+ or K^+ ions applies also for the synaptic current generated by the chemical synapses. It can be defined as the product of a conductance with a voltage difference [10]

$$I_{\text{syn},n} = g(t)(v_n - v_0). \tag{1.10}$$

Here conductance $g(t)$ depends on the presynaptic neuron and the potential v_0 is called reversal or Nernst potential as there is no net ions flow from one to another side of the membrane.

There are many ways to model the conductance $g(t)$. One of the most popular is to assume that conductance $g(t)$ is the sum of fixed functions, which depends only on the presynaptic neuron spiking time

$$g(t) = \tilde{g} \sum_j \alpha(t - t_k). \tag{1.11}$$

This definition of conductance leave us with possibility to choose from variety of alpha functions (delta functions, single or double exponential decays, etc.). However this approach is not related to the notion of voltage gated channels. Moreover, the tracking of the spiking times is needed, which can become a computational challenge for the bigger networks [10].

In a more realistic biological model the conductance $g(t)$ is defined as a product $g(t) = \tilde{g}s(t)$, where $\tilde{g}$ is the synaptic conductance maximum, $s(t)$ denotes the fraction of open channels in the dendrite and satisfy

$$\frac{\mathrm{d}s_n}{\mathrm{d}t} = \alpha_s(1 - s_n)H_\infty(v_j - v_T) - \beta_s s_n. \tag{1.12}$$

Here, α_s and β_s are the rates at which the synapse turns on and off, respectively. The function $H_\infty(v)$ represents the concentration of neurotransmitters, which was released from the jth presynaptic neuron to the nth postsynaptic neuron. This function usually is approximated by step-like functions, e.g. Heaviside or sigmoid. Finally, v_T is a threshold potential.

In this work, we suppose that the characteristic time of the synaptic variable $s(t)$ is much smaller than the characteristic period of the neuron self-oscillations. In this case the approximation $s_n \approx H_\infty(v_j - v_T)$ is valid.

The synaptic links according to interaction type are divided in two groups – *excitatory* and *inhibitory*. Excitatory interaction increases the probability that the postsynaptic cell will generate an action potential[1]. Inhibitory interaction

[1]The change in membrane potential occurring in nerve when excitation occurs.

acts contrary – it decreases the probability of the postsynaptic cell to generate an action potential. In most cases excitatory synapses tend to promote synchronous activity, while inhibitory synapses try to keep out-of-phase behaviour [10]. It is important that the ratio of inhibitory and excitatory interactions in the brain remains fixed whereas alternations may lead to brain malfunctioning [11].

If we take into account the network's topology the synaptic current generated by the nth neuron can be written as

$$I_{\mathrm{syn},n} = \tilde{g}(v_n - v_0) \sum_{j=1}^{N} a_{nj} H_\infty(v_j - v_T) \tag{1.13}$$

Here a_{nj} is the element of the adjacency matrix, which is equal to 1 if nth neuron is effected by the jth neuron and $a_{nj} = 0$ in other cases. Depending on the structure of the adjacency matrix one can generate networks with different topologies: global or local, dense or sparse, random or structured. In this thesis we assume one of the simplest and easiest tractable all-to-all coupling, i.e. $a_{nj} = 1$ for all $n \neq j$. Also the case of sparse random network will be analysed.

1.2 Introduction to phase oscillators and definition of synchronization

Oscillations are one of the possible neuron's activity patterns, which play an important role in brain functioning. It is necessary to note that neurons are not conservative systems, because they have energy source (which come from digested food) and undergo dissipation, also the amplitude, shape and period of oscillations is defined by neuron itself and cannot be changed by a weak perturbation. Therefore, when we are speaking about neuron as an oscillator we have in mind that it is a self-sustained oscillator. This section is dedicated to the investigation of general oscillators and oscillatory networks.

If we would couple several self-sustained oscillators with similar frequencies we can expect three things to happen [12]: i) oscillators can inhibit each other, thus oscillations would stop; ii) oscillations would become chaotic instead of being periodic; iii) oscillators can start to oscillate "synchronously" or in other words "sharing the same time". As the synchronization was described in Ref. [13] the oscillators adjusted their internal rhythms due to the interaction.

The self-sustained oscillators have an outstanding feature: they can be described by a single variable θ called *phase* [13–15]. Let's say that we have a

dynamical system defined by a M-dimensional state vector $\boldsymbol{x}$, which obeys ordinary differential equations

$$\dot{\boldsymbol{x}} = \boldsymbol{f}(\boldsymbol{x}). \tag{1.14}$$

Assume, that the system has a stable limit cycle solution $\boldsymbol{x}_c(t) = \boldsymbol{x}_c(t+T)$ with a period T. At the time $t = 0$ one can arbitrary choose point $\boldsymbol{x}(0) = \boldsymbol{x}_0$ on the limit cycle. Then the phase of $\boldsymbol{x}_c(t)$ is defined as $\theta = t \bmod T$. The initial point $\boldsymbol{x}_0$ can be chosen anywhere on the limit cycle, what introduces ambiguity in the definition of the phase. However the different choices of initial points in the definition of the phase, give only different constant shifts. To sum up, the phase θ is just an arbitrary measure, that shows oscillator's position on the limit cycle.

The notion of phase can be also introduced for the points in the phase space outside of the limit cycle. If the point $\boldsymbol{x}_1$ does not belong to the stable limit cycle $\boldsymbol{x}_c(t)$, then its phase is defined as follows. Since the limit cycle is stable the trajectory $\boldsymbol{x}(t)$ with the initial condition $\boldsymbol{x}(0) = \boldsymbol{x}_1$ reaches the point $\boldsymbol{x}_c(\bar{t})$ after $\bar{t} = nT \to +\infty$ with $n \in \mathbb{N}$. Then the phase of the point $\boldsymbol{x}_1$ is the same as the phase of the point $\boldsymbol{x}_c(\bar{t})$, i. e. $\theta(\boldsymbol{x}_1(0)) = \theta(\boldsymbol{x}_c(\bar{t}))$. The points in the M-dimensional phase space of the system having identical phases form $M-1$ dimension surfaces, which are referred to as *isochrons*.

An unperturbed oscillator's phase is governed by the simple differential equation

$$\dot{\theta} = 1. \tag{1.15}$$

It is convenient to renormalize phase change from the interval $[0; T]$ to $[0; 2\pi]$ in such case $\dot{\theta}$ would be equal to oscillators frequency ω. If the system (1.14) is perturbed by a weak time dependent force $\varepsilon \boldsymbol{p}(t) \ll 1$

$$\dot{\boldsymbol{x}} = \boldsymbol{f}(\boldsymbol{x}) + \varepsilon \boldsymbol{p}(t), \tag{1.16}$$

then its phase evolves according to

$$\dot{\theta} = \omega + \varepsilon \boldsymbol{Z}(\theta)\boldsymbol{p}(t) + o(\varepsilon), \tag{1.17}$$

where the function $\boldsymbol{Z}(\theta)$ is called a phase response curve. The function $\boldsymbol{Z}(\theta)$ contains all necessary information of the system to describe the phase dynamics of a weakly perturbed oscillator. The term $o(\varepsilon)$ represents error so that $o(\varepsilon)/\varepsilon \to 0$ as $\varepsilon \to 0$. For the sake of clarity, this term will be further omitted. The field in nonlinear dynamics which studies the transition from Eq. (1.14) to Eq. (1.17) is called the phase reduction theory. The details about this theory can be found in

Ref. [15].

The phase reduction theory is also applicable when the time dependent external force $\boldsymbol{p}(t)$ is replaced by the force generated by the other oscillator. Kuramoto [14] has shown that the phases of any weakly coupled systems of the nearly identical limit-cycle oscillators follow the rule

$$\dot{\theta}_i = \omega_i + \sum_{j=1}^{N} \Gamma_{ij}(\theta_j - \theta_i), \tag{1.18}$$

where index marks the number of an oscillator and the interaction functions $\Gamma_{ij}(\theta_j - \theta_i)$ can be estimated as integrals involving certain terms from the original limit-cycle model [14,16]. One can imagine the phase oscillators as balls moving on the circle and interacting between each other through force defined by $\Gamma_{ij}(\theta_j - \theta_i)$.

Let us say that we have N interacting oscillators, while each of them is described by M ordinary differential equations. The phase reduction theory allows us to reduce the initial system of NM differential equations to the system with only N equations. Although this procedure simplifies the problem, the analysis of equations (1.18) is still complicated. To specify the model, we first have to define the function $\Gamma_{ij}(\theta_j - \theta_i)$, which includes the knowledge about the topology and interaction.

One of the most popular, analytically tractable case is *Kuramoto model*, where oscillators are coupled all-to-all with the equal weight through the sine function

$$\Gamma_{ij}(\theta_j - \theta_i) = \frac{K}{N} \sin(\theta_j - \theta_i). \tag{1.19}$$

Equations (1.18)–(1.19) represents a paradigmatic model for the analysis of the synchronization of globally coupled oscillators.

Definitions of the synchronization. In order to find out the possible outcomes of oscillators coupling, let us start with a general model of two coupled phase oscillators

$$\dot{\theta_1} = \omega_1 + \Gamma_1(\theta_1 - \theta_2), \tag{1.20a}$$

$$\dot{\theta_2} = \omega_2 + \Gamma_2(\theta_2 - \theta_1). \tag{1.20b}$$

Since each phase variable is defined on the circle, the state space of coupled oscillators is a two-dimensional torus with θ_1 and θ_2 being latitude and longitude respectively, see Fig. 1.5. The trajectory of system's (1.20) solution dependently on the functions $\Gamma_{1,2}(\theta)$ and frequencies $\omega_{1,2}$ can be a closed curve or it can end-

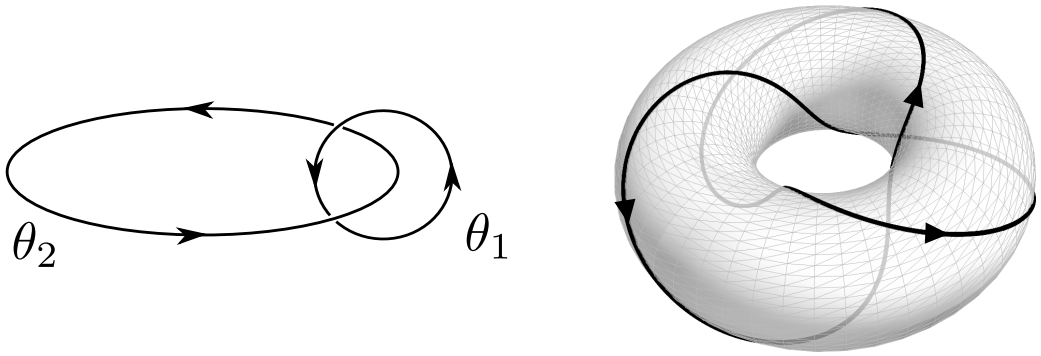

Figure 1.5: The dynamics of two phase oscillators can be represented on the two-dimensional torus.

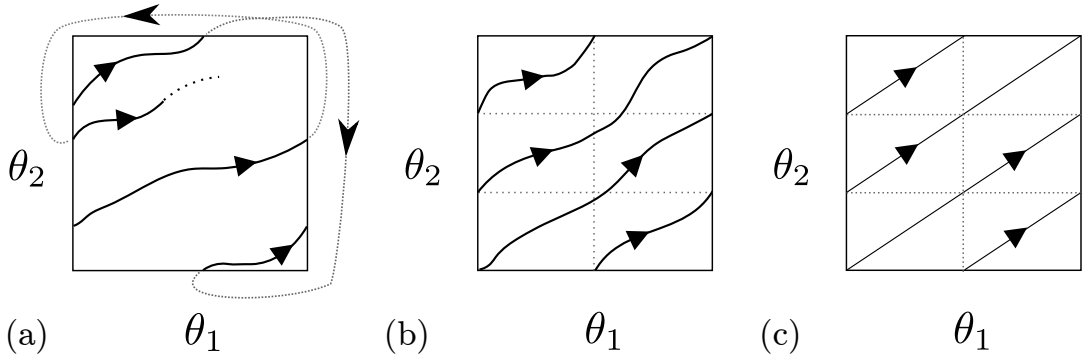

Figure 1.6: The two-dimensional torus representation on the square. (a) The system's (1.20) trajectory with no phase or frequency-locking; (b) An example of the 3:2 frequency-locked solution trajectory. A closed curve is produced on the torus; (c) An example trajectory of the phase-locked solution of the type 3:2.

lessly wind on the torus never intersecting itself. Since the trajectories on the curved surface of a torus is hard to draw, usually an equivalent representation: a square with periodic boundary conditions, is used, see Fig. 1.6.

If the phase space of the coupled oscillators (1.20) has a periodic trajectory, it is said that oscillators are *frequency-locked*. Mathematically this condition can be expressed as

$$p\left\langle \dot{\theta}_1 \right\rangle - q\left\langle \dot{\theta}_2 \right\rangle = 0, \tag{1.21}$$

where $\langle ... \rangle$ denotes averaging over long period of time. If θ_1 makes p rotations, while θ_2 rotates q times and p and q are relative prime integers then it is said that the system (1.20) has a $p:q$ type frequency-locking. The 1:1 frequency-locking is called the *entrainment*.

In a special case of $p:q$ frequency locking phase derivatives satisfy the following relation

$$p\dot{\theta}_1(t) - q\dot{\theta}_2(t) = 0. \tag{1.22}$$

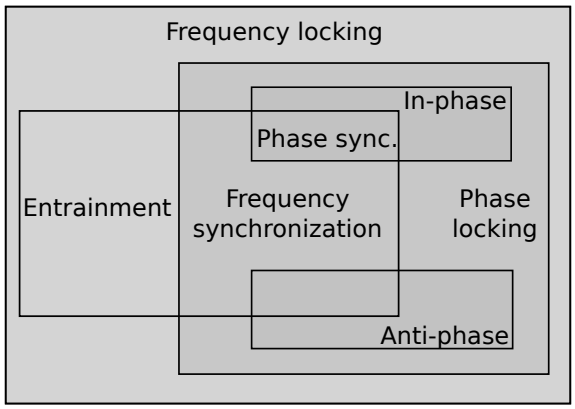

Figure 1.7: Relationship between locking definitions. Adapted from Ref. [17].

This relation implies that phases has a constant difference

$$p\theta_1(t) - q\theta_2(t) = \text{const.} \tag{1.23}$$

The given phenomenon is called the $p : q$ *phase locking*. In the Fig. 1.6 (b) and (c) the examples of 3:2 frequency and phase locking, respectively are shown. The value of constant determines whether the locking is *in-phase* (const = 0), *anti-phase* (const = π, that corresponds to a half of period) or *out-of-phase*. In many cases the difference $p\theta_1(t) - q\theta_2(t)$ approaches constant only in the limit $t \to +\infty$, thus it is said that phase-locking is asymptotic.

If the oscillators (1.20) undergo 1:1 phase-locking, then it means that $\dot{\theta_1} = \dot{\theta_2}$, i.e. both oscillators have the same frequencies. Therefore 1:1 phase-locking is called *frequency synchronization*. Finally, if the phase difference between the oscillators (1.20) is zero, i.e. $\theta_1 = \theta_2$, then it is said that the system is *phase synchronized*. In the literature there exist alternative terminologies for phase synchronization like *full*, *exact* or *perfect synchronization*. The above definitions can be trivially generalized for the higher number of the oscillators. The relations between given definitions is visualized in Fig. 1.7.

It should be noted that the phase synchronization can occur only if all natural frequencies ω_j are identical [18]. From the practical point this is a rare situation. The main object in most applications and theoretical analyses of the synchronization is phase entrainment. It is a phenomenon, when phase difference remain boundend in predefined region

$$|p\theta_1(t) - q\theta_2(t)| < \text{const.} \tag{1.24}$$

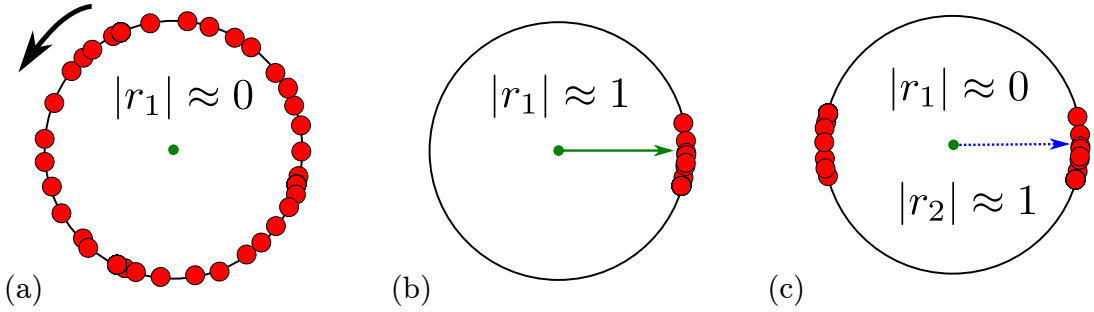

Figure 1.8: Illustration of the phase oscillators: (a) desynchronized; sinchronized in (b) single cluster and (c) double clusters.

This relationship can replace phase locking condition in noisy or chaotic systems.

Moreover, the network of oscillator can exhibit a partial synchronization, where only the part of oscillators are synchronized, while the other part oscillates randomly. In order to estimate the portion of the synchronized oscillators, the criterion called *the order parameter* is introduced

$$r = \frac{1}{N}\sum_{j=1}^{N}\exp(i\theta_j). \tag{1.25}$$

When all oscillator's phases are equal, the absolute value of the order parameter is equal to one $|r| = 1$ (see Fig. 1.8b). For sufficiently large N, $|r| \approx 0$ implies desynchronized state (see Fig. 1.8a). It should be noted, that the given order parameter estimates, just synchronization with coinciding phases. For example, if we would have two synchronized oscillators with phase lag equal to π, then $|r| = 0$. In some networks several synchronized clusters with phase lags between them not equal to 0 may form. To estimate synchronization for these cases the *generalized order parameters* [19] can be introduced

$$r_q = \frac{1}{N}\sum_{j=1}^{N}\exp(iq\theta_j). \tag{1.26}$$

For example, in the system with two synchronized clusters, the order parameter $|r_2|$ will have higher values, while $|r_1|$ will show asymmetry between the clusters (see Fig. 1.8c and Ref. [20] for more details).

Remark: The definitions presented in this subsection are mainly adapted from Refs. [17] and [18]. However, readers should be aware that such basic terms as synchronization, locking and entrainment have no conventional definitions in the literature, thus various authors may use these words with different meanings.

Note that here we did not intend to propose general definitions. Our aim was simply to overview different possible effects in interacting oscillatory systems.

Further we will see that it is not always easy to define the phase of oscillator, thus sometimes other criteria to define the level of the synchronization in the network are used. Such cases will be discussed in the subsequent chapters.

1.3 The problem: pathological synchronization of neural networks

The synchronization of oscillations is a mechanism for neural communication, which endows individual brain areas with the ability to perform specific tasks [21]. On the other hand, pathological, excessive synchronization may be the origin of symptoms of some neurological diseases. Various studies from microelectrodes recordings [22–24] or magnetic brain activity (magnetoencephalography) [25] observation suggest that tremor for Parkinon's disease patients may be caused by synchronous action of the thalamus and basal ganglia neurons (modest volume structures in the center of the brain). Increased synchronization was also measured in monkey model of parkinsonism, while in healthy monkeys synchronization was not observed [26].

1.3.1 The treatment

Pathological synchronization appears as a consequence of degeneration of neurons that produce neurotransmitter called dopamine [27]. Therefore as the first stage in suppression of involuntary limb movement is a pharmacological therapy, when a patient uses medicaments with L-DOPA (levodopa). In the early stages of disease this chemical precursor in the brain increases dopamine quantity [27]. Unfortunately after the long use of this drug its efficacy to suppress tremor decreases [28]. Furthermore adverse effects such as motor fluctuations and dyskinesia[2] are often associated with chronic drug administration also as frequent neuropsychiatric disturbances [29].

As an alternative to drug treatment would be lesioning of particular brain areas. The evidence that brain lesion is a successful method for the suppression of tremor was indicated as early as 1942, but used rarely until the late 1980's [29]. The procedure compared to medical treatment is more successful at improving

[2] A difficulty or distortion in performing voluntary movements.

patients life quality [30]. Nevertheless the intervention into the brain is always related to high risks as the effect of lesioning is irreversible.

In 1987 during stereotactic thalamotomy[3] surgery it was observed that low-frequency stimulation increases tremor, while at higher frequencies tremor was blocked [31]. To achieve a suppression of the tremor, the stimulation amplitude has to exceed a critical value. In [32] it was shown, that the relation between the critical amplitude and stimulation frequency forms a valley between 100Hz and 1kHz. Signals, which frequencies are not included in this region, require higher stimulation amplitudes or fail to suppress. The use of high frequency (HF) deep brain stimulation (DBS) for the treatment of Parkinson's disease was approved by the US Food and Drug Administration. Nowadays it is a standard procedure applied for medically refractory PD patients.

Despite the fact that DBS is used not only for PD treatment, but also shows promising results for suppressing symptoms of diseases like dystonia, major depression, chronic and phantom pain [9], it is not a panacea and has its own shortcomings. In some patients DBS may cause side effects, may not work or the therapeutic effects may become weaker during the time [9, 29].

Currently used DBS involves stimulation with adjustable amplitude and frequency[4] pulse trains. The stimulation is always turned on independently on state of patient. This is the main problem of control, because permanently operating stimulator shortens a battery life time and also may destroy surrounding tissue. Moreover, the adjustment of the control parameters may proceed a day or more longer trials, while optimal amplitude and frequency are chosen empirically by neurologist from patients response to therapy [27, 34].

1.3.2 Approaches for the control improvement

Understanding Parkinsonian network. In order to improve DBS efficacy one should understand the dynamics of basal ganglia and thalamus neurons networks. An early theoretical attempts to understand neural networks of the Parkinson's disease were done by firing rate models. Firing rate models describe activity of neurons population by a single 'average firing rate' variable. One can construct the fire rate equations for different kinds of neural populations and investigate interactions between them. Although the firing-rate models provide some useful information, they are inappropriate for understanding dynamical phenomena on such small-time scales as used in DBS [35].

[3] Lesioning brain region called thalamus.

[4] The current is induced by 2.5-5V voltage source, while the frequency usually is $\gtrsim$ 130Hz [33].

Terman *et. al.* in the paper [36] investigated the relationship between the neural network topology and neurons correlated firing. In the Ref. [36] models of subthalamic nucleus (STN) and globus pallidus externa (GPe) neurons were constructed considering experimental data. According to the authors these neurons have membrane properties that predispose them to rhythmic firing [36]. Derived models were used in construction of three network prototypes: i) sparse random; ii) sparse structured; and iii) tightly connected structured. It was shown that all three networks can produce episodic correlated spiking. Tightly connected structured network was able to produce episodic travelling wave solution, however there is no experimental evidence both in human patients and in primate Parkinsonian models that would support the travelling of coherent waves [27]. The authors suggested that the oscillations of the Parkinosn's state may be generated by increased striatal[5] input and decreased interaction between GPe internal connections.

Understanding the mechanism of high-frequency stimulation. The use of HF in DBS is the standard therapy for the reduction of the Parkinsons disease symptoms. Various studying methodologies like neuronal recordings, biochemical studies, computer modelling, imaging were adopted in order to reveal HF DBS mechanisms. However, these studies provide different explanations of possible mechanism, furthermore some of them are in a direct contradiction.

In order to understand the therapeutic mechanisms at least three questions must be answered [37]: i) What is the effect off DBS on individual neurons around the electrode? ii) Which molecular or neural elements mediate the therapeutic effect of DBS? iii) How neural networks are effected by the DBS? The understand of these questions may lead to a simpler selection of stimulation parameters or even into treatment improvement.

In Ref. [38] were performed simultaneous extracellular single-unit recordings with four individually driven micro-electrodes in the STN network of non-human primates during STN-HFS. Stimulation parameters were as follows: amplitude – 100 μA, frequency – 130 Hz, and 60 μs pulse width. Study provides evidence that STN-HFS decreases abnormal oscillatory activity in the STN. Authors shown that stimulation decreased the mean firing rate in majority of STN neurons from 19 to 8 Hz. Activity returned to base line within 100 milliseconds following the end of the stimulus train. The possible explanation of this behaviour is that after each pulse neurons resume usual activity after about 7 ms, while the gap between stimulation pulses for 130 Hz is 7.7 ms. This means that neurons have very short period of time to fire at their natural frequencies. Further experiments performed

[5]Brain part responsible for motivated movement.

on various brain areas with human patients and primates that supports idea of somatic inhibition in the stimulated nucleus can be found in Refs. [39–41]. These findings is compatible with theoretical work of Pyragas *et. al.* in Ref. [42], which suggests, that HF stimulation stabilizes neuron's resting state or low-amplitude subthreshold oscillations of its membrane potential.

Stimulation enforce neurons to fire in a regular pattern [43, 44] thus disabling them to transmit more subtle messages either normal or abnormal. This hypothesis is related to the computational models, which shows that HFS may induce high-frequency neuronal activity with zero variance, speaking in other words makes an information lesion [45]

The *in vivo* and *in vitro* neurochemical studies on rats show that DBS enhance or suppress production of neurotransmitters like GABA or glutamate [46–49]. The research on human subjects suggests that the similar mechanisms revealed in rat studies are responsible for amelioration of PD symptoms [37, 50]. Findings of [51] suggests that DBS activates the release of a neuromodulator[6] called adenosine, which inhibits neurons [42]. Pharmacological or genetic inactivation of adenosine receptors in living mice prevented the therapeutic effect of DBS. Conversely, intrathalamic infusion of adenosine receptor agonists[7] mimicked the beneficial effects of DBS [51].

It is important to understand, how HFS effects various brain regions. While the number of clinical trials comparative studies is small, the modelling approach was done in Ref. [53]. In this work the authors used the extended version of Rubin and Terman [44] model, for estimating possible STN, GPi (globus pallidus pars interna) and GPe stimulations outcomes. Authors findings suggest that (a) STN-DBS, (b) GPe-DBS, and (c) GPi-DBS could have three completely different network effects: (a) a functional restoration, (b) a functional over-activation, and (c) a functional inhibition of the thalamo-cortical relay activity, respectively [53].

The DBS studies should consider and current spread in brain structures adjacent to the site of stimulation. It is not known precisely how far stimulation spreads and how it varies with stimulation parameters like amplitude, pulse width and frequency. The situation, when stimulation current spreads in nearby regions and effects DBS outcome, may be especially true for STN, which is a small nucleus surrounded by several major fibres tracts [52]. Numerous studies supported

[6] Neurotransmitter is a chemical messenger that communicates across a synapse, while neuromodulator is a chemical that is used for communication with more distant target cells [52]. Neuromodulator can be targetted to a gourp of neurons. Usually effect of neuromodulator is long-lasting.

[7] An agonist is a chemical that binds to a receptor and activates the receptor to produce a biological response.

hypothesis, that the optimal stimulation site is located near the borders of STN, where stimulation effects are likely to extend into the nearby regions [52, 54–56].

In summary the possible HFS mechanism can be the following [57]: i) HFS jam neural transmission through stimulated nuclei (information lesion); ii) HFS stabilizes neurons membrane resting state, leaving just low amplitude subthreshold oscillations; iii) Stimulation can blockade voltage gated ion channels or activate inhibitory terminals; iv) Stimulation decrease production of neurotransmiters, thus inhibiting signal propagation to other neurons; v) Stimulation can inhibit pulse propagation in the axon. The reader who are interested in more detailed lists of possible HF DBS mechanisms, especially those which are related with neurochemistry, may be interested in Refs. [42, 52, 57] and references therein. Finally it must be pointed out that the successful operation of DBS probably is a combination of several mechanisms, thus ones task would be to figure out the size of each mechanisms influence [57].

Stimulation waveform improvement. An interesting concept for the search of alternative stimulation waveforms was proposed in Refs. [58, 59]. The authors suggest to use genetic algorithms. Firstly, they introduce two measures for efficacy of the control signal estimation: *Rel* and *Cor*. *Rel* – reliability, measures the ratio at which the cell correctly responds to sensimotor inputs. If *Rel* equal to 1, then it means that all sensimotor inputs have induced spikes in the cell and that no spikes were excited while there were no sesnimotor inputs [44, 58]. Measure *Corr* quantifies firing patterns through GPi cells' auto- and cross- correlation (see Ref. [58] for more detailed explanation). In the simplest case the cost function required by the genetic algorithm can be chosen from *Cor* or *Rel*, but in real life applications the energy consumption has to be taken into account. Therefore a cost function that estimates the efficacy of stimulation can be written as the sum of weighted measures

$$J = x + wR, \tag{1.27}$$

where x can be *Rel* or *Cor*, R is consumed energy and w is a weighting parameter.

The two strategies can be used for the signals form optimization. The first strategy would be to use periodic signal, while genetic algorithm would select optimal pulse duration, current amplitude and pulse period. The second way would be to use stochastic signals. In this case genetic algorithm would produce stimulation pulse probability distribution function, therefore neurons would be stimulated by the randomly distributed pulse train.

The work of Feng *et. al.* [58] had shown that: i) The HF is not the only one

periodic signal which can switch a network to the normal state; ii) Stochastic DBS waveforms can be effective alternatives for periodic inputs; iii) Genetic algorithm can find different stimulation signals with similarly "good" cost functions. Despite the fact that *Rel* and *Cor* experimentally are hardly measured, this work shows proper direction for further research as the application of genetic algorithm may simplify the estimation of optimal DBS parameters. Furthermore, the existence of multiple signals with similar cost functions can increase the number of patients responsive for DBS treatment.

A different approach for the optimization of the stimulation signal is developed in Ref. [60]. Here the authors rely on a detailed knowledge of the systems model and optimize a stimulus, which lead the oscillators towards a small ball around an unstable fixed point, in a smallest possible time. In the volume of a given ball the concentration of the isochrons[8] is very dense. This means that oscillators, which are driven by stimulus at nearby positions in the ball around the fixed point, may have huge difference in phases. Thus after transient processes oscillations will be detuned. The successful results of a given phase randomization algorithm was demonstrated on the network of reduced globally coupled Hodgkin–Huxley neurons. Nevertheless, the use of the signal optimization requires the perfect knowledge of the system's model, therefore making this approach difficult to apply for experimental setup. Moreover, the control severely distorts the system from oscillatory mode.

Phase resetting and coordinated phase reset stimulations. Another strategy was chosen in Refs. [61–66]. These works share two particular features. The first feature is that, the stimulations consist of two stages. At the first stage, the control signal drives (resets) oscillator's phases to preferable state, thereby ensuring that control would not be dependent on initial conditions. At the second stage, the system is driven to the desynchronized state by a single pulse. Other common feature is that stimulation does not suppress oscillatory behaviour. The difference between methods lies in the first stage where the phase reset can be achieved by single pulse [61–63], a HF pulse train [64] or by low-frequency pulse train (soft phase resetting) [65, 66].

These works were evolved further in Refs. [67, 68], where a *coordinated phase reset* (CR) was introduced. The population of synchronized neurons is stimulated with several electrodes placed at different sites. The stimuli at different electrodes are phase shifted with respect to each other, so they entrain different synchronous clusters of neurons (see Fig. 1.9). When the stimulation is switched off, the

[8] see Sec. 1.2

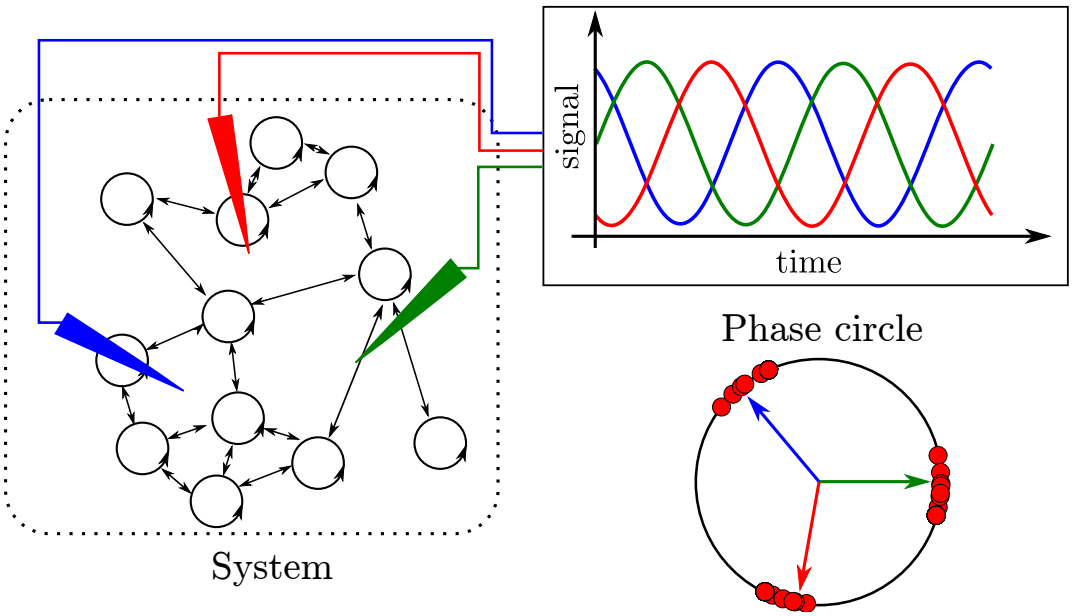

Figure 1.9: An example of the CR setup with three electrodes, which acts with harmonic signals. Due to stimulation oscillators adjust their phases to external force phase and three synchronized clusters emerge.

clusters desynchronize. After some time the population synchronizes to the one-cluster state, and the stimulation is switched on again (demand-control). This method is easy to implement since it does not require any online measurements. By numerical computations [9, 69] and *in vivo* experiments on parkinsonian monkeys [70] it was shown that CR stimulation induces long-term plasticity changes, what means that stimulation can change pathological networks connectivity to normal state. However, the method requires repetitive stimulus administration and cannot constantly maintain the desired unsynchronized state.

Control with feedback. The feedback methods are superior compared to previously discussed because they can stabilize the desired unsynchronized state and maintain it steadily with minimal stimulation intensities. Different algorithms based on linear [71–77] and nonlinear [78–80] time-delayed feedback, linear feedback bandpass filters [81–83] and others [84–87] have been proposed. Some of them will be discussed below.

One of the first feedback method adapted for synchronization control was proposed in Refs. [71–73]. The authors considered a linear single-site delayed feedback, that can be implemented with the single electrode, which performs the mean field measurements and stimulation at the same time. Authors had shown, on simplified and sophisticated oscillators, that by the tuning of feedback strength and delay time it is possible to enhance or suppress collective oscillations. The control signal is large only for short transient process, while at suppressed

synchronization stage the control signal is of the order of the background noise [71], this would help to extend the lifetime of pacemakers battery.

The ideas from linear delay feedback and coordinated reset stimulation [67,68] were combined in Ref. [74–76]. Here delayed feedback signals are administered in a spatially coordinated way via several stimulation sites using particularly selected delays for each stimulation site, respectively. The method was numerically tested on phase oscillators and physiologically realistic models. It was shown that the given setup is robust against variations of the system parameters.

From the physical point of view, the population of neural oscillators can be considered as an active medium. The main idea of the approach presented in Ref. [81] is to couple the medium to an additional passive oscillator i.e., the authors suggested to use the control signal generated from linear damped oscillator driven by the measured signal. Another idea used in Ref. [81] is based on a quite general consideration, that the mean field amplitude, at critical point, experience Hopf bifurcation. It means that instead of studying a huge number of oscillator's equations it is possible to analyze only one – a normal form of the complex mean field amplitude equation. Therefore efficacy of the proposed method was shown on the amplitude equation, where the stability domains of control parameters were estimated. The latter method was adapted for mean field all-to-all coupled Bonhoeffer-van der Pol oscillators and synaptically all-to-all coupled Hindmarsh-Rose neurons.

In order to avoid an overlap of stimulation and measurement processes a feedback algorithm with a spatially separated stimulation and registration setup has been suggested in Ref. [87]. Here the existence of two interacting subpopulations of oscillators were assumed. The measured mean field signal from the first subpopulation was fed through proportional-integro-differential controller to the second subpopulation. In the thermodynamic limit the authors estimated the gain threshold above which the method successfully desynchronizes the both subpopulations. Theoretical predictions were numerically tested and approved on globally coupled van der Pol oscillators.

2. Effect of high-frequency stimulation on pulse propagation in axon

In this chapter, we analyze the effect of a homogeneous HF stimulation on pulse propagation in a single axon. We consider two cases – unmyelinated and myelinated axons. As a basis for an axon model we chose the FitzHugh-Nagumo (FHN) equations [6, 7] and show that for sufficiently large amplitudes of HF stimulation the pulses cannot propagate in the axon. Seeking an analytical results we first apply an averaging method [88] and separate the neuron dynamics into slow and fast components. As a result we derive averaged equations for the slow component that do not contain a high-frequency term. Then we analyze the travelling waves in the averaged system via an asymptotic pulse construction [89, 90] method. Such an approach allow us to obtain the dependence of the parameters of the travelling pulse on the amplitude of HF stimulation current in an analytical form. Also the validity of the results is tested by the numerical simulations.

This chapter is organized as follows. In Sec. 2.1 the general statements about averaging method is presented. Further, this method is adopted for unmyelinated axon in Sec. 2.2 and for myelinated axon in Sec. 2.3. Section 2.2 is constituted from Sec. 2.2.1, where averaged equations for the continuous case are derived, Sec. 2.2.2, which is devoted to analytical and numerical analysis of travelling pulse solutions of the averaged system and in Sec. 2.2.3, we justify the results of travelling pulse solutions by numerical experiments performed with the original FHN model and averaged equations.

For discrete case an asymptotic method for constructing pulse solutions of the averaged equations is described in Sec. 2.3.1. Section 2.3.2 is devoted to the analysis of pulse characteristics in the dependence of the stimulation parameter. In Sec. 2.3.3, we confirm our theoretical findings by direct numerical simulations of the original system and consider an influence of noise.

The chapter is finished with the summary presented in Sec. 2.4.

2.1 Method of averaging

Lets consider an ordinary differential equation

$$\dot{\boldsymbol{x}}(t) = \varepsilon \boldsymbol{f}(\boldsymbol{x}(t), t, \varepsilon), \tag{2.1}$$

where $\boldsymbol{x}(t)$ is a n dimensional vector, $\varepsilon > 0$ is a small parameter, and the vector function $\boldsymbol{f}(\boldsymbol{x}, t, \varepsilon)$ periodically depends on time t, i.e. $\boldsymbol{f}(\boldsymbol{x}, t+T, \varepsilon) = \boldsymbol{f}(\boldsymbol{x}, t, \varepsilon)$. The system of differential equations, which explicitly depends on time t is called a *non-autonomous*. Usually this type of equations is difficult to analyze. Let's say that we want to find the solution $\boldsymbol{x}(t)$ of Eqs. (2.1) with the initial condition $\boldsymbol{x}(0) = \boldsymbol{x}_0$. One would be interested in a simplification of the problem by finding an autonomous system, whose solution would approximate the solution of the original system.

From the first sight it seems that due to the small parameter ε, the approximation of Eqs. (2.1) solutions can be constructed by regular perturbation methods. Such an approximation would be valid just in the time interval $t \in [0, L]$, with L of the order of 1. If we are interested in the time scales as long as $t \sim 1/\varepsilon$, it is necessary to use the singular perturbation methods. One of such methods is based on the averaging theorem [88].

The averaging theorem states that solution of

$$\dot{\boldsymbol{z}}(t) = \varepsilon \bar{\boldsymbol{f}}(\boldsymbol{z}(t)), \tag{2.2}$$

with the averaged function

$$\bar{\boldsymbol{f}}(\boldsymbol{x}) = \frac{1}{T} \int_0^T \boldsymbol{f}(\boldsymbol{x}, s, 0) \mathrm{d}s, \tag{2.3}$$

and with the initial condition $\boldsymbol{z}(0) = \boldsymbol{x}_0$ would differ from solution of Eqs. (2.1) $\boldsymbol{x}(t)$ by the order of magnitude of ε for $t \sim 1/\varepsilon$. More precisely, if ε is small enough, then there exists an ε-independent constant C such that

$$\|\boldsymbol{x}(t) - \boldsymbol{z}(t)\| \leq C\varepsilon, \tag{2.4}$$

for $0 \leq \varepsilon t \leq L$.

Here we present a trivial example, while more sophisticated cases will be dis-

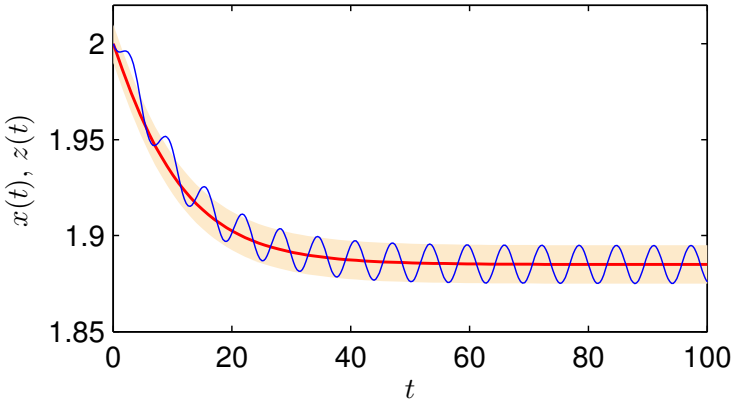

Figure 2.1: The comparison of numerical solutions of Eq. (2.5) and Eq. (2.6) with initial condition $x(0) = 2$ and parameter $\varepsilon = 0.01$. Blue (thin) curve represent solution of the original system $x(t)$, red (bold) curve represent solution of the averaged system $z(t)$, colored area is between curves $z(t) \pm \varepsilon$

cussed in the next sections.

Example. Let's consider a system

$$\dot{x} = \varepsilon \left(\sin(-10x) + \sin(t)\right), \tag{2.5}$$

when ε is small. The averaged function is $\bar{f} = 1/(2\pi) \int_0^{2\pi} [\sin(-10x) + \sin(t)]\, \mathrm{d}t = \sin(-10x)$. Thus the averaged equation reads

$$\dot{z} = \sin(-10z). \tag{2.6}$$

The comparison of numerical solutions of Eq. (2.5) and Eq. (2.6) with the initial condition $x(0) = 2$ and the parameter $\varepsilon = 0.01$ is shown in Fig. 2.1. □

2.2 Unmyelinated axon

Let us consider the FitzHugh-Nagumo (FHN) unmyelinated axons model [6,7] in the presence of homogeneously applied HFS current:

$$\frac{\partial v}{\partial t} = f(v) - w + D\frac{\partial^2 v}{\partial x^2} + a\cos(\omega t), \tag{2.7a}$$

$$\frac{\partial w}{\partial t} = \varepsilon(v + \beta - \gamma w). \tag{2.7b}$$

Here equation (2.7a) describes the dynamics of the membrane potential v, where $f(v) = v - v^3/3$ is the cubic source term of an ionic current, D is the diffusion coefficient and parameters a and ω define respectively the amplitude and frequency

of stimulation induced by DBS electrode. Equation (2.7b) defines the dynamics of the slow recovery variable w with a positive rate parameter $\varepsilon \ll 1$. The parameters β and γ are chosen such that without HFS ($a = 0$) the neuron is in an excitable regime. In numerical simulations presented below, we fix $\beta = 0.7$ and $\gamma = 0.8$. The diffusion coefficient D can be eliminated by rescaling the space variable x, and thus in the following we take $D = 1$ without loss of generality.

2.2.1 Derivation of the averaged equations

Our aim is to simplify the non-autonomous system (2.7) for large frequencies[1] $\omega \gg 1$, when the period of HF oscillations is much less than the characteristic time scales of the FHN axon. Using the small parameter $\omega^{-1} \ll 1$, we seek to eliminate the HF term $a\cos(\omega t)$ and obtain an autonomous system, the solutions of which approximate the original system. First, we change the variables of the system (2.7) by using the substitution

$$v = V + A\sin(\omega t), \tag{2.8a}$$
$$w = W, \tag{2.8b}$$

with

$$A = a/\omega \tag{2.9}$$

called stimulation intensity[2] and derive the following equations for the new variables V and W:

$$\frac{\partial V}{\partial t} = f[V + A\sin(\omega t)] - W + \frac{\partial^2 V}{\partial x^2}, \tag{2.10a}$$
$$\frac{\partial W}{\partial t} = \varepsilon[V + A\sin(\omega t) + \beta - \gamma W]. \tag{2.10b}$$

For $A = 0$ and $a = 0$, the systems (2.10) and (2.7) coincide and have identical solutions. Let us denote these solutions as $V^0(t) = v^0(t)$ and $W^0(t) = w^0(t)$, where by zero superscript we mean that the corresponding parameters A or a are zeros. Our aim is to obtain an approximate solution of the system (2.10)

[1] Note that FHN equations is dimensionless. The characteristic time of FHN potential variable is equal to one, therefore the comparison of the dimensionless stimulation frequency ω with 1 is valid. In the realistic neuron models the stimulation period $2\pi/\omega$ should be compared with characteristic time scale T_0 of the neuron in the absence of stimulation. In that case a small dimensionless parameter is $2\pi\omega^{-1}/T_0 \ll 1$.

[2] In the study of the realistic neuron models we would have a dimensional stimulation intensity $A = a/(\omega C)$, where C is membrane capacity and A has a dimension of millivolts. In this case the dimensionless parameter is $a/(\omega C U_0) \propto 1$, where U_0 is a characteristic action potential of neuron.

for $A \neq 0$. If we fix the amplitude a of HFS and increase the frequency ω, the parameter A varies as $O(\omega^{-1})$. In this case, an approximate solution of the system (2.10) can be obtained by the regular perturbation theory and presented in the form: $V(t) = v^0(t) + O(\omega^{-1})$, $W(t) = w^0(t) + O(\omega^{-1})$. Due to the relation (2.8) an approximate solution of the original system (2.7) has the same form: $v(t) = v^0(t) + O(\omega^{-1})$, $w(t) = w^0(t) + O(\omega^{-1})$. We see that for any fixed a and $\omega \to \infty$ the effect of HFS on the system vanishes, since $v(t) \to v^0(t)$ and $w(t) \to w^0(t)$.

In order to get an appreciable effect from the HFS for large ω, the parameter A must not vanish for $\omega \to \infty$. This can be achieved if with the increase of ω, the amplitude a will be increased proportionally as well, $a \propto \omega$. In other words, we have to assume $A = O(1)$ and $a = O(\omega)$. These assumptions lead to a non-trivial perturbation theory. By rescaling the time variable $t = \omega\tau$ (here τ is the "fast" time) the system (2.10) can be transformed to the standard form of equations discussed in the method of averaging [88]:

$$\frac{\partial V}{\partial \tau} = \omega^{-1}\{f[V + A\sin(\tau)] - W + \frac{\partial^2 V}{\partial x^2}\}, \tag{2.11a}$$

$$\frac{\partial W}{\partial \tau} = \omega^{-1}\varepsilon[V + A\sin(\tau) + \beta - \gamma W]. \tag{2.11b}$$

Due to the small parameter $\omega^{-1} \ll 1$ the variables V and W vary slowly while the periodic functions in the right hand side oscillate fast. According to the method of averaging [88] an approximate solution of the system (2.11) can be obtained by averaging the r.h.s. of the system over fast oscillations. Specifically, let us denote the variables of the averaged system as $(\bar{v}, \bar{w})$. They satisfy the equations:

$$\frac{d\bar{v}}{d\tau} = \frac{1}{2\pi\omega}\int_0^{2\pi}\{f[\bar{v} + A\sin(\vartheta)] - \bar{w} + \frac{\partial^2 \bar{v}}{\partial x^2}\}d\vartheta, \tag{2.12a}$$

$$\frac{d\bar{w}_n}{d\tau} = \frac{\varepsilon}{2\pi\omega}\int_0^{2\pi}[\bar{v}_n + A\sin(\vartheta) + \beta - \gamma\bar{w}_n]d\vartheta. \tag{2.12b}$$

The method of averaging states that the averaged system (2.12) approximates the solutions of the system (2.11) with the accuracy $O(\omega^{-1})$, i.e., $V = \bar{v} + O(\omega^{-1})$ and $W = \bar{w} + O(\omega^{-1})$.

After calculating the integrals and coming back to the original time scale (over-dot denotes differentiation with respect to the original time t), the averaged

system (2.12) simplifies to

$$\dot{\bar{v}} = \bar{f}(\bar{v}) - \bar{w} + \frac{\partial^2 \bar{v}}{\partial x^2}, \tag{2.13a}$$

$$\dot{\bar{w}} = \varepsilon(\bar{v} + \beta - \gamma \bar{w}), \tag{2.13b}$$

where $\bar{f}(\bar{v}) = (1 - A^2/2)\bar{v} - \bar{v}^3/3$. Formally, these equations are similar to the original system (2.7) (for $a = 0$ they are identical), but the HFS term $a\cos(\omega t)$ is eliminated in (2.13). The dependence of the averaged system (2.13) on the HFS appears through the modification of the coefficient at the variable $\bar{v}$ in the function $\bar{f}(\bar{v})$. As a result the nullcline[3] of this equation becomes dependent on the stimulation parameter A. In Fig. 2.2 (a) there are shown nullclines (blue/thin lines) for $A = 0$ together with vector field and two trajectories (red/bold lines), which starts at different sides of the $\dot{\bar{v}} = 0$ nullcline and ends at the rest point.

Due to configuration of the vector field, the neuron can generate a spike only when a perturbation of the membrane potential exceeds threshold value Δ. This threshold is called *excitability*. A mathematical expression for Δ calculation will be presented in the following section.

The nullclines for different values of A are shown in Fig. 2.2 (b), while Fig. 2.2 (c) shows the dependence of the excitability parameter Δ on A. We see that the increase of the stimulation parameter A reduces the excitability of the neuron, since for sufficiently large A the parameter Δ increases drastically with the increase of A. Thus we can expect the large stimulation intensities to block the propagation of pulses. In the next section, we derive the precise criterion for such a conduction block phenomenon.

Finally, the solution of the original nonautonomous system (2.7) can be presented as a sum of the solution of the averaged (autonomous) system (2.13) that describes the slow motion and the high-frequency term:

$$v = \bar{v} + A\sin(\omega t) + O(\omega^{-1}), \tag{2.14a}$$

$$w = \bar{w} + O(\omega^{-1}). \tag{2.14b}$$

We stress that the averaged Eqs. (2.13) depend only on the parameter A that is equal to the ratio of the amplitude to the frequency of HFS. Thus this ratio completely defines the effect of HFS on the averaged system's dynamics. For example, the effect of HFS is the same if we fix the amplitude a and double the

[3]The set of the points in phase plane, where one of the variables change rate becomes zero or in other words if we have ODE system $\dot{x}_i(t) = f_i(\boldsymbol{x})$ for $i = 1, .., N$, then the curves defined by $f_i(\boldsymbol{x}) = 0$ are called nullclines. Intersection of all nullclines shows stationary points.

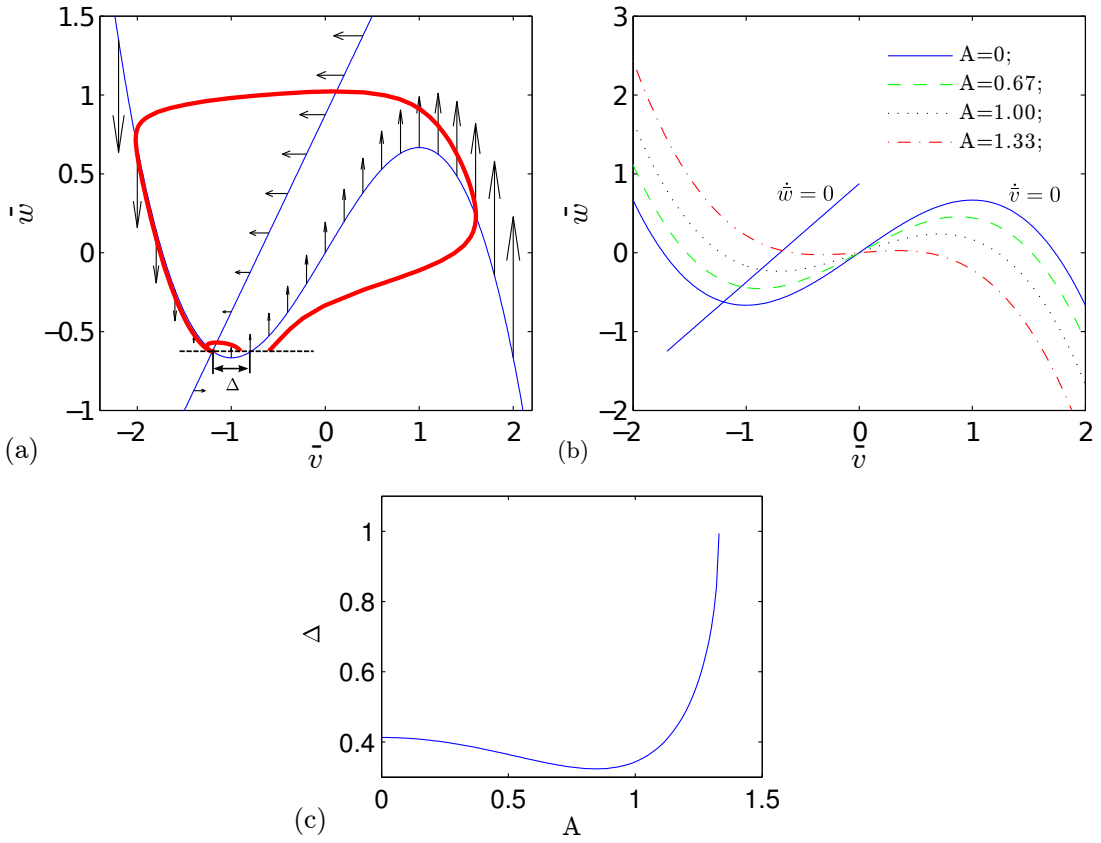

Figure 2.2: The system's (2.13): (a) Nullclines (blue/thin lines) with turned off stimulation $A = 0$ together with vector field and two trajectories (red/bold lines); (b) Nullclines form dependence on different stimulation parameters A; (c) Excitability parameter dependence on stimulation intensity A.

frequency ω or fix the frequency ω and halve the amplitude a. Note that the approximation (2.14) is valid for any fixed A including the small values of this parameter, however, as noted above, the effect of HFS vanishes for $A \to 0$.

2.2.2 Traveling pulse solutions of the averaged system

To study travelling waves, we first place the system of equations (2.13) in a reference of a traveling coordinate frame. We define the traveling wave coordinate $\xi = x - ct$, where $c > 0$ is the wave speed, yet to be determined. Then the partial differential equations (2.13) for the stationary traveling waves become the ordinary differential equations:

$$\bar{v}_\xi = \bar{u}, \tag{2.15a}$$

$$\bar{u}_\xi = -\bar{v}(1 - \frac{A^2}{2}) + \frac{\bar{v}^3}{3} + \bar{w} - c\bar{u}, \tag{2.15b}$$

$$\bar{w}_\xi = -\frac{\varepsilon}{c}(\bar{v} + \beta - \gamma\bar{w}). \tag{2.15c}$$

Here the subscript ξ denotes the derivative with respect to the traveling wave coordinate ξ and an auxiliary variable $\bar{u} \equiv \bar{v}_\xi$ is introduced to write the system as first order differential equations. This system has the only fixed point (V_0, U_0, W_0) with the coordinates $U_0 = 0$, $W_0 = (V_0 + \beta)/\gamma$ and V_0 being the resting potential of the neuron that satisfies the real value solution of the cubic equation

$$\frac{V_0^3}{3} - V_0\left(1 - \frac{1}{\gamma} - \frac{A^2}{2}\right) + \frac{\beta}{\gamma} = 0. \tag{2.16}$$

The traveling pulse solutions are defined by homoclinic orbits of system (2.15). Such orbits begin and end at the fixed point of the system. For further analysis it is convenient to shift the origin of the coordinate system of equations (2.15) to the fixed point. Then the equations for the deviations from the fixed point $(\delta v, \delta u, \delta w) = (\bar{v} - V_0, \bar{u} - U_0, \bar{w} - W_0)$ read:

$$\delta v_\xi = \delta u, \tag{2.17a}$$

$$\delta u_\xi = -F(\delta v) + \delta w - c\delta u, \tag{2.17b}$$

$$\delta w_\xi = -(\delta v - \gamma \delta w)\varepsilon/c. \tag{2.17c}$$

where $F(\delta v) = (1 - A^2/2 - V_0^2)\delta v - V_0\delta v^2 - \delta v^3/3$ is a cubic polynomial function. This polynomial has three real-valued roots one of which is equal to zero. Therefore, the polynomial $F(\delta v)$ can be factorized as

$$F(\delta v) = -\delta v(\delta v - V_1)(\delta v - V_2)/3, \tag{2.18}$$

where the two other roots V_1 and V_2 of the polynomial are positive, satisfy $V_2 \leq V_1$ and can be simply determined from a quadratic equation

$$V_{1,2} = \frac{1}{2}\left(-3V_0 \pm \sqrt{12 - 6A^2 - 3V_0^2}\right). \tag{2.19}$$

Note that the middle root V_2 of the polynomial (2.18) has a clear physical meaning. It defines an excitability threshold Δ of the neuron.

(I) Traveling pulses in a singular limit $\varepsilon \to 0$

To find an approximate analytical expressions for the traveling pulse one can use perturbation methods exploiting the different time scales of the system. In the limit of small parameter $\varepsilon \to 0$, the traveling pulse can be constructed with the help of the geometrical singular perturbation theory [89,90]. The phase space

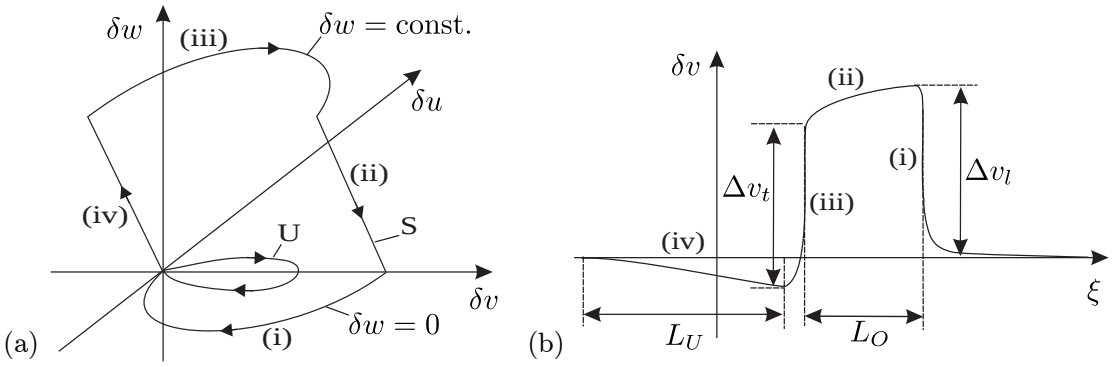

Figure 2.3: (a) Phase space sketch of stable (S) and unstable (U) homoclinic trajectories of system (2.17) in a singular perturbation limit $\varepsilon = 0$. (b) Voltage pulse of the stable (S) homoclinic orbit vs. traveling wave coordinate ξ for small $\varepsilon > 0$. Δv_l and Δv_t denote the heights of the leading and trailing edges while L_O and L_U mark respectively the lengths of pulse segments corresponding to the overshoot and undershoot

sketch of homoclinic orbits for system (2.17) in the singular limit $\varepsilon = 0$ is presented in Fig. 2.3 (a). There are two homoclinic orbits marked by letters U and S. The first orbit lies completely in the plane $\delta w = 0$ and describes a pulse with the zero velocity, which is unstable [91], and hence is not interesting from a physical point of view. The second orbit marked by letter S represents a traveling pulse, which is of interest for further analysis, since it is stable [92]. In Fig. 2.3 (b), a voltage pulse sketch of this orbit is shown in the traveling coordinate frame for small $\varepsilon > 0$. Going backward in ξ or forward in time this pulse consists of four segments [89, 90]: (i) The leading edge that corresponds to a fast dynamics in the plane $\delta w = 0$ of the phase space of system (2.17) [cf. Fig. 2.3 (a)]; (ii) A slow relaxation from $\delta w = 0$ to a new value $\delta w = \tilde{W} = \text{const}$ at the conditions $\delta u = 0$ and $\delta u_\xi = 0$; (iii) The trailing edge that corresponds to a fast dynamics in the plane $\delta w = \tilde{W}$; (iv) The slow relaxation from $\delta w = \tilde{W}$ back to zero at the conditions $\delta u = 0$ and $\delta u_\xi = 0$. Below we describe the governing equations for each segment of the homoclinic trajectory in more details and derive the main parameters of the traveling pulse.

(i) *The leading edge.* This segment of the homoclinic trajectory lies in the plane $\delta w = 0$ and the dynamics of fast variables δv and δu is governed by equations (2.17a) and (2.17b) that can be presented in the form

$$\delta v_\xi = \delta u, \tag{2.20a}$$

$$\delta u_\xi = -F(\delta v) - c\delta u \tag{2.20b}$$

The leading edge is defined by heteroclinic trajectory of the system (2.20),

which connects its fix points $(0,0)$ and $(V_1,0)$ in the phase plane $(\delta v, \delta u)$. Such a trajectory exists when the speed c satisfies (cf., for example, Ref. [4], p. 273):

$$c = \sqrt{1/6}\,(V_1 - 2V_2). \tag{2.21}$$

Although here we have determined the speed of the leading edge, Eq. (2.21) defines the speed of the whole pulse, since the speed of all segments of the stable traveling pulse must be the same. The dependence of the speed c on the stimulation parameter A can be defined analytically in a parametric form. For this purpose we choose the resting potential V_0 as an independent, variable parameter. Then the dependence of A on V_0 can be obtained from (2.16)

$$A(V_0) = [2(1 - 1/\gamma - V_0^2/3 - \beta/\gamma V_0)]^{1/2}. \tag{2.22}$$

The speed c in Eq. (2.21) is expressed through variables V_1 and V_2 whose dependence on the parameter V_0 is determined by Eq. (2.19). Thus the parametric dependence of the speed on the stimulation parameter $[c = c(V_0),\ A = A(V_0)]$ is defined by Eqs. (2.19), (2.21) and (2.22). This dependence is depicted in Fig. 2.4. We see that the speed of traveling pulse decreases with the increase of stimulation intensity and turns to zero at a critical value $A = A^*$ defined by

$$A^* = \sqrt{2(1 - \beta^2/3)}. \tag{2.23}$$

The zero speed is attained at the resting potential $V_0 = -\beta$. Equation (2.23) defines a threshold stimulation intensity for existence of traveling pulse. For $A > A^*$, the traveling pulse solution does not exist and thus the pulses cannot propagate in the axon if the amplitude a of HFS exceeds the critical value $a^* = \omega A^*$, which is proportional to the frequency of HFS.

The hight Δv_l of the leading edge [cf. Fig. 2.3 (b)] is defined as $\Delta v_l = V_1$. Its parametrical dependence on the stimulation parameter A is determined by equations (2.19) and (2.22) and is shown in Fig. 2.4. The hight Δv_l decreases with the increase of the stimulation parameter A, however, unlike the velocity it does not vanish when the stimulation parameter reaches the critical value A^*.

(ii) *Slow relaxation from $\delta w = 0$ to $\delta w = \tilde{W}$.* Here one can neglect the variation of the fast variables in system (2.17), taking $\delta v_\xi = 0$ and $\delta u_\xi = 0$. It follows that $\delta u = 0$ and δw is related with δv by

$$\delta w = F(\delta v) \equiv -\delta v(\delta v - V_1)(\delta v - V_2)/3. \tag{2.24}$$

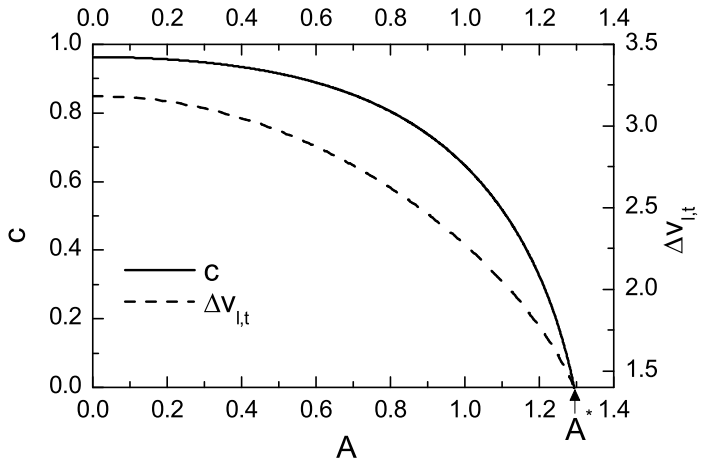

Figure 2.4: Pulse speed c and heights of leading Δv_l and trailing Δv_t edges ($\Delta v_l = \Delta v_t$) as functions of the stimulation parameter A.

The dynamics of the slow variable δw is determined by Eq. (2.17c) with the initial condition $\delta w = 0$ and relationship between the variables δw and δv defined by Eq. (2.24). We are interested in the length L_O of this segment (pulse overshoot) [cf. Fig. 2.3 (b)], which can be defined as

$$L_O = \frac{c}{\varepsilon} \int_{\tilde{W}}^{0} \frac{d\delta w}{\gamma \delta w - \delta v}. \tag{2.25}$$

Note that the value $\tilde{W}$ is jet unknown; it will be determined in the next segment of the homoclinic trajectory.

(iii) *The trailing edge.* This segment of trajectory lies in the plane $\delta w = \tilde{W}$. Here the dynamics of fast variables δv and δu is governed by (2.17a) and (2.17b) that can be presented in the form

$$\delta v_\xi = \delta u, \tag{2.26a}$$

$$\delta u_\xi = \Phi(\delta v, \tilde{W}) - c\delta u, \tag{2.26b}$$

where

$$\Phi(\delta v, \tilde{W}) = \delta v(\delta v - V_1)(\delta v - V_2)/3 + \tilde{W}, \tag{2.27}$$

is a third order polynomial with respect to the variable δv. Denote the roots of this polynomial as $\delta\tilde{v}_1 < \delta\tilde{v}_2 < \delta\tilde{v}_3$ and rewrite equation (2.27) in the form:

$$\Phi(\delta v, \tilde{W}) = (\delta v - \tilde{V}_1)(\delta v - \tilde{V}_2)(\delta v - \tilde{V}_3)/3. \tag{2.28}$$

The trailing edge is defined by heteroclinic trajectory of the system (2.26),

which connects its fix points $(\tilde{V}_3, 0)$ and $(\tilde{V}_1, 0)$ in the phase plane $(\delta v, \delta u)$. Such a trajectory exists when the speed c [which must coincide with the speed of the leading edge defined by (2.21)] satisfies

$$c = \sqrt{1/6}\,(2\tilde{V}_2 - \tilde{V}_3 - \tilde{V}_1). \tag{2.29}$$

Comparing (2.28) with (2.27) and (2.29) with (2.21) we obtain the relationship between the coordinates of fixed points of systems (2.26) and (2.20)

$$\tilde{V}_1 = (2V_2 - V_1)/3, \tag{2.30a}$$
$$\tilde{V}_2 = (2V_1 - V_2)/3, \tag{2.30b}$$
$$\tilde{V}_3 = 2(V_1 + V_2)/3 \tag{2.30c}$$

and define the value of unknown parameter $\tilde{W}$ introduced previously:

$$\tilde{W} = -\tilde{V}_1\tilde{V}_2\tilde{V}_3/3. \tag{2.31}$$

The hight Δv_t of the trailing edge [cf. Fig. 2.3 (b)] is defined as $\Delta v_t = \tilde{V}_3 - \tilde{V}_1$. From equations (2.30a) and (2.30c) it is easy to see that it coincides with the hight of the leading edge, $\Delta v_t = V_1 = \Delta v_l$.

Taking into account the above results, equation (2.25) defining the length of the pulse overshoot can be rewritten in a form convenient for numerical estimation,

$$L_O = \frac{c}{\varepsilon}\int_{\tilde{V}_3}^{V_1} \frac{F'(\delta v)d\delta v}{\gamma F(\delta v) - \delta v}, \tag{2.32}$$

where $F'(\delta v)$ is the derivative of function $F(\delta v)$. Here we have replaced the integration variable δw by δv taking into account the relationship (2.24).

(iv) *Slow relaxation from $\delta w = \tilde{W}$ back to $\delta w = 0$.* Here as well as in the segment (ii) the variation of the fast variables is neglected and dynamics of the slow variable δw is determined by (2.17c) with the initial condition $\delta w = \tilde{W}$. Taking into account the relationship (2.24) between the variables δw and δv the length L_U of this segment (pulse undershoot) [cf. Fig. 2.3 (b)] is defined by integral:

$$L_U = \frac{c}{\varepsilon}\int_{0}^{\tilde{V}_1} \frac{F'(\delta v)d\delta v}{\gamma F(\delta v) - \delta v}. \tag{2.33}$$

The lengths L_O and L_U are shown in Fig. 2.5 as functions of the stimulation parameter A. Both lengths decrease with the increase of A and vanish when the stimulation parameter reaches the threshold value A^*. Thus the mechanism of

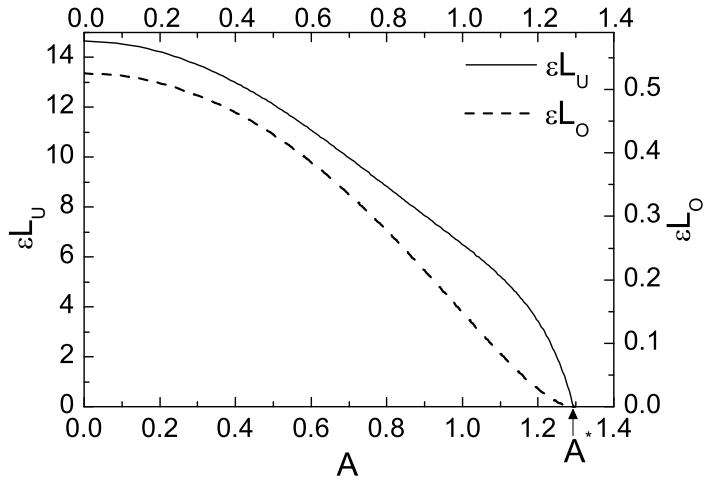

Figure 2.5: The lengths of pulse overshoot (L_O) and undershoot (L_U) multiplied by parameter ε vs. the stimulation parameter A.

HFS responsible for the suppression of pulse propagation consists in pulse narrowing. With the increase of HFS intensity the pulse shrinks and its width becomes zero when $A = A^*$.

(II) Traveling pulses for finite $\varepsilon > 0$

The singular perturbation theory has allowed us to determine analytically many important characteristics of the traveling pulse, including the threshold value A^* of the stimulation parameter for the existence of traveling pulse solution. In fact, the threshold A^* depends on the parameter ε. For finite $\varepsilon > 0$, the analytical approach fails and the homoclinic trajectories of system (2.17) can be determined only numerically. In Fig. 2.6 we show the results of such an analysis. The dependence of the pulse speed on the stimulation parameter A for different values of ε is presented in Fig. 2.6 (a). For $\varepsilon \geq 0.008$, these curves have been constructed with the help of the MatCont package [93] and for smaller $\varepsilon \leq 0.0008$, the shooting method [94] has been used. Each curve consists of two branches. The upper branch represents the speed of the stable pulse [91], while the lower branch corresponds to the unstable pulse [92]. The point where the two branches coincide defines the threshold parameter A^*. At this point, the homoclinic trajectories corresponding to the fast (stable) and slow (unstable) pulses collide and disappear, such that for $A > A^*$ the traveling pulse solutions do not exist. Note, that the curves in Fig. 2.6 (a) approach asymptotically the singular perturbation solution (bold curve) when $\varepsilon \to 0$. This justifies the analytical results obtained in the previous section.

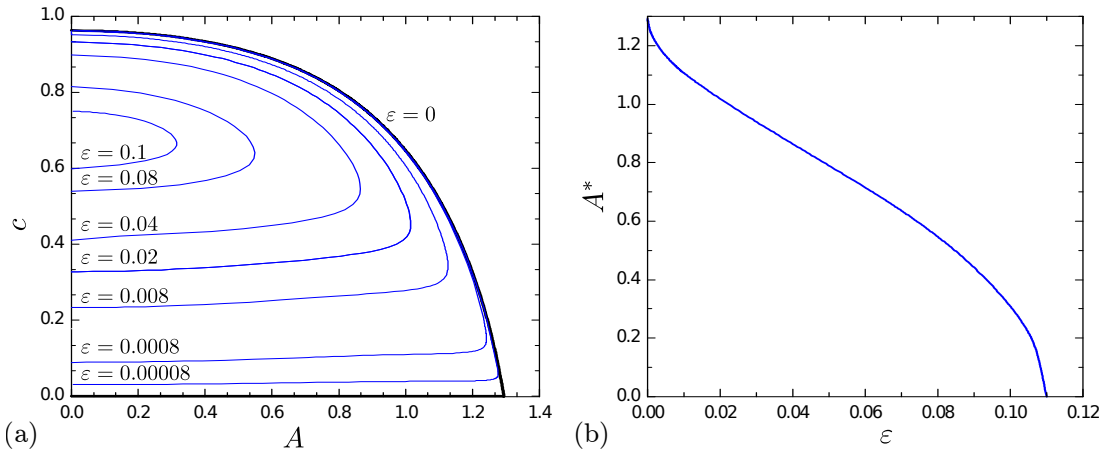

Figure 2.6: (a) The speed c of traveling pulses as a function of the stimulation parameter A for different values of ε. The bold curves show the speed dependence analytically determined in the singular perturbation limit $\varepsilon = 0$. (b) The threshold A^* of the stimulation parameter vs. ε.

The dependence of the threshold A^* of the stimulation parameter on ε is shown in Fig. 2.6 (b). Larger values of the parameter ε require less stimulation intensity A^* to suppress the pulse. This is because the pulse length of the free ($A = 0$) system depends on the parameter ε. The increase of the parameter ε have the same effect as the increase of the stimulation intensity A; they both narrow the pulse [cf. (2.32) and (2.33)]. Therefore, for larger ε less HFS intensity is needed to zero the pulse length and suppress its propagation.

2.2.3 Numerical experiments

To justify the results of stationary traveling pulse solutions obtained in the previous section, here we perform numerical experiments with the original system (2.7) of partial differential equations (PDE) as well as with the averaged PDEs (2.13). First we verify the validity of the averaged equations. In Fig. 2.7, we show the dynamics of the neuron potential in the middle of the sample at different values of the stimulation parameter A. The thin (blue) curves represent the solutions of the original system (2.7) while the bold (red) curves show the solutions of the averaged Eqs. (2.13). We see that these solutions are in good agreement. The PDEs have been solved with the periodic boundary conditions taking the length of the sample equal to $L = 400$ and $\Delta x = 0.5$ discretization step. The initial conditions are chosen in such a way, that for a given stimulation intensity A, they coincide with the stable pulse profile. As predicted by singular perturbation theory and numerical analysis of stationary pulses for finite ε, the increase of the stimulation intensity leads to the decrease of both the pulse velocity

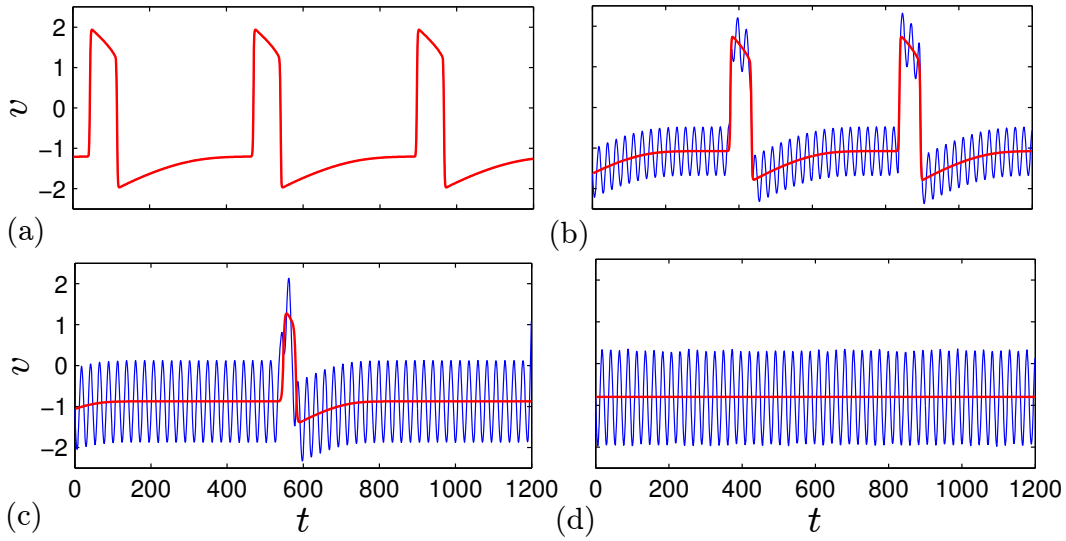

Figure 2.7: The dynamics of the neuron potential at the middle of the sample for fixed $\varepsilon = 0.008$ and $\omega = 50$, and different values of the HFS amplitudes: (a) $a = 0$ ($A = 0$); (b) $a = 30$ ($A = 0.6$); (c) $a = 50$ ($A = 1$); (d) $a = 56.5$ ($A = 1.13$). The thin (blue) curves show the solutions of the original system (2.7) and the bold (red) curves represent the solutions of the averaged system (2.13).

and the pulse length [cf. Figs. 2.7 (a)-(c)]. The propagating pulse disappears for $A > A^* \approx 1.13$ and only small amplitude subthreshold high-frequency oscillations remain [cf. Fig. 2.7 (d)].

In Fig. 2.8, we demonstrate the space-time evolution of the averaged system (2.13) under initial excitation of the middle of the neuron. The excitation is performed with a DC current $I = 2$ applied to the small space interval $\Delta x = 4$ in the center of the sample for the initial time interval $\Delta t = 1$; then the DC current is off. In the absence of HFS, the DC stimulus initiates two pulses traveling in opposite directions [cf. Fig. 2.8 (a)]. An influence of HFS to the pulse propagation is demonstrated in Figs. 2.8 (b)-(d). When the HFS intensity is increased, the propagating pulses shrink and slow down. The pulses die out when the stimulation parameter exceeds the threshold value $A^* \approx 1.13$ [cf. Fig. 2.8 (d)]. Again, this confirms the main conclusions of the previous section.

2.3 Myelinated axon

In this section we consider a one-dimensional chain of coupled excitable elements governed by the FHN equations in the presence of high-frequency field:

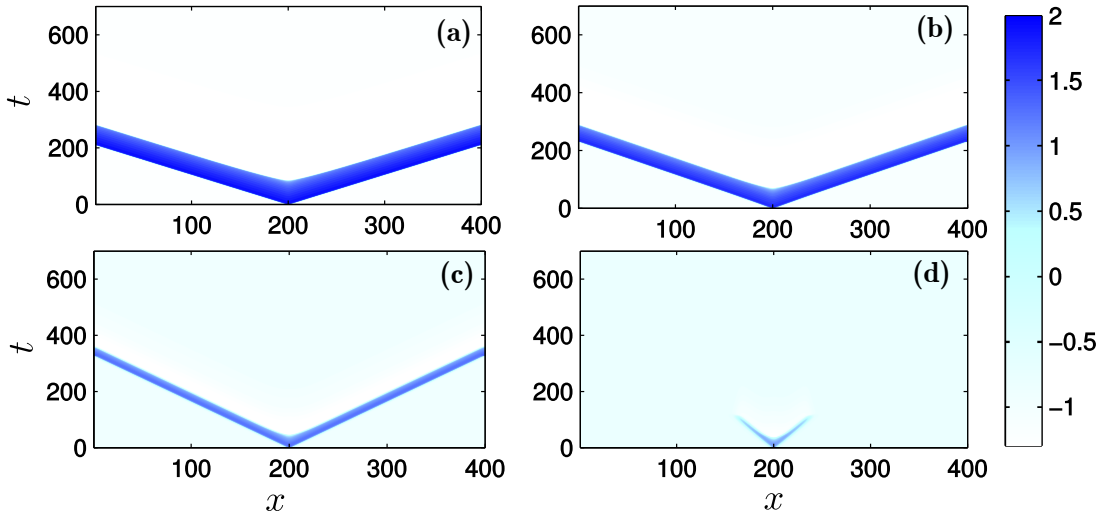

Figure 2.8: Space-time evolution of the averaged system (2.13) under initial excitation of the center of the neuron with the DC current $I = 2$ applied for a short time interval $\Delta t = 1$. The parameter ε is the same as in Fig. 2.7 and the HFS amplitudes are: (a) $A = 0$; (b) $A = 0.6$; (c) $A = 1.0$; (d) $A = 1.13$.

$$\dot{v}_n = f(v_n) - w_n + D(v_{n+1} - 2v_n + v_{n-1}) + a\cos(\omega t), \tag{2.34a}$$

$$\dot{w}_n = \varepsilon(v_n + \beta - \gamma w_n). \tag{2.34b}$$

These equations are discrete case of the (2.7) equations and represents a myelinated axon. As we further will see, discreteness brings new features to the system and its stimulation effects. All variables has the same meaning as in (2.7) case: v_n denotes the membrane potential and w_n is the recovery variable of the nth node, $f(v_n) = v_n - v_n^3/3$ is the cubic source term of an ionic current, and the discrete diffusive term with the coupling strength D is proportional to the difference in internodal currents through a given site. The last term in Eq. (2.34a) describes the current induced by HFS, where a and ω are the amplitude and the frequency, respectively. The constant $\varepsilon > 0$ is the ratio between the characteristic time scales of v_n and w_n variables. As usual, we assume $\varepsilon \ll 1$, that is, fast excitation and slow recovery. In this section, numerical simulations are performed for $\gamma = 0.8$ and $\beta = 0.7$, what determines excitable state of the neuron.

Similar to the continuous case, the solution of (2.34) can be approximated as

a sum of averaged equations solution and high frequency term

$$v_n(t) \approx \bar{v}_n(t) + A\sin(\omega t), \tag{2.35a}$$
$$w_n(t) \approx \bar{w}_n(t). \tag{2.35b}$$

Where averaged equations are

$$\dot{\bar{v}}_n = \bar{f}(\bar{v}_n) - \bar{w}_n + D(\bar{v}_{n+1} - 2\bar{v}_n + \bar{v}_{n-1}), \tag{2.36a}$$
$$\dot{\bar{w}}_n = \varepsilon(\bar{v}_n + \beta - \gamma\bar{w}_n). \tag{2.36b}$$

Again, the averaging modified ionic current function $f(v_n)$ to $\bar{f}(\bar{v}_n) = (1 - A^2/2)\bar{v}_n - \bar{v}_n^3/3$, where the parameter A is equal to the ratio of the amplitude to the frequency of stimulating current, $A = a/\omega$. The effect of stimulation to nullclines can be seen in Fig. 2.2 (b).

2.3.1 Asymptotic construction of pulse solutions

The method of averaging has allowed us to reduce the original problem to the analysis of averaged Eqs. (2.36). These equations are autonomous, and we can utilize theoretical approaches developed for the free discrete FHN system. In the following, we are interested in estimating characteristic parameters of the propagating pulses in the dependence of the stimulation parameter A and finding a criterion for the propagation failure. Note that if the averaged Eqs. (2.36) have the solution with a propagating pulse then in the original system this pulse will propagate against the background of homogeneous high-frequency oscillations described by the term $A\sin(\omega t)$ in Eq. (2.35a). A comparison of solutions of the original Eqs. (2.34) and averaged system (2.36) is demonstrated in Fig. 2.9 (a).

An asymptotic construction of pulse solutions for the free discrete FHN equation in the limit $\varepsilon \to 0$ is described in Ref. [95]. The main idea is similar to the Keener's asymptotic idea [90] developed for the FHN model with spatially continuous diffusion also used in previous section. We combine these ideas with the Erneux's and Nicolis' [96] perturbation theory developed for the discrete Nagumo model to study pulse propagation in the averaged system (2.36).

A snapshot of a typical propagating pulse computed from the system (2.36) is shown in Fig. 2.9(b). As in continuous case the pulse profile can be subdivided into four segments. There are two segments in which $\bar{v}_n$ vary smoothly with n, separated by two moving sharp fronts. We refer to the segment between the fronts as the pulse overshoot and to the segment following the trailing edge as the pulse

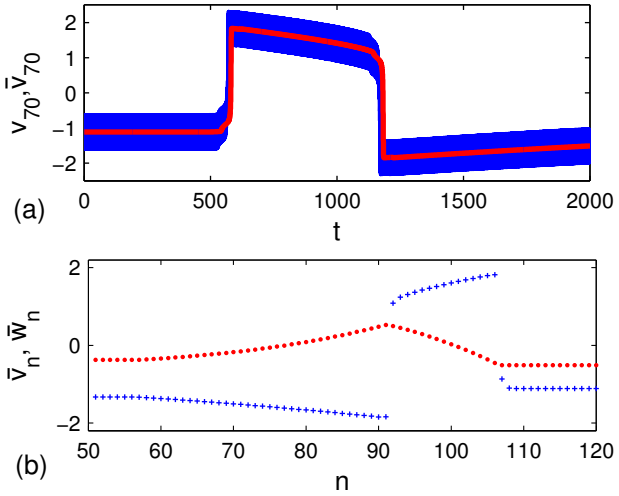

Figure 2.9: (a) Comparison of solutions of the original Eqs. (2.34) and averaged Eqs. (2.36). The dynamics of the membrane potential for the 70th node of axon obtained from the original and averaged systems are shown by blue (dark grey) (the HF oscillations are converged) and red (light grey) curves, respectively. (b) Snapshot of typical pulse propagating from left to right computed from the averaged system (2.36). The membrane potential and recovery variables are marked by the dots (red) and crosses (blue), respectively. The parameters are: $a = 5$, $\omega = 10$, $A = 0.5$, $D = 0.015$ and $\varepsilon = 0.0008$.

undershoot. In the latter two segments, we may set $\dot{v}_n = 0$, $D = 0$ and obtain a description of slow recovery. Wave fronts are smooth solutions $\bar{v}_n(t) = \bar{v}(z)$, $\bar{w}_n(t) = \bar{w}(z)$ of the continuous variable $z = n - ct$, where c is the pulse speed. The recovery variable $\bar{w}$ is constant at each side of the front, and the excitation variable is governed by the discrete Nagumo Eq. (2.36a). A stable pulse is obtained when the velocity of the leading edge is equal to the velocity of the trailing edge.

For further analysis, we rewrite Eqs. (2.36) in a more convenient form. For $D = 0$, these equations have the only fixed point $(\bar{v}_n, \bar{w}_n) = (V_0, W_0)$, where $W_0 = (V_0 + \beta)/\gamma$ and V_0 is the resting potential of the neuron that satisfies the real value solution of the cubic equation (2.16). We define the deviations from the fixed point as $(\delta v_n, \delta w_n)=(\bar{v}_n - V_0, \bar{w}_n - W_0)$ and rewrite Eqs. (2.36) for these deviations

$$\delta\dot{v}_n = F(\delta v_n) - \delta w_n + D(\delta v_{n+1} - 2\delta v_n + \delta v_{n-1}), \tag{2.37a}$$

$$\delta\dot{w}_n = \varepsilon(\delta v_n - \gamma\delta w_n), \tag{2.37b}$$

where $F(\delta v_n)$ is a cubic polynomial function defined by Eq. (2.24).

We can now discuss different segments in the asymptotic description ($\varepsilon \to 0$) of a pulse as follows (cf. [95]).

(i) *The leading edge.* Here the membrane potential δv_n varies rapidly, while the recovery variable is fixed at $\delta w_n = 0$, so that Eqs. (2.37) reduce to

$$\delta\dot{v}_n = F(\delta v_n) + D(\delta v_{n+1} - 2\delta v_n + \delta v_{n-1}). \tag{2.38}$$

This equation admits a solution in the form of a wave front moving towards the right $\delta v_n(t) = \delta v(n - ct)$ with speed c measured in nodes per unit time t. The monotone decreasing profile $\delta v(z)$ satisfies the boundary conditions $\delta v(-\infty) = V_1$ and $\delta v(\infty) = 0$. Below we will use Eq. (2.38) to derive the criterion for propagation failure and to estimate the pulse speed for small and large coupling strength D.

(ii) *The pulse overshoot.* This is a segment between the fronts in which the variation of the fast variable δv_n can be neglected. Taking $D(\delta v_{n+1} - 2\delta v_n + \delta v_{n-1}) = 0$ and $\delta\dot{v}_n = 0$ in Eq. (2.37a) we obtain the relationship between δv_n and δw_n

$$\delta w_n = F(\delta v_n). \tag{2.39}$$

The inverse relationship $\delta v_n = R(\delta w_n)$ can be obtained by solving the cubic equation (2.39) with respect to δv_n. We numerate the roots of this equation in increasing order as $R_1(\delta w_n) < R_2(\delta w_n) < R_3(\delta w_n)$. In this stage membrane potential is in the neighborhood of V_1, what corresponds to the branch $R_3(\delta w_n)$ of Eq. (2.39) solution. Thus the slow recovery variable obeys Eq. (2.37b) with $\delta v_n = R_3(\delta w_n)$:

$$\delta\dot{w}_n = \varepsilon[R_3(\delta w_n) - \gamma\delta w_n]. \tag{2.40}$$

This segment contains a finite number of nodes. On its far right $\delta w_n = 0$. As we move towards the left, δw_n increases slowly until it reaches a certain value $\tilde{W}$ corresponding to that in the trailing wave front. The value $\tilde{W}$ is determined from the condition that the leading and trailing edges move with the same speed. Equations (2.39) and (2.40) will be used below to estimate the length of pulse overshoot.

(iii) *The trailing edge.* Here the recovery variable is fixed at $\delta w_n = \tilde{W}$, while dynamics of the variable δv_n is governed by the equation:

$$\delta\dot{v}_n = \tilde{F}(\delta v_n) + D(\delta v_{n+1} - 2\delta v_n + \delta v_{n-1}), \tag{2.41}$$

where

$$\tilde{F}(\delta v_n) = F(\delta v_n) - \tilde{W} \tag{2.42}$$

is a cubic polynomial with respect to δv_n whose roots we denote by $\tilde{R}_1 < \tilde{R}_2 < \tilde{R}_3$.

We are interested in solution of Eq. (2.41) in the form of a moving trailing front $\delta v_n(t) = \delta v(n - ct)$ with the boundary conditions $\delta v(-\infty) = \tilde{R}_1$ and $\delta v(\infty) = \tilde{R}_3$. Now the speed c of the front depends on the parameter $\tilde{W}$. To obtain the appropriate value of this parameter the dependence $c = c(\tilde{W})$ has to be numerically estimated from Eq. (2.41). Then the correct value $\tilde{W}$ is determined from the requirement $c(\tilde{W}) = c(0)$, which means that the leading and trailing edges move with the same speed. As mentioned above, the value $\tilde{W}$ is needed to estimate the pulse length.

(iv) *The pulse undershoot.* This segment corresponds to the pulse tail. Here the recovery variable obeys Eq. (2.37b) with $\delta v_n = R_1(\delta w_n)$:

$$\delta \dot{w}_n = \varepsilon[R_1(\delta w_n) - \gamma \delta w_n], \tag{2.43}$$

where $R_1(\delta w_n)$ is the least root of Eq. (2.39). Equation (2.43) describes a slow relaxation of δw_n from the initial state $\delta w_n = \delta \tilde{w}$ to the state $\delta w_n = 0$. We will use this equation to estimate the length of pulse undershoot.

2.3.2 Pulse characteristics and propagation failure as functions of the stimulation parameter A

We are seeking to define the main characteristics of the pulse in the dependence of the stimulation parameter A. We are also interested in the criterion of propagation failure. There are two factors responsible for this phenomenon. The first is inherent for discrete systems and may come into play if the coupling strength D is too small and/or the excitability threshold V_2 is too large. For $\varepsilon = 0$, this factor can be analyzed based on the Nagumo Eq. (2.38). There exists a critical value $D = D_c$ below which the leading front fails to propagate [96, 97]. In this section part (I) we will establish the dependence of the critical coupling D_c on the stimulation parameter A.

The second factor responsible for the propagation failure is related to the finite value of ε, when the recovery is not sufficiently slow. This phenomenon also occurs in the spatially continuous FHN system. The continuous system possesses two pulses (one stable and other unstable), which coalesce at a certain critical value of $\varepsilon = \varepsilon_c$ and cease to exist for $\varepsilon > \varepsilon_c$ (e.g. Sec. 2.2.2). In the discrete FHN system, the propagation failure occurs due to the finite number of nodes inside the pulse [95]. With the increase of ε, the length of the pulse decreases, and the pulse ceases to exist when its length becomes less than the distance between the

nodes. We will discuss this type of propagation failure in this section part (III).

(I) Propagation failure for $\varepsilon = 0$

First, we establish a criterion when the leading front (consequently, also the pulse) cannot propagate in the system. For $\varepsilon = 0$, the leading front is governed by the discrete Nagumo Eq. (2.38). This equation has been extensively studied in the literature and various algorithms for finding approximate solutions have been introduced. Here we extend the ideas of the perturbation theory proposed in Ref. [96] and derive a criterion for the propagation failure in the dependence of the stimulation parameter A. To simplify the analysis, we reduce the number of parameters in Eq. (2.38) by the following substitutions: $V_2/V_1 = q$, $3D/V_1^2 = d$, $V_1 t/3 = \tau$ and $\delta v_n/V_1 = u_n$. Then Eq. (2.38) transforms to

$$du_n/d\tau = \psi(u_n) + d(u_{n+1} - 2u_n + u_{n-1}), \tag{2.44}$$

where

$$\psi(u_n) = -u_n(u_n - 1)(u_n - q). \tag{2.45}$$

Equations (2.44) and (2.45) contain only two parameters, q and d. To use the ideas of the perturbation theory [96], we assume that q is a small parameter compared to 1. This assumption is satisfactory if the stimulation parameter A is not very large. In this subsection, we are mainly interested in values of $A \in (0, 1.2)$, then q varies in the interval $(0.12, 0.23)$.

To determine the conditions for a traveling front solution, we consider a set of $N + 2$ elements described by Eqs. (2.44) for $n = 1, \ldots, N$ and the boundary conditions for the first and last nodes as

$$u_0 = 1, \quad u_{N+1} = u_N. \tag{2.46}$$

The front solution joining two stable points $u_n = 1$ and $u_n = 0$ can be originated by the initial condition: $u_n = 0$ for $n = 1, \ldots, N$ at $t = 0$. If there is no coupling between the nodes ($d = 0$), the initial front remains pined for all times $t > 0$. However, if we increase d to some critical value $d = d_c(q)$, the front starts to propagate. The critical value d_c can be estimated by the bifurcation analysis of the steady-state solutions of Eqs. (2.44).

The idea of the bifurcation analysis can be demonstrated with the simple example of a neuron consisting of only three elements. In this case $N = 1$ and we have the only dynamic equation for u_1: $du_1/d\tau = \psi(u_1) + d(1 - u_1)$. For $d = 0$,

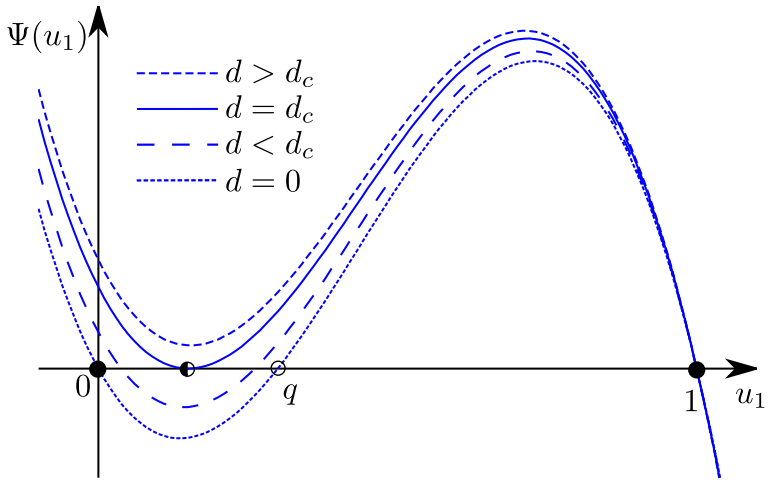

Figure 2.10: Dependence of function $\mathrm{d}u_1/\mathrm{d}t = \Psi_1 \equiv \psi(u_1) + d(1-u_1)$ on various diffusion coefficients for neuron consisting of only three elements, i.e. N=1. Full circles show stable points, empty – unstable, half-empty – saddle-node bifurcation point.

this system has two stable fixed points $u_1 = 0$ and $u_1 = 1$ and one unstable fixed point $u_1 = q$ (see Fig. 2.10). With the increase of d, the points $u_1 = 0$ and $u_1 = q$ approach each other and coalesce at the saddle-node bifurcation for some $d = d_c$, so that for $d > d_c$ the only stable fixed point $u_1 = 1$ remains in the system. The critical value d_c can be determined from the equations: $\Psi_1 \equiv \psi(u_1) + d(1-u_1) = 0$ and $d\Psi_1/du_1 = 0$. Solving these equations we obtain $d_c = q^2/4$. This expression has been derived in Ref. [96]; it is valid for a neuron with an arbitrary number of nodes with accuracy $O(q^2)$. In the following we refine this expression by expanding it with higher-order terms with respect to q.

To derive higher-order terms in the dependence $d_c = d_c(q)$ we have to generalize the above consideration for a neuron consisting of an arbitrary number of nodes. When the number of nodes in a neuron is $N + 2$ the saddle-node bifurcation initiating the front propagation takes place in an N dimensional phase space defined by the state vector $\mathbf{U} = (u_1, u_2, \ldots, u_N)$. The minimal criterion for front propagation would be that the fixed points, having coordinates $(0, 0, \ldots, 0)$ and $(q, 0, \ldots, 0)$ at $d = 0$, coalesce at $d = d_c$, what means that front at least would be able travel from the zeroth to the first node. Coalescence of these points induce saddle-node bifurcation, it would happen when the r.h.s. of Eqs. (2.44) and their Jacobian vanish:

$$\psi(u_n) + d(u_{n+1} - 2u_n + u_{n-1}) = 0, \quad n = 1, \ldots, N, \tag{2.47}$$

$$\begin{vmatrix} \psi'(u_1)-2d & d & 0 & \cdots & 0 & 0 \\ d & \psi'(u_2)-2d & d & \cdots & 0 & 0 \\ \vdots & \vdots & \vdots & \ddots & \vdots & \vdots \\ 0 & 0 & 0 & \cdots & d & \psi'(u_N)-d \end{vmatrix} = 0. \tag{2.48}$$

Equations (2.47) and (2.48) together with the boundary conditions (2.46) define completely the conditions of the saddle-node bifurcation for arbitrary N.

For small q, these equations can be solved by expanding $d = d_c(q)$ and $u_n(q)$ in power series of the parameter q. The analysis of low-dimensional cases $N = 1, 2$ suggests that $d_c = O(q^2)$ and $u_n = O(q^n)$. This motivates the following general expansions:

$$d_c = \sum_{k=0}^{\infty} q^{2+k} d^{(k)}, \quad u_n = \sum_{k=0}^{\infty} q^{n+k} u_n^{(k)}. \tag{2.49}$$

Substituting Eqs. (2.49) into (2.47) and (2.48) and equating terms at different powers of q one obtains the expansion coefficients $d^{(k)}$ and $u_n^{(k)}$ in an explicit form. Performing this procedure up to third-order terms in the expansion of d_c, we get: $d^{(0)} = 1/4$, $d^{(1)} = 1/8$, $d^{(2)} = 7/64$, $u_1^{(0)} = 1/2$, $u_1^{(1)} = 1/8$, $u_1^{(2)} = 5/32$, and $u_2^{(0)} = 1/8$. As a result we obtain the critical value of the coupling strength up to terms proportional to q^4:

$$d_c = \frac{q^2}{4}\left(1 + \frac{1}{2}q + \frac{7}{16}q^2\right) \tag{2.50}$$

or in original variables:

$$D_c = \frac{V_2^2}{12}\left[1 + \frac{1}{2}\frac{V_2}{V_1} + \frac{7}{16}\left(\frac{V_2}{V_1}\right)^2\right]. \tag{2.51}$$

Equation (2.51) together with Eqs. (2.16) and (2.19) gives an analytical dependence of the critical coupling strength D_c on the stimulation parameter A. This dependence is depicted in Fig. 2.11. The dashed curve shows this dependence estimated from the first-order term $V_2^2/12$ in Eq. (2.51), while the solid curve takes into account all three terms in expansion (2.51). The critical values of the coupling strength obtained directly by numerical simulation of the Nagumo Eq. (2.38) are shown by symbols. We see that the analytical formula (2.51) agrees well with the numerical experiments.

An important property of the dependence $D_c = D_c(A)$ is the presence of a dip in a certain interval of A: with the increase of A the D_c first falls to a minimal value $D_c^* = D_c(A^*)$ at $A = A^*$ and then increases for $A > A^*$. Such

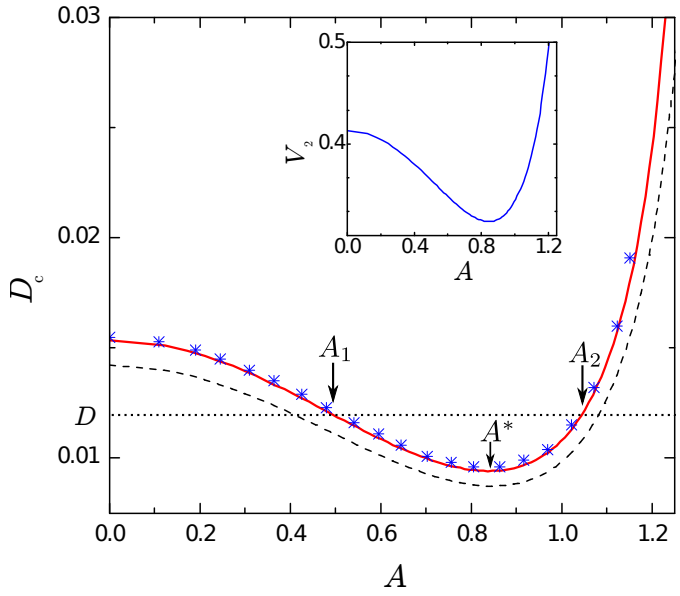

Figure 2.11: Critical coupling strength D_c as a function of the stimulation parameter A. Dashed curve represents an approximation with the only first term in expansion (2.51), the solid curve takes into account all three terms in (2.51), and asterisks show the results of direct numerical simulation of Eq. (2.38). The inset shows the dependence of the excitability threshold V_2 on A.

a dependence allows us to enhance the conductivity of a neuron by applying the HFS of certain amplitudes. Indeed, if we take the value D of the coupling strength from the interval $[D_c^*, D_c(0)]$, then the pulse cannot propagate without HFS, since $D < D_c(0)$. However, if we increase A so that its value ends up in the interval $A_1 < A < A_2$ where $D_c(A_1) = D_c(A_2) = D$, then the propagation becomes possible. For $A > A_2$, the propagation will be suppressed again.

We emphasize that the effect of enhancement of pulse propagation by HFS is an exclusive property of spatially discrete systems. This is because the difference operator that describes the coupling between the nodes can be approximated by the diffusion operator only in the limit $D \to \infty$, whereas this effect takes place only for small D, when $D < D_c(0)$. For $D > D_c(0)$, the HFS may cause only suppression.

The mechanism of enhancement of pulse propagation can be explained as follows. If we omit higher-order terms in expansion (2.51), then we reveal that the critical coupling strength D_c is proportional to the square of the neuron excitability threshold, $D_c \propto V_2^2$. Therefore, the dip in the dependence of D_c on A is caused by a similar dependence of the excitability threshold V_2 on A. The dependence $V_2 = V_2(A)$ is shown in the inset of Fig. 2.11. We see that in a certain interval of the stimulation parameter A, the HFS reduces the excitability threshold of

excitable elements, and this enhances the pulse propagation. Similarly, the suppression of pulse propagation for large A is explained by the sudden increase of the excitability threshold $V_2(A)$ for $A > A^*$.

(II) The pulse speed

The speed of the pulse is determined by the discrete Nagumo Eq. (2.38) that describes the motion of the leading front. Analytical expressions for the front speed of the discrete Nagumo equation have been derived for two cases: (i) for small coupling strength, when D is close to the critical value D_c [96] and (ii) for large D, when the difference operator in the Nagumo equation can be approximated by the diffusion operator and a small correction term [4]. Here we utilize these theoretical results in order to estimate the dependence of the front speed on the stimulation parameter A.

For d close to d_c, the front speed of the Nagumo system written in the form of Eq. (2.44) has been derived in Ref. [96]. In the notations of Eq. (2.38) this reads:

$$c = \frac{\sqrt{3(D - D_c)}}{V_1 \left[\arctan\left(V_2\sqrt{3/(D - D_c)}/6\right) + \pi/2\right]}. \tag{2.52}$$

For large D, the expression for the front speed can be found in Ref. [98]:

$$c = c_0\sqrt{D}\left[1 - \tau_1(c_0)c_0^2/2D\right], \tag{2.53}$$

where

$$c_0 = (V_1 - 2V_2)/\sqrt{6} \tag{2.54}$$

and $c_0\sqrt{D}$ is the front speed in the spatially continuous case. The coefficient $\tau_1(c_0)$ depends on the front profile and can be computed according to the algorithm described in Ref. [98] (p. 279).

In Fig. 2.12, we show the dependence of the front speed on the stimulation parameter A computed from Eqs. (2.52) and (2.53) for small and large values of the coupling strength, respectively. We compare these analytical results with the results of direct numerical simulation of Eq. (2.38). We see that the accuracy of Eq. (2.52) is good in the regions of the parameter A, where the front speed approaches zero, i.e close to the thresholds of the propagation failure, and the accuracy declines beyond these regions. For large D, the discrete system can be well approximated by the continues model, and Eq. (2.53) provides an accurate estimate of the front speed for all A.

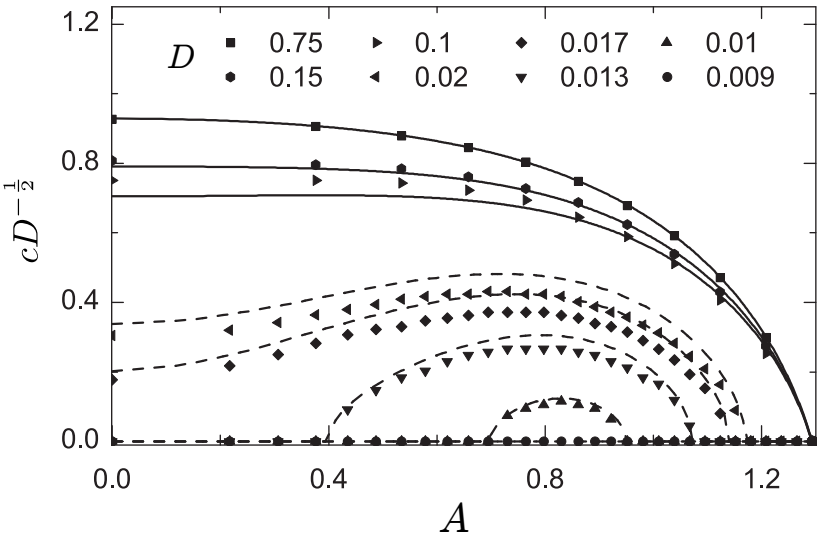

Figure 2.12: Scaled front speed $cD^{-1/2}$ as a function of the stimulation parameter A for different values of the coupling strength D. The dashed and solid curves represent analytical results obtained from Eqs. (2.52) and (2.53), respectively. The symbols show the results of numerical simulation of Eq. (2.38).

(III) The pulse length and propagation failure for a finite ε

For the spatially discrete system, the durations of the pulse overshoot T_O and undershoot T_U can be estimated in a similar manner as in the spatially continuous case (cf. [95, 98]):

$$T_O = \int_0^{\bar{W}} \frac{\mathrm{d}\delta w_n}{\varepsilon\left[R_3(\delta w_n) - \gamma\delta w_n\right]}, \tag{2.55}$$

$$T_U = \int_{\bar{W}}^0 \frac{\mathrm{d}\delta w_n}{\varepsilon\left[R_1(\delta w_n) - \gamma\delta w_n\right]}. \tag{2.56}$$

Equations (2.55) and (2.56) follow from Eqs. (2.40) and (2.43), respectively. The lengths of the pulse overshoot L_O and undershoot L_U measured in a number of nodes per corresponding segment can be estimated by multiplying the above times with the pulse speed:

$$L_O = cT_O = \frac{c}{\varepsilon}\int_{V_1}^{\tilde{R}_3} \frac{F'(\delta v_n)\mathrm{d}\delta v_n}{\delta v_n - \gamma F(\delta v_n)}, \tag{2.57}$$

$$L_U = cT_U = \frac{c}{\varepsilon}\int_{\tilde{R}_1}^{0} \frac{F'(\delta v_n)\mathrm{d}\delta v_n}{\delta v_n - \gamma F(\delta v_n)}. \tag{2.58}$$

Here the integral expressions are rewritten in a form convenient for numerical estimation. The integration variable δw_n is replaced by δv_n taking into account the relationship (2.39). The $F'(\delta v_n)$ denotes the derivative of the function $F(\delta v_n)$.

Note that the lengths L_O and L_U decrease as ε^{-1} with the increase of ε and the pulse ceases to exist at some $\varepsilon = \varepsilon_c$ when the shorter length L_O falls below 1. This condition defines a simple criterion for the pulse propagation failure at finite ε.

In Fig. 2.13 (a) and (b), we show the dependence of εL_O on the stimulation parameter A for different D. The solid curves are obtained from Eq. (2.57), while the symbols denote the results of direct numerical simulation of the averaged system (2.36). In fact, the variable εL_O provides an estimate for the critical value of the parameter ε at which the pulse ceases to exist, since $\varepsilon L_O = \varepsilon_c$ when $L_O = 1$. For large D [Fig. 2.13 (a)], the dependence of ε_c on A is monotonous and thus the HFS can cause only suppression of pulse propagation. For small D [Fig. 2.13 (b)], the non-monotonous dependence of ε_c on A makes possible both effects, the enhancement and suppression of the propagation. Note that for large D, the Eq. (2.57) approximates well the results of the averaged system (2.36), while for small D the accuracy of Eq. (2.57) declines.

To verify the law of proportionality $L_O \propto \varepsilon^{-1}$ anticipated by Eq. (2.57), in Fig. 2.13 (c) we present the dependence L_O on ε (for different values of A) in a double logarithmic scale. Then this dependence should take the form of straight lines. As is seen from the figure, the direct numerical simulations of the averaged Eqs. (2.36) indeed support this law for sufficiently small values of ε.

2.3.3 Numerical simulations of the original system

In the previous section, we have shown that the asymptotic theory described in Sec. 2.3.1 predicts rather well the properties of the averaged system (2.36) provided the parameter ε is sufficiently small. We recall that the system (2.36) has been derived from the original Eqs. (2.34) using the method of averaging. To support the validity of this approximation, the main effects of HFS observed in the averaged system (2.36) we now confirm by numerical simulations of the original system (2.34).

In Fig. 2.14 we show the solutions of Eqs. (2.34), which demonstrate the effect of enhanced pulse propagation under action of HFS. The value of the coupling strength is chosen sufficiently small, $D = 0.015$, so that for $\varepsilon = 0.0008$ the pulse cannot propagate in the free ($A = 0$) system. The simulations were performed with the boundary conditions $v_0 = v_1$, and $v_{N+1} = v_N$. The initial conditions for all elements were chosen equal to the fixed point of the averaged equations at the given stimulation intensity except for ten nodes in the middle of the sample, where the potential variable was enlarged by 2. In the part (a) of Fig. 2.14 the

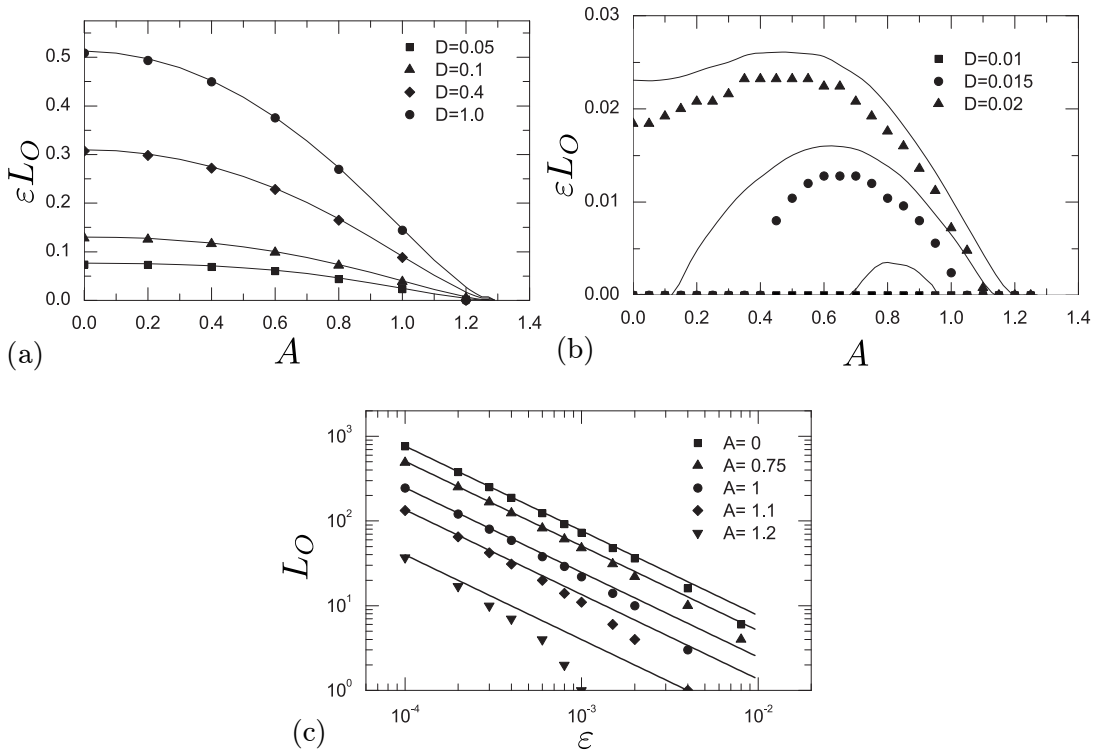

Figure 2.13: (a) and (b) The length of pulse overshoot multiplied by ε as a function of the stimulation parameter A for different values of the coupling strength D. (c) The dependence of the length of pulse overshoot on ε for fixed $D = 0.05$ and different values of A. Solid curves represent estimations based on the formula (2.57) while symbols show the results of direct numerical simulations of the averaged system (2.36). The length of pulse in (a) and (b) has been estimated from (2.36) for $\varepsilon = 0.0008$.

stimulation is off ($A = 0$) and the initial excitation of the middle nodes dies out, while in the part (b) the HFS of amplitude $A = 0.7$ cancels the propagation failure, and we observe two pulses propagating in different directions.

In order to test an influence of noise on the above effect, we performed simulations of the system (2.34) with the modified Eq. (2.34b):

$$\dot{w}_n = \varepsilon \left[v_n + \beta - \gamma w_n + \sigma \xi_n(t) \right]. \tag{2.59}$$

We added white Gaussian noise term $\sigma\xi_n(t)$ with $\langle \xi_n(t) \rangle = 0$ and $\langle \xi_n(t) \xi_{n'}(t') \rangle = \delta_{n,n'} \delta(t - t')$. Here the parameter σ governs the amplitude of noise, $\delta_{n,n'}$ is the Kronecker delta and $\delta(t)$ is the Dirac delta function. The results of simulations are presented in the parts (c) and (d) of Fig. 2.14. The small noise intensity $\sigma = 0.1$ in (c) does not influence the effect. However, sufficiently large noise may destroy the pulse propagation. In the part (d), we see that for $\sigma = 0.5$ the pulse

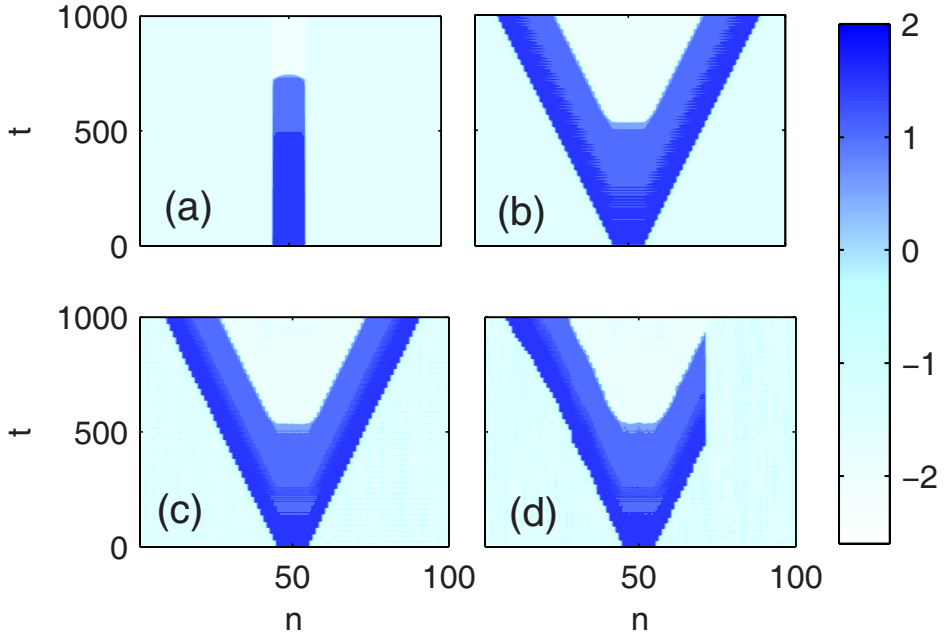

Figure 2.14: Spatio-temporal evolution of the membrane potential obtained from Eqs. (2.34) without noise [(a) and (b)] and from Eqs. (2.34a) and (2.59) in the presence of noise [(c) and (d)]. The background of homogeneous high-frequency oscillations is excluded by subtracting from the membrane potential the term $A\sin(\omega t)$ [cf. Eq. (2.35a)], i.e. the color encodes the value $v_n - A\sin(\omega t)$. The values of the fixed parameters are: $\omega = 10$, $N = 100$, $\varepsilon = 0.0008$ and $D = 0.015$. The variable parameters are: (a) $A = 0$, $\sigma = 0$, (b) $A = 0.7$, $\sigma = 0$, (c) $A = 0.7$, $\sigma = 0.1$ and (c) $A = 0.7$, $\sigma = 0.5$.

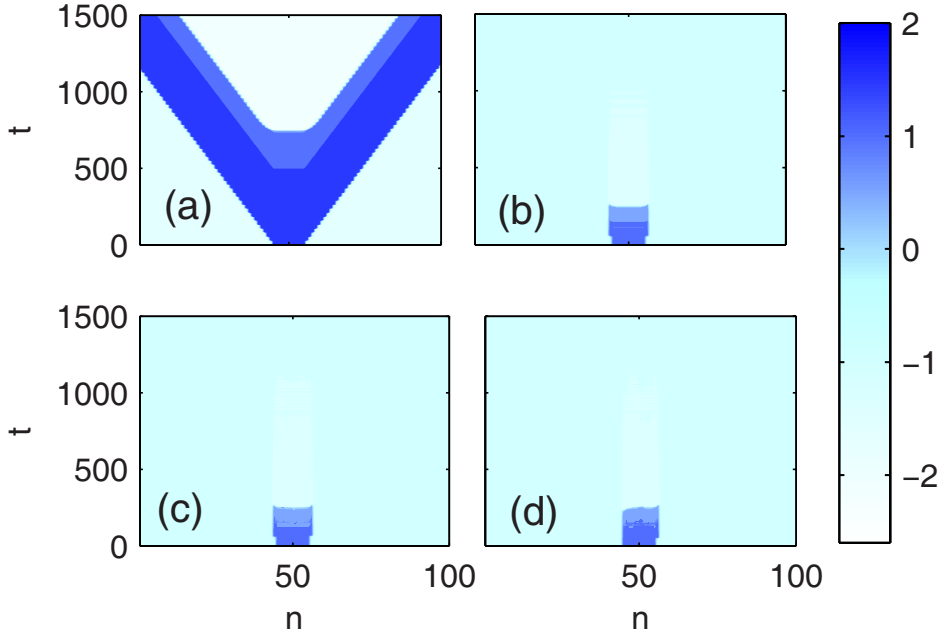

Figure 2.15: The same graphs as in Fig. 2.14 but the coupling strength is larger, $D = 0.02$, and the variable parameters are: (a) $A = 0$, $\sigma = 0$, (b) $A = 1.1$, $\sigma = 0$, (c) $A = 1.1$, $\sigma = 0.1$ and (c) $A = 1.1$, $\sigma = 0.5$.

propagating to the right dies out, while the pulse propagating to the left is not destroyed.

Notice that the effect of an enhanced propagation of a harmonic low-frequency signal under action of HFS has been observed in numerical simulations of the Barkley's model [99] in Ref. [100], but no theoretical treatment of the results has been presented. Moreover, the crucial role of the discreetness of the excitable system for the existence of this effect has not been highlighted.

In Fig. 2.15 we demonstrate the effect of suppression of pulse propagation. Here all the parameters are the same as in Fig. 2.14 except of the coupling strength, which is now increased to the value $D = 0.02$, so that the system without HFS admits pulse propagation. The two propagating pulses in the free system ($A = 0$) are shown in the part (a) of Fig. 2.15. The part (b) demonstrates the propagation failure in the presence of HFS with the amplitude $A = 1.1$. The parts (c) and (d) show the same effect when the noise is superimposed upon the system. We see that even large noise does not destroy the effect of propagation failure. This suggests that the effect of suppression of pulse propagation is less sensitive to the noise than the effect of enhancement of propagation.

2.4 Summary

We have analyzed the effect of a homogeneous high-frequency stimulation on the simple models of unmyelinated and myelinated axons described by spatially continuous and discrete FitzHugh-Nagumo equations. We have shown that, depending on the amplitude, the HFS may suppress the pulse propagation through the axon. Furthermore, the HFS may enhance the pulse propagation in the discrete systems. This differs essentially from the continuous case.

Our analysis is based on two main approximations. The first utilizes different time scales of the neuron and the high-frequency signal. Applying the method of averaging, we eliminate the high-frequency term and reduce the problem to the analysis of autonomous systems that describes the slow motion. It appears that the HFS influences the slow dynamics through a parameter A equal to the ratio of the amplitude to the frequency of HFS. The second approximation is related to the solution of the averaged equations. Here we utilize the smallness of the parameter ε that defines the ratio between the time scales of the membrane potential and the recovery variable. We adapt the asymptotic methods developed for the free FHN system and derive the main characteristics of the traveling pulse in the dependence of the stimulation parameter A.

As an important result of this approach, we have established an analytical criterion for the propagation failure and revealed the mechanism underling the effects of enhancement and suppression of pulse propagation. We have shown that the effects are related to the fact that the HFS of a small amplitude reduces the excitability threshold of excitable elements, while the HFS of a large amplitude increases the threshold. The validity of the above two approximations is supported by numerical simulations of the averaged equations and the original system.

The results of this section are published in Refs. [101, 102].

3. Controlling synchrony in oscillatory networks via act-and-wait method

In this chapter, we propose an algorithm for synchrony suppression in ensembles of globally coupled oscillators for a complicated control situation, when an output signal is small in comparison to a stimulated signal so that the reliable simultaneous registration and stimulation of the system is not possible, and the standard feedback control algorithms cannot be applied. Such a situation is typical for neuronal systems. Our algorithm is based on the act-and-wait control, which assumes a separation in time the registration and stimulation stages. In the registration (wait) stage, the mean field of the free oscillatory system is recorded in a memory and in the stimulation (act) stage it is fed back to the system. The periodic repetition of these two stages can effectively destroy the mutual synchronization in ensembles of globally coupled oscillators. Mathematically, this algorithm is described by delay differential equations with the periodically switched on and off time-delay feedback term. Although systems with time delay are usually associated with an infinity dimensional phase space, here the problem of stability of the incoherent state is defined by the eigenvalues of a finite dimensional monodromy matrix. This fact facilitates considerably the search for appropriate control parameters that guarantee the stability of the incoherent state.

The chapter is organized as follows. In Sec. 3.1 the act-and-wait algorithm is presented, its use in the linear systems and networks of oscillators are compared and the limit of small delay times is discussed. In Secs. 3.2 and 3.3 we apply the algorithm to an ensemble of globally coupled standard and modified Stuart-Landau (SL) oscillators. We present an analytical treatment of this problem in the thermodynamic limit. Section 3.4 is devoted to control of synchronization in synaptically coupled FitzHugh-Nagumo (FHN) neurons. Here we introduce a modification of our algorithm that takes into account the charge-balanced re-

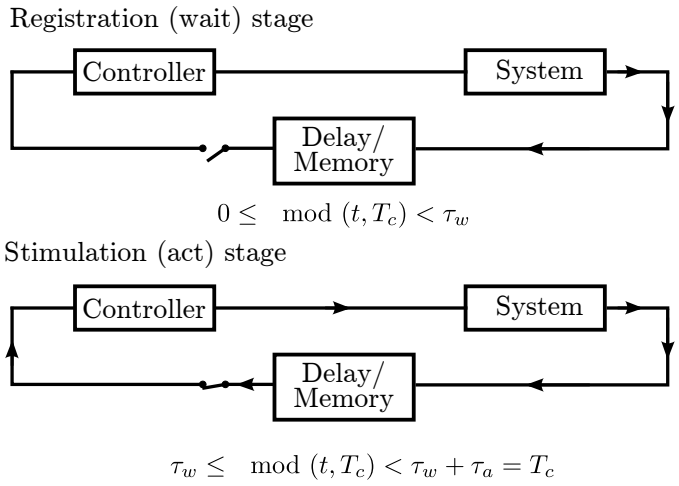

Figure 3.1: Block diagram of the algorithm with the separated in time registration (wait) and stimulation (act) setup. The wait and act stages are periodically repeated with the period $T_c = \tau_w + \tau_a$, where τ_w and τ_a are the durations of the wait and act stages, respectively. In the wait stage $0 \leq \mod(t, T_c) < \tau_w$, the mean field of the free neuronal population is recorded in a memory. In the act stage $\tau_w \leq \mod(t, T_c) < T_c$, the system is stimulated by memorized signal, previously processed by controller.

quirement. In Sec. 3.5 we apply our algorithm to an ensemble of realistic model neurons described by Hodgkin-Huxley (HH) equations. Finally, in Sec. 3.6 we conclude this chapter by summarizing our results.

3.1 Act-and-wait algorithm

In certain experimental systems, the implementation of feedback methods can meet fundamental problems. For example, in DBS the stimulation current exceeds the measured neuronal currents by several orders of magnitude, so that reliable registration of neuronal activity in the presence of simultaneous stimulation can be hardly achieved [103]. To avoid this problem we developed a feedback algorithm, called *the act-and-wait method*, where the processes of the stimulation and registration were separated in time. The block-diagram of our algorithm is presented in Fig. 3.1. The control process involves the periodic repetition of two stages. In the first stage, the mean field of the free neuronal population is registered and recorded in a memory, and in the second stage, the memorized signal is processed by a controller and fed back to the system.

Let's consider a typical neural network model under the act-and-wait control

$$\dot{v}_i = F_i(v_i, ..., v_N, \boldsymbol{w}_i) - PG(t)V(t-\tau), \tag{3.1a}$$

$$\dot{\boldsymbol{w}}_i = \boldsymbol{Q}_i(v_i, \boldsymbol{w}_i), \tag{3.1b}$$

where v_i represents ith's neuron voltage variable, while other variables are defined by the vector $\boldsymbol{w}_i$. The function $F_i(v_i, ..., v_N, \boldsymbol{w}_i)$ defines individual neuron's dynamics as well as the coupling between neurons. The last term in Eq. (3.1a) comes from control, where P is a feedback gain and function $G(t)$ is periodic switching function

$$G(t) = \begin{cases} 0, & 0 \leq \mod(t, T_c) < \tau_w, \\ 1, & \tau_w \leq \mod(t, T_c) < \tau_w + \tau_a = T_c. \end{cases} \tag{3.2}$$

so that the control force is switched off for a period of length τ_w (wait), and it is switched on for a period of length τ_a (act). Feedback is proportional to the measured mean field $V(t)$, which was generated by neurons, as in the experiments it is impossible to measure every neurons state in the brain.

In fact this algorithm for a different situation was introduced in the works of Insperger [104, 105]. The problem that authors were solving was the control of linear system, when due to physical limitations the feedback signal has some delay

$$\dot{\boldsymbol{x}}(t) = \boldsymbol{A}\boldsymbol{x}(t) - \boldsymbol{B}\boldsymbol{x}(t-\tau), \tag{3.3}$$

where $\boldsymbol{x}(t) \in \mathbb{R}^n$ is the state vector, $\boldsymbol{A} \in \mathbb{R}^{n\times n}$ constant matrix, $\boldsymbol{B} \in \mathbb{R}^{n\times n}$ is the control matrix and τ is delay time. The delay complicates the control, because the problem becomes infinite dimensional. This means that with a finite number of matrix $\boldsymbol{B}$ elements one has to control an infinite number of poles (also called characteristic roots or the characteristic exponents) determined by a transcendental characteristic equation

$$\det(\lambda \boldsymbol{I} - \boldsymbol{A} - \boldsymbol{B}\mathrm{e}^{-\tau\lambda}) = 0. \tag{3.4}$$

In order to overcome this problem Insperger suggested to change the control matrix $\boldsymbol{B}$ by

$$\boldsymbol{B} = \boldsymbol{P}G(t), \tag{3.5}$$

where $G(t)$ is periodic switching function defined in Eq. (3.2). As pointed out in Refs. [104, 105], if $\tau_a \leq \tau_w$ then this condition leads to an essential simplification of the time delay problem. For $\tau_a \leq \tau_w$, we can reduce the problem to a finite

dimensional map that relates the state variables of the system at the beginning of the $n+1$-st control period with the state variables at the beginning of the n-th control period, so that the stability of the controlled system is defined by eigenvalues of a finite dimensional monodromy matrix[1]. The idea can be simply explained by the example presented below.

Example: Stabilization of the exponential growth. Here we use the act-and-wait method for the stabilization of the zero fixed point $x^* = 0$ of the exponential growth

$$\dot{x} = \lambda x - PG(t)x(t-\tau), \tag{3.6}$$

where $\lambda > 0$. For the control we choose equal waiting, acting and delay times, i.e. $\tau_w = \tau_a = \tau$. Thus the control has two parameters P and τ, which have to be determined. Let's say that at the beginning of the n-th registration-stimulation period the system is at the state X_n. For the registration stage $t \in (0, \tau)$, the system evolves freely according to the exponential growth, thus for this period $x(t) = X_n \exp(\lambda t)$. During the stimulation stage the system evolves according to the equation

$$\dot{x} = \lambda x - PX_n \exp(\lambda t), \tag{3.7}$$

which, taking into account the initial condition, has the solution

$$x(t) = (\mathrm{e}^{\lambda\tau} - P\tau)\mathrm{e}^{\lambda t} X_n. \tag{3.8}$$

From this expression one can tell that in this case the monodromy matrix is just a scalar value $A(\tau) = (\mathrm{e}^{\lambda\tau} - P\tau)\mathrm{e}^{\lambda\tau}$, which relates Eq. (3.6) states at the beginning of the nth and $n+1$ stimulation-registration periods $X_{n+1} = (\mathrm{e}^{\lambda\tau} - P\tau)\mathrm{e}^{\lambda\tau} X_n$. Because of the fact that the investigated system is one-dimensional, the value of the monodromy matrix coincides with the Floquet multiplier. Therefore one can conclude that the act-and-wait algorithm stabilizes zero fixed point, when the absolute value of the Floquet multiplier $A(\tau)$ will be less than 1, or in other words, when parameters τ and P satisfy the inequality

$$|(\mathrm{e}^{\lambda\tau} - P\tau)\mathrm{e}^{\lambda\tau}| < 1. \tag{3.9}$$

[1] If we have the liner ODE

$$\dot{\boldsymbol{x}}(t) = \boldsymbol{C}(t)\boldsymbol{x}(t),$$

where matrix $\boldsymbol{C}(t) = \boldsymbol{C}(t+T)$ is T-periodic, then the monodromy matrix $\boldsymbol{A}(T)$ relates the given system's initial state $\boldsymbol{x}_0$ with the systems state after time T, i.e. $\boldsymbol{x}(T) = \boldsymbol{A}(T)\boldsymbol{x}_0$. The eigenvalues of the monodromy matrix, called Floquet multipliers, defines the stability of the periodic solutions.

The stabilization is the fastest when the Floquet multiplier is equal to 0, i.e. when $e^{\lambda\tau} = P\tau$. $\square$

Further we restrict ourselves to the case of equal act, wait and delay durations $\tau_a = \tau_w = \tau$. Then the period of act-and-wait switching is $T_c = 2\tau$ and the 2τ-periodic function $G(t)$ can be presented as

$$G(t) = H\left[-\sin(\pi t/\tau)\right], \tag{3.10}$$

where $H(\cdot)$ is the Heaviside step function.

The limit of small τ

For the limit of the small delays $\tau \to 0$ the control current in Eq. (3.1) can be approximated as

$$I_{\rm con}(t) = G(t)P[V(t) + O(\tau)]. \tag{3.11}$$

up to the first order in τ. Substituting Eq. (3.11) into Eq. (3.1) we get a nonautonomous system of ordinary differential equations with the high-frequency periodic function $G(t)$. Such a system can be treated by the method of averaging (see previous chapter or Ref. [88]). To transform our system to the standard form of equations as typically used by this method we rescale the time variable $\bar{t} = t/\tau$ (here $\bar{t}$ is the "fast" time) and obtain

$$\frac{dv_j}{d\bar{t}} = \tau\{F_j(v_1, \ldots, v_N, \boldsymbol{w}_j) - \tilde{G}(\bar{t})P[V + O(\tau)]\}, \tag{3.12a}$$

$$\frac{d\boldsymbol{w}_j}{d\bar{t}} = \tau \boldsymbol{Q}_j(v_j, \boldsymbol{w}_j). \tag{3.12b}$$

Due to the small factor τ, the variables v_j and $\boldsymbol{w}_j$ vary slowly while the periodic function $\tilde{G}(\bar{t}) \equiv G(\tau\bar{t}) = H[-\sin(\pi\bar{t})]$ oscillates fast. According to the method of averaging [88], an approximate solution of system (3.12) can be obtained by averaging the r.h.s. of the system over fast oscillations. Specifically, let us denote the variables of the averaged system as $(\bar{v}_j, \bar{\boldsymbol{w}}_j)$. They satisfy the equations:

$$\frac{d\bar{v}_j}{d\bar{t}} = \frac{\tau}{2}\int_0^2 \{F_j(\bar{v}_1, \ldots, \bar{v}_N, \bar{\boldsymbol{w}}_j) - \tilde{G}(s)P\bar{V}\}ds, \tag{3.13a}$$

$$\frac{d\bar{\boldsymbol{w}}_j}{d\bar{t}} = \frac{\tau}{2}\int_0^2 \boldsymbol{Q}_j(v_j, \bar{\boldsymbol{w}}_j)ds, \tag{3.13b}$$

where $\bar{V} = N^{-1}\sum_{j=1}^N \bar{v}_j$. The method of averaging states that the averaged system (3.13) approximates the solutions of the system (3.12) with the accuracy of $O(\tau)$, i. e., $v_j = \bar{v}_j + O(\tau)$ and $\boldsymbol{w}_j = \bar{\boldsymbol{w}}_j + O(\tau)$. After performing the integration (note

that $\int_0^2 \tilde{G}(s)ds = 1$) and coming back to the original time scale, the averaged system (3.13) takes the form:

$$\dot{\bar{v}}_j = F_j(\bar{v}_1, \ldots, \bar{v}_N, \bar{\boldsymbol{w}}_j) - P\bar{V}/2, \tag{3.14a}$$

$$\dot{\bar{\boldsymbol{w}}}_j = \boldsymbol{Q}_j(\bar{v}_j, \bar{\boldsymbol{w}}_j). \tag{3.14b}$$

Here the dot denotes differentiation with respect to the original time t. Thus the nonautonomous system (3.1) with the accuracy $O(\tau)$ can be transformed to the autonomous averaged system (3.14). The last term in Eq. (3.14a) describes the standard proportional feedback control with the strength $P/2$. Therefore, the act-and-wait control algorithm for $\tau \to 0$ transforms to the proportional feedback control algorithm.

3.2 Stuart-Landau oscillators coupled and controled via both variables

Consider an ensemble of N globally coupled and stimulated SL oscillators, representing a normal form of a supercritical Andronov-Hopf bifurcation

$$\dot{z}_j = (i\omega_j + 1 - |z_j|^2)z_j + KZ - PG(t)Z(t - \tau_a). \tag{3.15}$$

Here $z_j = x_j + iy_j$ is a complex valued variable, that defines the state of the jth oscillator, $j = 1, \ldots, N$. Without coupling ($K = 0$) and without stimulation ($P = 0$) each oscillator performs an uniform rotation with the natural frequency ω_j and amplitude 1. The oscillators are globally coupled via the mean field

$$Z = \frac{1}{N}\sum_{k=1}^{N} z_k. \tag{3.16}$$

We suppose that both components x and y of the complex variable z are coupled with the same coupling strength defined by the real valued parameter K. The last term in Eq. (3.15) describes the act-and-wait control force. The delayed mean field $Z(t-\tau_a)$, which is recorded in a memory during the wait period, is multiplied by the T_c-periodic act-and-wait switching function defined in (3.10).

3.2.1 Equation for the order parameter

To explore the advantages of the act-and-wait control algorithm we investigate the phase dynamics of the system (3.15). Substituting $z_j = \rho_j e^{i\theta_j}$ and neglecting the dynamics of the amplitudes ρ_j one can transform Eq. (3.15) to the following equation for the phases θ_j:

$$\dot{\theta}_j = \omega_j + [Kr - PG(t)r_\tau]e^{-i\theta_j}/2i + \text{c.c.}. \tag{3.17}$$

Here $r = r(t)$ is the complex order parameter

$$r = \frac{1}{N}\sum_{k=1}^{N} e^{i\theta_k} \tag{3.18}$$

and the subscript τ denotes the time delayed value $r_\tau(t) \equiv r(t-\tau)$. The abbreviation "c.c." stands for complex conjugate. Without control ($P = 0$), Eq. (3.17) represents the classical Kuramoto model [14]. We assume that the frequencies ω_j are randomly distributed according to a symmetric probability density function $g(\omega)$, $g(\Omega - \omega) = g(\Omega + \omega)$, where Ω is the central frequency. Then the critical coupling for spontaneous synchronization is [14, 16]: $K_c = 2/\pi g(\Omega)$. For $K < K_c$ the ensemble relaxes to the state, where all oscillators move incoherently, and for $K > K_c$ mutual synchronization occurs in a group of oscillators.

We now analyze the synchronization properties of the system in the presence of the act-and-wait control. We characterize the synchronization by the absolute value of the order parameter (3.18). The values of $|r|$ vary in the interval $[0, 1]$ such that small values indicate the incoherent state while the values close to 1 represent the strong mutual synchronization. To solve the problem analytically we analyze the system (3.17) in the thermodynamic limit $N \to \infty$. We describe the state of the oscillator system at time t by a continuous distribution function, $f(\omega, \theta, t)$, in frequency ω and phase θ that satisfies the normalization

$$\int_0^{2\pi} f(\omega, \theta, t)\mathrm{d}\theta = g(\omega) \tag{3.19}$$

for all t. Since oscillators are conserved f must satisfy the continuity equation

$$\frac{\partial}{\partial t} f(\omega, \theta, t) = -\frac{\partial}{\partial \theta}[f(\omega, \theta, t)v(\omega, \theta, t)], \tag{3.20}$$

where the velocity $v(\omega, \theta, t)$ is defined by the r.h.s. of Eq. (3.17)

$$v(\omega, \theta, t) = \omega + [Kr - PG(t)r_\tau]e^{-i\theta}/2i + \text{c.c.} \tag{3.21}$$

In the continuum limit, Eq. (3.18) can be written as

$$r = \int_0^{2\pi} \int_{-\infty}^{\infty} e^{i\theta} f(\omega, \theta, t) \mathrm{d}\omega \mathrm{d}\theta. \tag{3.22}$$

Expanding $f(\omega, \theta, t)$ in Fourier series in θ we have

$$f = \frac{g(\omega)}{2\pi} \left(1 + \left[\sum_{n=1}^{\infty} f_n(\omega, t) e^{in\theta} + \text{c.c.} \right] \right). \tag{3.23}$$

Following Ott and Antonsen [106], we restrict our analysis to a special class of distribution functions defined by the ansatz:

$$f_n(\omega, t) = [\alpha(\omega, t)]^n, \tag{3.24}$$

where $|\alpha(\omega, t)| \leq 1$ to avoid divergence of the series. Substituting this series expansion into Eqs. (3.20) and (3.22) we find that this special form of f satisfies Eqs. (3.20) and (3.22) if

$$\dot{\alpha} = \frac{K}{2}(r^* - r\alpha^2) - i\omega\alpha + \frac{G(t)}{2}(P\alpha^2 r_\tau - P^* r_\tau^*) \tag{3.25}$$

and

$$r = \int_{-\infty}^{+\infty} \alpha^*(\omega, t) g(\omega) \mathrm{d}\omega. \tag{3.26}$$

Further simplification can be gained by choosing the density distribution of the natural frequencies in the Lorentzian function form

$$g(\omega) = g_L(\omega) \equiv (\Delta/\pi) \left[(\omega - \Omega)^2 + \Delta^2 \right]^{-1}, \tag{3.27}$$

where Δ defines the width of the distribution. This form allows us to solve the ω integral in Eq. (3.26) and obtain an explicit relation $r^*(t) = \alpha(\Omega - i\Delta, t)$. Putting this result into Eq. (3.25) and setting $\omega = \Omega - i\Delta$ we finally get a closed equation for the complex order parameter

$$\dot{r} = \left[i\Omega - \Delta + \frac{K}{2}(1 - |r|^2) \right] r + \frac{G(t)}{2}(P^* r^2 r_\tau^* - P r_\tau). \tag{3.28}$$

This equation is considerably simpler than the original system (3.15) and allows for

the direct analysis of the influence of the act-and-wait control on the macroscopic properties of the system. From this equation it follows, that without control ($P = 0$) the order parameter $r(t)$ experiences the Andronov-Hopf bifurcation when the coupling strength K is increased. For $K < K_c = 2\Delta$, the order parameter relaxes to the stable fixed point $r = 0$, which means the incoherent state of the oscillator system. When the coupling exceeds the critical value $K > K_c$, the fixed point loses the stability and r approaches the stable limit cycle with the amplitude $|r| = (1 - K_c/K)^{1/2}$ and frequency Ω. This corresponds to a partial synchronization, which becomes more and more stronger when K is increased. For $K \to \infty$ the systems tends to the fully synchronized state, since $|r| \to 1$. Below we analyze how this scenario changes in the presence of the act-and-wait control.

(I) Linear stability analysis

We now consider an influence of the act-and-wait control on the dynamics of the order parameter defined by Eq. (3.28). The goal of the control is to suppress the synchronization that we assume to exist in the free system due to a large global coupling, i.e., we take $K > K_c$, so that the fixed point $r = 0$ of the free system is unstable. The incoherent state can be rebuilt by control if the last term in Eq. (3.28) proportional to $G(t)$ stabilizes the fixed point. To analyze the stability of the fixed point we first rewrite system (3.28) in the rotating frame with the mean frequency Ω by changing the variable $r = e^{i\Omega t}R$. Then linearizing the system with respect to small R we obtain

$$\dot{R} = (K/2 - \Delta)\, R - G(t) P e^{-i\Omega\tau} R_\tau/2. \tag{3.29}$$

The change of the coordinate system does not change the absolute value of the order parameter, $|R| = |r|$. To analyze the stability of the fixed point $R = 0$ it is useful to rewrite Eq. (3.29) in terms of real valued coordinates $x + iy = R$,

$$\begin{pmatrix} \dot{x} \\ \dot{y} \end{pmatrix} = \lambda \begin{pmatrix} x \\ y \end{pmatrix} - G(t) \begin{pmatrix} \bar{P}_x & -\bar{P}_y \\ \bar{P}_y & \bar{P}_x \end{pmatrix} \begin{pmatrix} x_\tau \\ y_\tau \end{pmatrix}. \tag{3.30}$$

Here we introduced the notations $\lambda = K/2 - \Delta > 0$, $\bar{P}_x = |P| \cos(\varphi - \Omega\tau)/2$ and $\bar{P}_y = |P| \sin(\varphi - \Omega\tau)/2$, where φ is the argument of the complex valued parameter $P = |P| e^{i\varphi}$.

Though the system (3.30) contains time delay feedback terms, which are usu-

ally associated with an infinite dimensional phase space, it can be transformed to a finite-dimensional map (c.f. [104, 105]). Such a transformation is possible due to the presence of the periodic act-and-wait switching function $G(t)$. Denote the state variables of the system at the beginning of the n-th act-and-wait control period by $x_n = x(2\tau n)$ and $y_n = y(2\tau n)$. Then for the wait period $2\tau n \leq t < 2\tau n + \tau$ the parameter $G(t) = 0$ and we obtain the solution of (3.30) as $x(t) = x_n e^{\lambda(t-2\tau n)}$ and $y(t) = y_n e^{\lambda(t-2\tau n)}$. In the next act period $2\tau n + \tau \leq t < 2\tau(n+1)$, the parameter $G(t) = 1$ so that the time delay functions x_τ and y_τ come into play. These functions are exactly the above solutions obtained in the wait stage, so that here Eq. (3.30) represents a linear non-autonomous system. Solving this system we find the values of the state variables at the end of the act stage and finally obtain the map

$$\begin{pmatrix} x_{n+1} \\ y_{n+1} \end{pmatrix} = \boldsymbol{A} \begin{pmatrix} x_n \\ y_n \end{pmatrix}, \tag{3.31}$$

where

$$\boldsymbol{A} = e^{\lambda\tau} \begin{pmatrix} -\tau\bar{P}_x + e^{\lambda\tau} & \tau\bar{P}_y \\ -\tau\bar{P}_y & -\tau\bar{P}_x + e^{\lambda\tau} \end{pmatrix} \tag{3.32}$$

is the monodromy matrix. The eigenvalues $\mu_{1,2}$ of this matrix defined by the characteristic equation

$$\det(\boldsymbol{A} - \boldsymbol{I}\mu) = 0, \tag{3.33}$$

are responsible for the stability of the system (3.30). The origin of this system is stable if the both eigenvalues are inside the unit circle in the complex plane, $|\mu_{1,2}| < 1$. From Eqs. (3.32) and (3.33) we obtain

$$|\mu_{1,2}| = e^{\lambda\tau} \left[(\tau\bar{P}_x - e^{\lambda\tau})^2 + \tau^2 \bar{P}_y^2 \right]^{1/2}. \tag{3.34}$$

Thus despite the presence of time delayed feedback the stability of the system is defined by only two eigenvalues. By appropriate choice of the two control parameters $\bar{P}_x$ and $\bar{P}_y$ both eigenvalues can be easily placed inside the unit circle. As is seen from Eq. (3.34) the parameter $\bar{P}_y$ plays destructive role; it can only enhance the values of $|\mu_{1,2}|$. Thus the best choice is to make it zero, $\bar{P}_y = 0$. In terms of the initial complex valued parameter P this means that we fix its argument at $\varphi = \Omega\tau$, i.e., choose the feedback strength in the form $P = |P|e^{i\Omega\tau}$. Then on substitution of $\bar{P}_x = |P|/2$ and $\bar{P}_y = 0$ into Eq. (3.34) the criterion of the stability simplifies to

$$|\mu_{1,2}| = \left| e^{\lambda\tau} - |P|\tau/2 \right| e^{\lambda\tau} < 1.$$

From this it follows that the act-and-wait control force can stabilize the incoherent state of strongly coupled ($K > K_c$) SL oscillators if the feedback strength satisfies the inequalities

$$P_{\rm mn} < |P| < P_{\rm mx}, \tag{3.35}$$

$$P_{\rm mx,mn} = 2\left[e^{(K/2-\Delta)\tau} \pm e^{(-K/2+\Delta)\tau}\right]/\tau. \tag{3.36}$$

The optimal value of the feedback strength is attained at $|P| = 2e^{\lambda\tau}/\tau$, when the both eigenvalues vanish $|\mu_{1,2}| = 0$ and the incoherent state becomes superstable.

(II) Numerical simulations

To demonstrate the efficacy of the act-and-wait control algorithm and verify the validity of the above analytical theory we have numerically simulated an ensemble of $N = 1000$ globally coupled Stuart-Landau oscillators described by Eqs. (3.15). The natural frequencies ω_j were randomly chosen from the Lorentzian distribution (3.27) with $\Omega = 0.25\pi$ and $\Delta = 0.1$. The coupling strength $K = 0.5$ was taken far away above the critical value of the spontaneous synchronization, $K_c = 2\Delta = 0.2$. In this case Eq. (3.28) predicts rather large stationary value of the order parameter of the uncontrolled system, $|r| = (1 - K_c/K)^{1/2} \approx 0.77$. In Fig. 3.2(a), the dynamics of the order parameter (3.18) computed by direct integration of the system (3.15) is presented by blue (dark) curve. For $t < 100$, the control is not activated and the order parameter fluctuates with a small amplitude around the predicted value $|r| = 0.77$. When the act-and-wait control is switched on ($t \geq 100$) the oscillator system approaches suddenly the incoherent state and the value of the order parameter falls to zero. In the same figure, we also show [by red (grey) curve] the dynamics of the order parameter obtained from the macroscopic Eq. (3.28). We see that the solution of this equation reproduces well the results obtained from the direct integration of the oscillator system (3.15). This confirms the validity of Ott-Antonsen ansatz (3.24), which allowed us to find an analytical solution of the continuity Eq. (3.20) in the presence of the act-and-wait control. In panel (b) of Fig. 3.2, we demonstrate how the act-and-wait control changes the dynamics of individual oscillators, by taking the first three oscillators as an example.

Incoherent state stability domains in the plane of parameters $(\tau, |P|)$ are presented in Fig. 3.3. The linear theory predicts the domain of stability lying between two thick black curves $P_{\rm mx,mn}(\tau)$ defined by Eqs. (3.35) and (3.36). In panels (a) and (b), the values of the order parameter evaluated from the solutions of Eqs. (3.28) and (3.15), respectively, are encoded in color. We see that

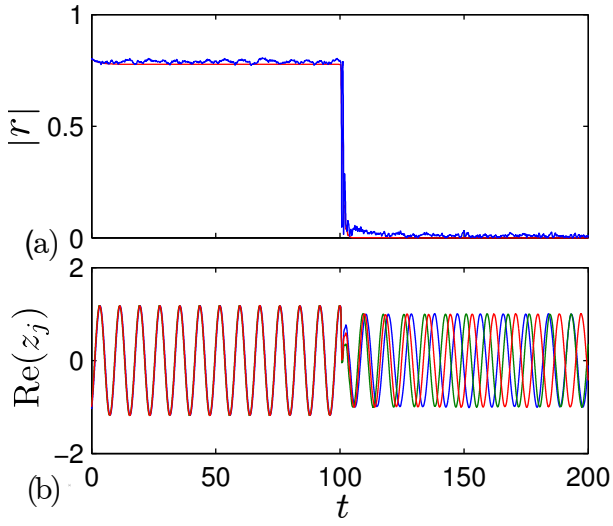

Figure 3.2: Dynamics of $N = 1000$ globally coupled Stuart-Landau oscillators (3.15) under act-and-wait control. For $t < 100$ the control is off ($|P|$=0), while for $t \geq 100$ the act-and-wait control with the feedback strength $|P| = 4$ is activated. (a) Absolute value of the order parameter estimated from direct integration of Eqs. (3.15) [blue (dark)] and from macroscopic Eq. (3.28) [red (grey)]. (b) Dynamics of the first three oscillators. The values of the parameters are: $K = 0.5$, $\Omega = 0.25\pi$, $\Delta = 0.1$ and $\tau = 0.4$. The complex feedback strength is chosen in the form $P = |P|e^{i\Omega\tau}$.

the linear theory predicts well the results obtained from solution of the nonlinear Eq. (3.28) for the order parameter. However, the prediction for the original system (3.15) of SL oscillators is limited. Here the linear theory predicts well only the lower boundary $|P| = P_{\mathrm{mn}}(\tau)$ of the stability domain, but with the increase of $|P|$ the oscillators start to synchronize before $|P|$ reaches the upper boundary $|P| = P_{\mathrm{mx}}(\tau)$. Such a discrepancy between the results obtained from Eqs. (3.15) and (3.28) is explained by the fact that for large $|P|$ the act-and-wait control force influences not only the phases of the individual oscillators but the amplitudes as well. Therefore, for large $|P|$ we cannot neglect the dynamics of the amplitudes and substitute the original system (3.15) by the Kuramoto model (3.17) that takes into account only the dynamics of the phases.

3.3 Coupling and control via a single variable

We now consider a situation typical for neuronal systems where the interaction between neurons is provided by a single variable, the membrane potential, while the other (gate) variables do not participate directly in the interaction. Electrical stimulation acts directly also only on the membrane potential of neurons. We can

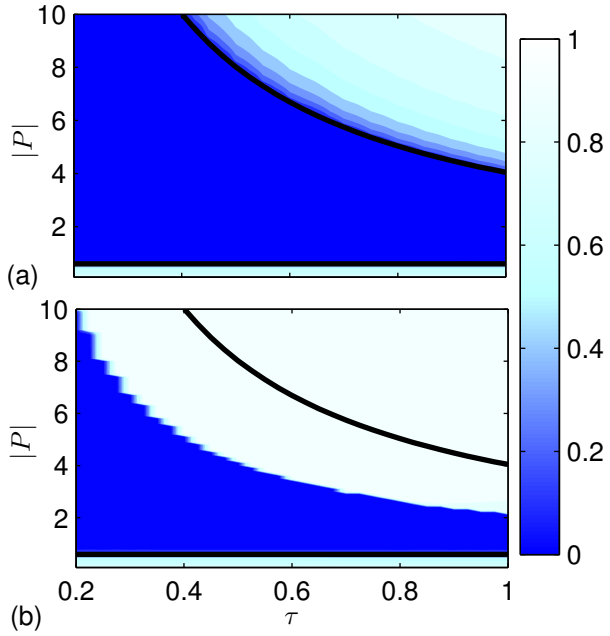

Figure 3.3: Incoherent state stability domains in the plane of parameters $(\tau, |P|)$ for the Stuart-Landau oscillators (3.15) controlled by the act-and-wait algorithm. The thick black curves represent the boundaries of stability $P_{\mathrm{mx,mn}}(\tau)$ defined by Eqs. (3.36). The color encodes the absolute value $|r|$ of the order parameter estimated from (a) Eq. (3.28) and (b) Eqs. (3.15). The values of the parameters are: $N = 1000$, $K = 0.5$ and $\Delta = 0.1$. The computations are performed in the rotating coordinate frame where $\Omega = 0$.

mimic this situation by modifying the system (3.15) as follows:

$$\dot{z}_j = (i\omega_j + 1 - |z_j|^2)z_j + K\mathrm{Re}Z - PG(t)\mathrm{Re}Z(t-\tau). \tag{3.37}$$

Here, unlike to Eqs. (3.15), the term of the global coupling and the act-and-wait control force are applied only to the real part of SL equations. We assume that both, the coupling strength K and the feedback strength P, are real valued parameters.

Similar as in Sec. 3.2.1, we neglect the dynamics of the amplitudes and derive an equation for the phases

$$\dot{\theta}_j = \omega_j - \sin(\theta_j)\mathrm{Re}\left[Kr - G(t)Pr_\tau\right]. \tag{3.38}$$

Now assuming that the natural frequencies are distributed by the Lorentzian law (3.27) and repeating the procedure presented in Sec. 3.2.1 one can show that in

the thermodynamic limit $N \to \infty$, the order parameter obeys the equation

$$\dot{r} = (i\Omega - \Delta)r + \frac{1-r^2}{2}\left[K\mathrm{Re}(r) - G(t)P\mathrm{Re}(r_\tau)\right]. \tag{3.39}$$

To analyze the stability of the incoherent state $r = 0$, we rewrite Eq. (3.39) in terms of real valued coordinates $x + iy = r$ and linearizing it with respect to the fixed point $(x, y) = (0, 0)$, obtain

$$\begin{pmatrix} \dot{x} \\ \dot{y} \end{pmatrix} = \begin{pmatrix} K/2 - \Delta & -\Omega \\ \Omega & -\Delta \end{pmatrix} \begin{pmatrix} x \\ y \end{pmatrix} - G(t)\frac{P}{2}\begin{pmatrix} x_\tau \\ 0 \end{pmatrix}. \tag{3.40}$$

From this it follows that the incoherent state of the control free ($P = 0$) system is unstable for $K > K_c = 4\Delta$. We suppose that this inequality is fulfilled and look for the act-and-wait control parameters (τ, P), which lead to the stabilization of the zero fixed point of the system (3.40). As well as in Sec. 3.2.1, an analytical solution of this system can be written in the form of Eq. (3.31). However, an expression for the monodromy matrix is now much more complicated and we do not present it here. Generally, analytical expressions for the stability domains in the (τ, P) plane are not available, but they can be easily estimated numerically.

An exception where an analytical result can be gained is the case of small τ. As it is shown in the Sec. 3.1, for $\tau \to 0$, the system (3.37) can be treated by the method of averaging and its solution can be approximated as $z_j \approx \bar{z}_j$, where $\bar{z}_j$ satisfy the averaged equations

$$\dot{\bar{z}}_j = (i\omega_j + 1 - |\bar{z}_j|^2)\bar{z}_j + (K - P/2)\mathrm{Re}\bar{Z} \tag{3.41}$$

with $\bar{Z} = N^{-1}\sum_{j=1}^{N}\bar{z}_j$. By comparison of Eqs. (3.41) and (3.37) we see that for $\tau \to 0$ the act-and-wait control transforms to the proportional feedback control. On the other hand, Eq. (3.41) can be treated as a control-free equation but with the modified coupling strength $K \to K - P/2$. Then from Eq. (3.40) we obtain a simple criterion for the stability of the incoherent state

$$P > 2(K - 4\Delta). \tag{3.42}$$

The results of numerical simulations of Eqs. (3.37), (3.39) and the linear stability analysis based on Eq. (3.40) are presented in Figs. 3.4 and 3.5. In Fig. 3.4, we choose the values of the parameters $\Delta = 0.1$ and $K = 1 > K_c = 0.4$ so that the control-free system is synchronized ($|r| \approx 0.78$) and show that the switch-

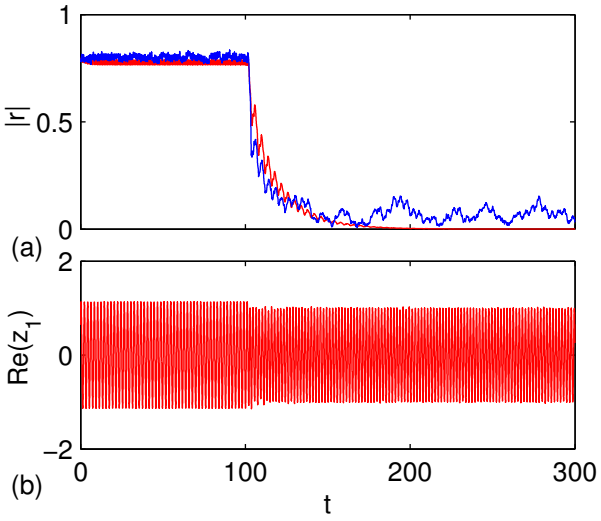

Figure 3.4: Dynamics of globally coupled $N = 1000$ Stuart-Landau oscillators (3.37) under act-and-wait control. For $t < 100$ the control is off (P=0), while for $t \geq 100$ the act-and-wait control with the feedback strength $P = 1.5$ is activated. (a) Absolute value of the order parameter estimated from direct integration of Eqs. (3.37) [blue (dark)] and from macroscopic Eq. (3.39) [red (grey)]. (b) Dynamics of the first oscillator. The values of the parameters are: $K = 1$, $\Omega = \pi$, $\Delta = 0.1$ and $\tau = 2$.

ing on the act-and-wait control leads to the desynchronization characterized by a small value of the order parameter. The dynamics of the order parameter [panel (a)] obtained from Eq. (3.39) agree well with the results of direct simulation of Eqs. (3.37). In panel (b), we show the dynamics of the first oscillator. The results of the linear stability analysis are presented in Fig. 3.5 (thick black curves). Incoherent state stability domains in the (τ, P) plane have a resonance structure; they are located at the values of $\tau = mT/2$, where $T = 2\pi/\Omega$ is the mean natural period of the oscillators and $k = 0, 1, 2, \ldots$ is a nonnegative integer number. The feedback strength P in these domains change the sign depending on m being odd or even number. In panels (a) and (b) the values of the order parameter evaluated from the solutions of Eqs. (3.39) and (3.37), respectively, are encoded in color. The linear theory predicts well the results obtained from solution of the nonlinear Eq. (3.39), however, the prediction for the original system (3.37) is limited. This limitation is again due to ignoring the dynamics of oscillator amplitudes in the transition from the original system (3.37) to the Kuramoto model (3.38). Note that for the given values of the parameters, the analytical condition (3.42) derived for $\tau \to 0$ reads $P > 1.2$. This is in good agreement with the numerical results presented in Fig. 3.5.

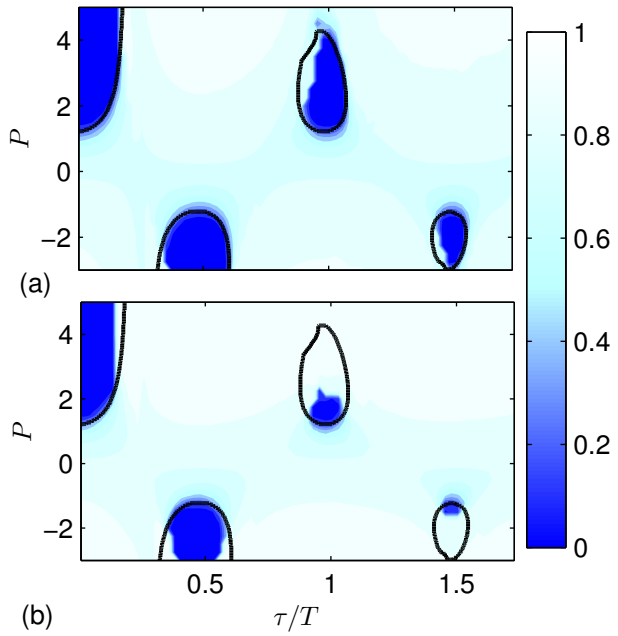

Figure 3.5: Incoherent state stability domains in the plane of parameters (τ, P) for the Stuart-Landau oscillators (3.37) controlled by the act-and-wait algorithm. The thick black curves represent the boundaries of stability derived from linear Eq. (3.40). The color encodes the absolute value $|r|$ of the order parameter estimated from (a) Eq. (3.39) and (b) Eqs. (3.37). The values of the parameters are: $N = 1000$, $K = 1$, $\Delta = 0.1$, $\Omega = \pi$ and $T = 2\pi/\Omega$.

3.4 Synaptically coupled FitzHugh-Nagumo neurons

We now test the efficacy of the act-and-wait control for neuronal systems. We start from a simple model of synaptically coupled FitzHugh-Nagumo [6,7] neurons

$$\dot{v}_j = f(v_j) - w_j + I_j - I_{\text{syn}} - I_{\text{con}}, \tag{3.43a}$$

$$\dot{w}_j = \varepsilon(v_j + \beta - \gamma w_j). \tag{3.43b}$$

Here the variable v_j denotes the membrane potential and w_j is the recovery variable of j-th neuron ($j = 1, \ldots, N$), $f(v_j) = v_j - v_j^3/3$ is the cubic source term of an ionic current, I_j is a stimulus current that defines the spiking frequency of the free neuron, I_{syn} stands for the synaptic current of the j-th neuron due to connection with other neurons and I_{con} is the current generated by the act-and-wait control algorithm. The constant $\varepsilon > 0$ is the ratio between the characteristic time scales

of v_j and w_j variables. We choose the standard values of the parameters $\varepsilon = 0.2$, $\gamma = 0.8$ and $\beta = 0.7$.

In order to spread the natural spiking frequencies of neurons, the stimulus currents I_j are generated by a normal distribution with the mean value $\langle I \rangle = 1$ and the standard deviation $\sigma = 0.1$. We assume that neurons are globally coupled via a synaptic current defined as

$$I_{\text{syn}} = g(v_j - v_c)\frac{1}{N-1}\sum_{k\neq j}\Theta(v_k - v_0), \tag{3.44}$$

where $\Theta(v) = 1/[1 + \exp(-v/v_{\text{th}})]$ is a sigmoid function with the characteristic threshold parameter v_{th} and v_c is the reversal potential. We choose the parameters of synaptic current in such a way as to model an excitatory coupling; each generated spike speeds up other neurons to generate spikes, so that without control ($I_{\text{con}} = 0$) the population spikes in synchrony. Then we seek to suppress the synchronization by an external current constructing in the form of the act-and-wait control

$$I_{\text{con}}(t) = G(t)PV(t-\tau), \tag{3.45}$$

where

$$V(t) = \frac{1}{N}\sum_{k=1}^{N} v_k(t). \tag{3.46}$$

is the mean field of membrane potential, which we assume is accessible for the measurement. The parameter P defines the feedback strength, and the 2τ-periodic act-and-wait switching function $G(t)$ is defined by Eq. (3.10).

3.4.1 Criteria of synchronization and numerical results

In coupled and controlled neuronal population the individual phases of neurons can be defined as in Ref. [13]:

$$\theta_j(t) = 2\pi\frac{t - t_k^{(j)}}{t_{k+1}^{(j)} - t_k^{(j)}}, \quad t_k^{(j)} \leq t \leq t_{k+1}^{(j)}. \tag{3.47}$$

Here $t_k^{(j)}$ are the moments when the membrane potential of the j-th neuron reaches the maximum. Using this phase definition we can characterize the synchronization between neurons by the standard order parameter $r = N^{-1}\sum_{j=1}^{N} e^{i\theta_j}$. The dynamics of this characteristic for $N = 500$ synaptically coupled FHN neurons is presented in Fig. 3.6 (a). For $t < 1500$, when the control is off ($I_{\text{con}} = 0$), the value of the order parameter is close to one. This indicates a highly synchronized

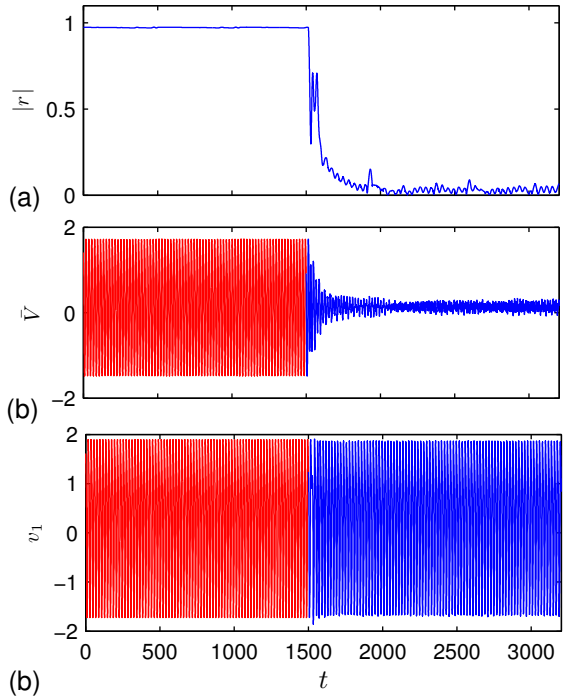

Figure 3.6: Dynamics of $N = 500$ synaptically coupled FitzHugh-Nagumo neurons (3.43) under act-and-wait control. For $t < 1500$ the control is off (I_{con}=0), while for $t \geq 1500$ the act-and-wait control (3.45) with the parameters $\tau = 18.5$ and $P = 0.2$ is activated. (a) Absolute value of the order parameter, (b) the mean field of membrane potential (3.46) and (c) the membrane potential of the first neuron. The values of the parameters are: $\varepsilon = 0.2$, $\beta = 0.7$, $\gamma = 0.8$, $v_0 = 1$, $v_c = 2.8$, $g = 0.05$ and $v_{\text{th}} = 0.1$.

state induced by synaptic interjection. Then for $t > 1500$ the synchronization is effectively suppressed, when the control current (3.45) with appropriate values of the parameters $\tau = 18.5$ and $P = 0.2$ is switched on. Here the order parameter falls to values close to zero. The effect of synchronization suppression is also observed in the dynamics of the mean field (3.16) presented in panel (b). When neurons are synchronized ($t < 1500$), the mean field oscillates with an amplitude comparable to the amplitude of individual neurons, but incoherently spiking neurons ($t > 1500$) produce mean field oscillations with a small amplitude. In order to demonstrate that the act-and-wait control does not destroy the spiking of individual neurons, in panel (c) we show the dynamics of the first neuron, as an example.

The phase definition (3.47) is not universal and its use becomes problematic when the dynamics of individual neurons is complex. Such a complex dynamics appears, e.g., for the values of the act-and-wait control parameters that do not succeed in the desynchronization. Thus for more detailed analysis of outcomes

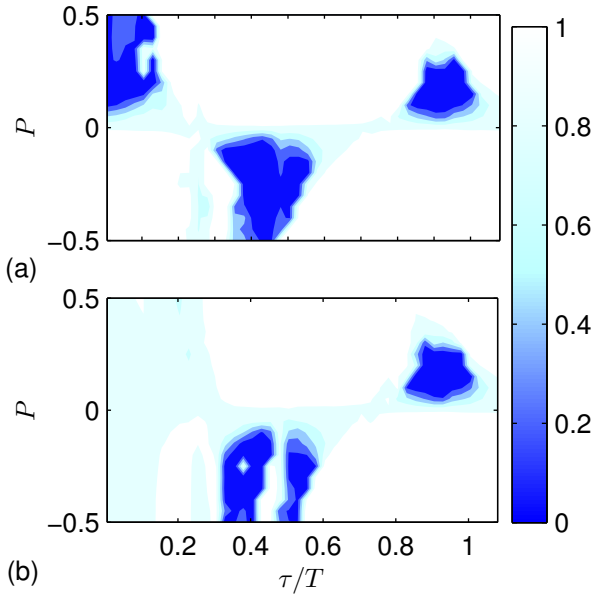

Figure 3.7: Performance of the act-and-wait control algorithm for synaptically coupled FHN neurons (3.43): (a) control law (3.45) without charge-balanced requirement and (b) control law (3.50) with the charge-balanced requirement. The color in the (τ, P) parameter plane encodes the value of the synchronization criterion S defined by Eq. (3.48). Incoherent states are characterized by small values of S. The period of the mean field oscillations of the coupled control-free neurons is $T \approx 19.8$ and other parameters are the same as in Fig. 3.6.

of the act-and-wait control algorithm we need an alternative, more universal, criterion of synchronization. Below we use the criterion based on the comparison of mean fields of the controlled and uncontrolled systems [73]:

$$S = [\mathrm{Var}(V_{\mathrm{stim}})/\mathrm{Var}(V_{\mathrm{free}})]^{1/2}. \tag{3.48}$$

The parameter S is defined as a square root of the ratio between the variances of the mean fields of the controlled $\mathrm{Var}(V_{\mathrm{stim}})$ and control free $\mathrm{Var}(V_{\mathrm{free}})$ system. In the synchronized state, when all neurons spike simultaneously, the value of this parameter is close to one, while in the incoherent state it is close to zero.

In Fig. 3.7 (a), we present the results of numerical computation of the parameter S dependence on the act-and-wait control parameters τ and P. The values of S in the $(\tau,\ P)$ plane are depicted in color code. We see that the incoherent state domains have a resonance structure similar to that obtained for the Stuart-Landau oscillators (see Fig. 3.5). They are located at $\tau = mT/2$, where $T \approx 19.8$ is the period of the mean field oscillations of the coupled control-free neurons and $m = 0, 1, 2, \ldots$ is a nonnegative integer number. The odd m defines the domains with positive values of P, while the even m corresponds to the negative P.

3.4.2 Charge-balanced stimulation

In practice, electrical neuron stimulation algorithms require some additional constraints. One of them is that the control current has not to accumulate charge in the cell, i.e., the control current integrated over the period of stimulation has to vanish. This so-called charge-balanced stimulation requirement is clinically mandatory to avoid tissue damage [107, 108]. Such a requirement can be easily satisfied by a simple modification of the act-and-wait control algorithm as follows. For each n-th wait stage we estimate the mean value of the recorded signal

$$\bar{V}_n = \frac{1}{\tau}\int_{2n\tau}^{(2n+1)\tau} V(t)dt \tag{3.49}$$

and then in the following act stage we subtract this value from the recorded signal, i.e., instead of the control current (3.45) we apply the current in the form:

$$I_{\text{con}}(t) = G(t)P\left[V(t-\tau) - \bar{V}_n\right]. \tag{3.50}$$

As is seen from Fig. 3.7 (b) this algorithm is successful as well as the algorithm without charge-balanced requirement, whose performance is presented in panel (a) of the same figure. The only qualitative effect induced by charge-balanced requirement is that the act-and-wait control technique stops working for small values of τ. Comparing panels (a) and (b) we see that the domain of successful desynchronization at small τ exists in (a) and disappears in (b). This effect can be explained by repeating the steps introduced in the Sec. 3.1, where the limit case was investigated. The analysis will show that at the limit $\tau \to 0$ the control current also vanishes $I_{\text{con}} \to 0$.

3.5 Hodgkin-Huxley neurons under a charge-balanced act-and-wait control

As a last example demonstrating the efficacy of our algorithm we consider synchronization control in an ensemble of synaptically coupled realistic model

neurons described by the Hodgkin–Huxley equations [3]:

$$\begin{aligned} C\dot{v}_j &= -g_{Na}m_j^3h_j(v_j - v_{Na}) - g_K n_j^4(v_j - v_K) \\ &\quad - g_L(v_j - v_L) + I_j + I_{\text{syn}} + I_{\text{con}}, \qquad (3.51a) \\ \dot{m}_j &= \alpha_m(v_j)(1 - m_j) - \beta_m(v_j)m_j, \qquad (3.51b) \\ \dot{h}_j &= \alpha_h(v_j)(1 - h_j) - \beta_h(v_j)h_j, \qquad (3.51c) \\ \dot{n}_j &= \alpha_n(v_j)(1 - n_j) - \beta_n(v_j)n_j. \qquad (3.51d) \end{aligned}$$

Here v_j is the membrane potential of the j-th neuron ($j = 1, \ldots, N$) measured in mV. We take the standard values of the parameters: $C = 1\ \mu\text{F/cm}^2$, $(v_L, v_K, v_{Na}) = (10.6, -12, 115)$ mV, $(g_L, g_K, g_{Na}) = (0.3, 36, 120)$ mS/cm^2. The rate parameters defining the dynamics of the gating variables m_j, h_j and n_j are defined in Eqs. (1.6). The voltage scale in this model is shifted in such a way that the membrane resting potential (i.e., the steady state value of the membrane potential without external currents, $I_j = I_{\text{syn}} = I_{\text{con}} = 0$) is zero.

The spiking regimes of individual neurons are induced by direct stimulation currents I_j. In order to spread the natural spiking frequencies of neurons we choose these values randomly from a normal distribution with the mean $\langle I \rangle = 25\ \mu\text{A/cm}^2$ and standard deviation $\sigma = 0.5\,\mu\text{A/cm}^2$. The neurons are globally coupled via synaptic current I_{syn} defined by Eq. (3.44) with the parameters $(v_c, v_0, v_{\text{th}}) = (120, 50, 10)$ mV/cm^2. The charge-balanced act-and-wait control is performed via the current I_{con} determined by Eq. (3.50).

In Fig. 3.8 we show the results of numerical simulation of system (3.51) for $N = 100$ neurons. In the time interval $t \in [0, 1000]$ ms the dynamics of uncoupled ($g = 0$) and uncontrolled ($P = 0$) neurons is presented. Then in the interval $t \in [1000, 2500]$ ms the synaptic coupling (3.44) with the strength $g = 0.05$ mS/cm^2 is activated but the control is off. Finally, for $t \geq 2500$ ms we activate the charge-balanced act-and-wait control (3.50) with the strength $P = 0.23$ mS/cm^2 and delay time $\tau = 10.5$ ms. We see that the mean field V of uncoupled and uncontrolled neurons fluctuates with a small amplitude about some mean value [panel (a)] and the order parameter $|r|$ is small [panel (b)]. When the synaptic coupling is switched on, the neurons synchronize and the amplitude of the mean field as well as the order parameter increase. This synchronization is effectively suppressed when the control is switched on. The amplitude of the mean field suddenly decreases and we observe the fluctuations of the mean field similar to those observed without coupling and control. The order parameter also falls suddenly to small values. In panel (c), we show the dynamics of the control current.

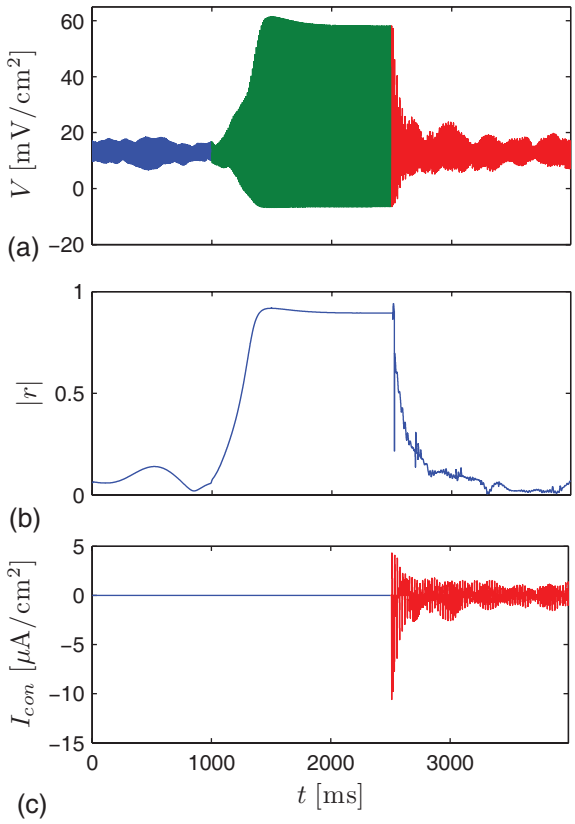

Figure 3.8: Dynamics of an ensemble of $N = 100$ Hodgkin-Huxley neurons (3.51). In the time interval $t \in [0, 1000]$ ms the control and coupling is off ($g = 0$, $P = 0$). In the interval $t \in [1000, 2500]$ ms the synaptic coupling (3.44) with the strength $g = 0.05$ mS/cm^2 is activated but the control is off. For $t \geq 2500$ ms the charge-balanced act-and-wait control (3.50) with the strength $P = 0.23$ mS/cm^2 and delay time $\tau = 10.5$ ms is activated. (a) The mean field of membrane potential, (b) absolute value of the order parameter, and (c) the control current.

When the system is desynchronized, the control current does not vanish. This is conditioned by the mean field fluctuations that remain in the desynchronized state due to the finite number of neurons. Here we do not show the dynamics of individual neurons, because it is analogous to that observed in the FHN model; the control does not destroy the spiking of individual neurons.

In Fig. 3.9, we present the results of numerical computation of the synchronization criterion (3.48) in the dependence of the act-and-wait control parameters τ and P. The values of the parameter S in the (τ, P) plane are depicted in color code. The incoherent state domains have again the resonance structure similar to that obtained for the FHN neurons [see Fig. 3.7 (b)]. Note that here as well as for the FHN neurons the charge-balanced act-and-wait control fails for $\tau \to 0$ (see Sec. 3.1 for details).

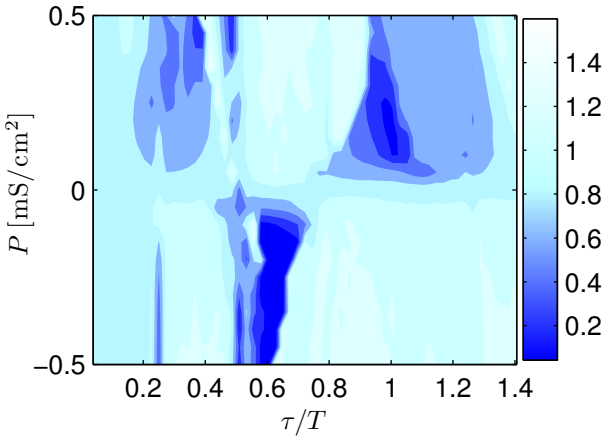

Figure 3.9: Performance of the charge-balanced act-and-wait control algorithm for synaptically coupled Hodgkin-Huxley neurons (3.51). The color in the (τ, P) parameter plane encodes the value of the synchronization criterion S defined by Eq. (3.48). Incoherent states are characterized by small values of S. The period of the mean field oscillations of the coupled control-free neurons is $T \approx 10.5$ ms. The values of the parameters are the same as in Fig. 3.8.

3.6 Summary

In this chapter, the act-and-wait control algorithm was proposed to suppress synchrony in globally coupled oscillatory networks in the situation when the simultaneous registration and stimulation of the system is not possible. The algorithm involves the periodic repetition of the registration (wait) and stimulation (act) stages, such that in the first stage the mean field of the free system is recorded in a memory and in the second stage the system is stimulated with the recorded signal. A modified version of the algorithm that takes into account the charge-balanced requirement is considered as well. The efficiency of our algorithm is demonstrated analytically and numerically for globally coupled Stuart-Landau oscillators, and synaptically all-to-all coupled FitzHugh-Nagumo as well as Hodgkin-Huxley neurons.

The results of this section are published in Ref. [109].

4. Eliminating synchronization in bistable networks

In this chapter, we consider the problem of controlling synchrony in bistable networks, which possess the coexisting coherent and incoherent states, both being stable for the same values of the parameters. The specific asymptotic state of such a system depends on the initial conditions. The control problem that we formulate here is as follows. We assume that a bistable network is initially in the stable coherent state and our aim is to design a particular time-dependent perturbation which enables us to switch the system to the stable incoherent state. Such a problem can be motivated, e.g., by a possible control of epilepsy, which is modelled by a bistable neural network in which the disease and healthy states are associated with the stable coherent and incoherent states, respectively.

Motivated by neural networks with excitatory and inhibitory coupling we have implemented in Ref. [110] introduced conformist-contrarian phase oscillators model. Along with this known Kuramoto-type model, we introduce the bistable networks consisting of all-to-all coupled noisy FitzHugh-Nagumo neurons.In the real brain most neurons are connected relatively sparsely and locally. There are a very small proportion of highly connected neurons (hubs), which have connections spanning much longer distances, whilst most neurons would only interact with a few neighbours. The mentioned properties are characteristic for networks with scale-free topology, which we implemented with phase oscillators model.

We suggest two different algorithms to switch the bistable networks from the stable coherent state to the stable incoherent state. One of them is an act-and-wait control method, which was presented in chapter 3. We show that this algorithm is efficient for the globally coupled populations. Another algorithm is based on the multisite coordinated reset stimulation (MCR). The algorithm is nonfeedback, but it uses inhomogeneous perturbations and is efficient even for the networks with a complex scale-free topology. In addition to the numerical analysis of finite size networks, the analytical results for the Kuramoto-type models in the

thermodynamic limit are presented.

The chapter is organized as follows. In Sec. 4.1, three models of bistable networks are presented and the existence of a hysteresis in synchronization diagrams is demonstrated. Sections 4.2 and 4.3 are devoted to the act-and-wait and MCR control algorithms, respectively. Using numerical and analytical methods we demonstrate their capability to eliminate synchronization in the above described networks. The conclusions are presented in Sec. 4.4.

4.1 Models of bistable oscillatory networks

4.1.1 Kuramoto model with positive and negative couplings

A generalized Kuramoto model that demonstrates synchronization bistability has been proposed in Ref. [110]:

$$\dot{\theta}_j = \omega_j + \frac{K_j}{N}\sum_{l=1}^{N}\sin(\theta_l - \theta_j), \quad j = 1, \ldots, N. \tag{4.1}$$

Here θ_j is the phase of the jth oscillator and ω_j is its natural frequency, chosen at random from a unimodal, symmetric probability density $g(\omega)$. There are two types of oscillators in the population referred to as conformists and contrarians. The conformists are positively connected ($K_j > 0$) to all other oscillators of the population and they tend to fall in line with whatever rhythm has emerged in the population. The contrarians have negative coupling strength $K_j < 0$ and they are repelled by the prevailing rhythm. In terms of neuroscience, the positive and negative values of the coefficients K_j correspond to the excitatory and inhibitory coupling, respectively.

For the Kuramoto-type models, the collective rhythm is quantified by the complex order parameter

$$R = \frac{1}{N}\sum_{l=1}^{N} e^{i\theta_l}. \tag{4.2}$$

The absolute value $0 \leq |R| \leq 1$ of this parameter measures the macroscopic coherence of the system. The value $|R| = 0$ indicates the incoherent state while $|R| = 1$ defines the fully synchronized state. The values in-between represent partially synchronized states. Note, that differently from the previous chapters, here the whole systems order parameter is identified by a capital letter R, while the order parameter of some groups of oscillators will be marked by lower case

letter r. By means of the definition (4.2), the system (4.1) can be rewritten as

$$\dot{\theta}_j = \omega_j + \mathrm{Im}\left[K_j R e^{-i\theta_j}\right], \quad j = 1, \ldots, N. \tag{4.3}$$

In our numerical simulations, we choose the natural frequencies of the oscillators from the Lorentz distribution

$$g(\omega) = (\Delta/\pi)\left[(\omega - \omega_0)^2 + \Delta^2\right]^{-1} \tag{4.4}$$

and then subdivide randomly the whole population of N oscillators into two groups with N_- and N_+ oscillators in each subpopulation. For all oscillators in the first subpopulation we assign the same negative value of the coupling strength $K_j = \kappa_1 < 0$ and label these oscillators as contrarians. Similarly, for the second, conformist subpopulation, we set $K_j = \kappa_2 > 0$. We also introduce the parameter $p = N_+/N$ that denotes the proportion of conformists in the population.

Continuation diagram. In Fig. 4.1, we present an example of a synchronization diagram that demonstrates the hysteresis in the dependence $|R|$ versus p and thus the existence of the bistability. The system (4.1) consisting of $N = 10000$ phase oscillators was numerically simulated for the fixed values of the parameters $\omega_0 = 0$, $\Delta = 0.05$, $\kappa_1 = -3$ and $\kappa_2 = 1$. The values of the parameter p were first increased progressively for $p_0, p_0 + \delta p, \ldots, p_0 + n\delta p$ (forward continuation) and then decreased from $p_0 + n\delta p$ to p_0 (backward continuation). For each fixed p, the stationary post-transient values of the order parameter $|R|$ were computed and depicted in Fig. 4.1. In this diagram, the lower branch indicates the incoherent state, when the oscillators are completely desynchronized and scattered uniformly across all phases. The upper branch represents the state in which the conformists and contrarians are partially synchronized into two diametrically opposed clusters whose phases are separated by the angle π. The forward and backward continuations lead to the sudden jumps of the order parameter from zero (incoherent state) to a finite value (coherent state) and back. The jumps take place at different values of the parameter p. The stable incoherent and coherent states coexist in the interval of p between the jumps of the order parameter.

The main advantage of this model is that it admits an analytical treatment in the thermodynamic limit of infinite number of oscillators $N \to \infty$. In the next sections, we will use this approach to facilitate the analysis of our proposed bistability control algorithms.

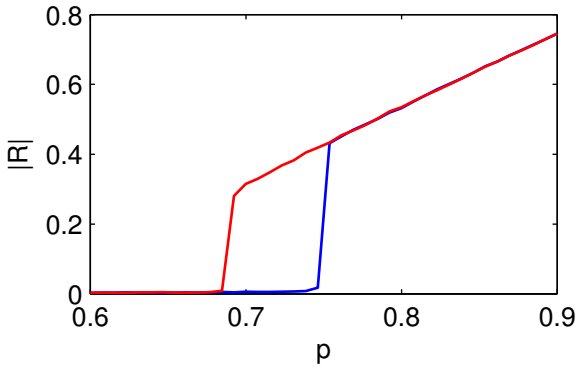

Figure 4.1: Synchronization diagram for the generalized Kuramoto model (4.1) consisting of $N = 10000$ coupled phase oscillators at the parameter values $\omega_0 = 0$, $\Delta = 0.05$, $\kappa_1 = -3$ and $\kappa_2 = 1$. Blue (dark) and red (light) curves show the forward and backward continuations, respectively. The continuation step is $\delta p = 0.0075$.

4.1.2 Synaptically coupled FitzHugh-Nagumo neurons

In this section, we present a bistable network constructed in a similar way as described above, but instead of the phase oscillators as units of the network we utilize FHN neurons. Moreover, we take into account the synaptic coupling between neurons and the presence of noise. Specifically, our model is as follows:

$$\dot{v}_j = f(v_j) - w_j + I - I_{\text{syn}} - I_{\text{con}} + \xi_j, \tag{4.5a}$$

$$\dot{w}_j = \varepsilon_j(b_0 + b_1 v - w_j) \tag{4.5b}$$

for $j = 1, \ldots, N$. Here the variable v_j denotes the membrane potential and w_j is the recovery variable of the jth neuron, $f(v_j) = v_j - v_j^3/3$ is the cubic source term of an ionic current and I is a constant current that defines the spiking regime of uncoupled neurons. The current I_{syn} defines the coupling between neurons and I_{con} is the control current, which will be defined in the next sections. Here we take $I_{\text{con}} = 0$. The last term in Eq. (4.5a) is the white Gaussian noise, which is different and independent for each neuron. We assume that the mean value of the noise is zero $\langle \xi_j \rangle = 0$ and the standard deviation is $\sigma_{\xi_j} = 0.1$. The parameter ε_j defines the ratio between the characteristic time scales of v_j and w_j variables and also the spiking period of the jth neuron. To scatter the spiking periods of the neurons we choose ε_j randomly from the Gaussian distribution with the mean $\langle \varepsilon \rangle = 0.02$ and the standard deviation $\sigma_\varepsilon = 0.1\langle \varepsilon \rangle$. The other parameters are chosen as follows $b_0 = 2$ and $b_1 = 1.5$.

To mimic realistic junctions between neurons, we couple them synaptically. We

assume for simplicity that the coupling is global and write the term of synaptic current in the form

$$I_{\text{syn}} = K_j(v_j - U_j)\frac{1}{N-1}\sum_{k\neq j}\Theta(v_k - v_0), \tag{4.6}$$

where K_j is the coupling strength and U_j defines the reversal potential of the jth neuron. $\Theta(v) = 1/[1 + \exp(-(v - v_{\text{th}})/\Delta)]$ is the sigmoid function with the threshold parameter $v_{\text{th}} = 1.5$ and the width $\Delta = 0.1$. In analogy to the previous model, we subdivide randomly the whole population of N neurons into two groups consisting of N_{exc} and N_{inh} neurons, characterized by the excitatory and inhibitory coupling, respectively. We distinguish them by the values of the parameters K_j and U_j. For excitatory coupled neurons, we choose $K_j = \kappa_1 = 0.4$ and $U_j = u_1 = 2.5$, while for inhibitory coupled neurons, we take $K_j = \kappa_2 = 1.2$ and $U_j = u_2 = -2.5$. We denote by $p = N_{\text{exc}}/N$ the proportion of excitatory coupled neurons.

As in the case of Sec. 3.4, the use of the order parameter (4.2) for the system (4.5) is problematic, since it is difficult to define the phases of individual neurons when their dynamics is complex. Therefore we use an alternative synchronization criterion based on the variance $\text{Var}(V)$ of the mean field:

$$V(t) = \frac{1}{N}\sum_{j=1}^{N} v_j(t). \tag{4.7}$$

In the synchronized state, when all neurons spike simultaneously, the value of this parameter is large, while in the incoherent state it is close to zero. In addition, we introduce the variances $\text{Var}(V_{\text{exc}})$ and $\text{Var}(V_{\text{inh}})$ for the mean fields of excitatory and inhibitory coupled neurons in order to separately measure the synchronization level in each of the subpopulations.

Figure 4.2 shows dependence of the variances $\text{Var}(V)$, $\text{Var}(V_{\text{inh}})$ and $\text{Var}(V_{\text{exc}})$ on the parameter p. The computations were performed for the total number of $N = 5000$ neurons with the continuation step $\delta p = 0.017$. The hysteresis in these dependencies indicates the presence of the bistability. In the interval of the parameter $p \in (0.45, 0.62)$ the phase space of the system has two attractors related to the coherent and incoherent states.

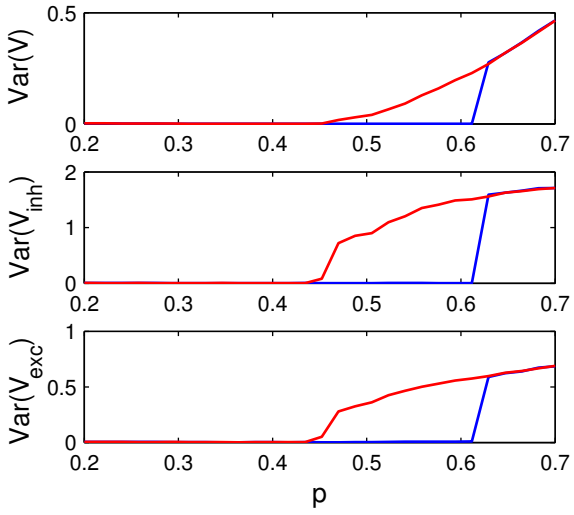

Figure 4.2: Synchronization diagrams for the network of $N = 5000$ synaptically coupled FHN neurons (4.5). Blue (dark) and red (light) curves show the forward and backward continuations, respectively. The continuation step is $\delta p = 0.0075$, the values of other parameters are presented in the text. Equations (4.5) were integrated by Euler-Maruyama method with time step $h = 0.05$.

4.1.3 Scale-free network of phase oscillators

The last bistable network analyzed in this thesis differs essentially from the previous three by the topology of connections. Now we consider a network of phase oscillators connected by a scale-free topology:

$$\dot{\theta}_j = \omega_j + K \sum_{l=1}^{N} a_{jl} \sin(\theta_l - \theta_j). \tag{4.8}$$

Here a_{jl} is an element of the adjacency matrix $\mathbf{A}$, which encodes network's topology. For the connected j and l oscillators, the matrix element is equal to one, $a_{jl} = 1$, while $a_{jl} = 0$ otherwise. We assume that the coupling is symmetric $a_{lj} = a_{jl}$ and there are no self-connections $a_{ll} = 0$. In the scale-free networks, the proportion $P(k)$ of nodes having k connections satisfies for large k the power law $P(k) \sim k^{-\gamma}$ with $2 < \gamma \leq 3$. It was shown [111] that in scale-free networks the hysteresis appears when the natural frequencies ω_j of oscillators are positively correlated with their degrees (numbers of connections k_j), i.e. when $\omega_j \sim k_j$.

The degree of synchronization among oscillators is quantified by the order parameter (4.2). We performed numerical simulations with networks consisting $N = 10^3 \div 10^4$ number of oscillators with various power law exponents γ and average degree $\langle k \rangle$. Our simulations show that the position and the width of hysteresis in continuation plot depends strongly on specific networks realisation.

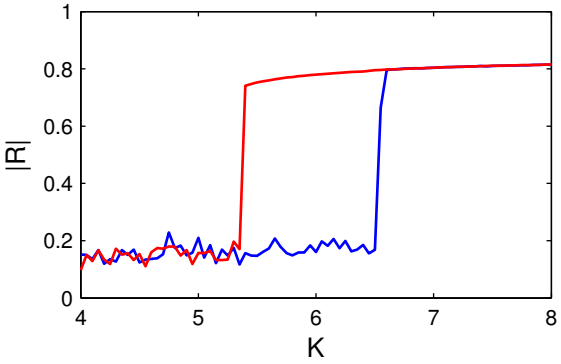

Figure 4.3: Synchronization diagram for the scale-free network of $N = 1000$ phase oscillators (4.8). The adjacency matrix is generated using the configuration model [113] with the parameters $\gamma = 2.4$, $\langle k \rangle = 6$ and $k_{\min} = 1$. The natural frequency for each oscillator is equal to its degree, $\omega_j = k_j$. Blue (dark) and red (light) curves show the forward and backward continuations, respectively. The continuation step is $\delta K = 0.05$.

This means that the different networks generated from the same sequence of oscillators degrees can have different continuation diagrams for the order parameter defined in (4.2). For demonstration purpose of our algorithms we have chosen one realisation (showed in Fig. 4.3) with sufficiently wide range of bistability. Here is a scale-free network consisting of $N = 1000$ oscillators. The adjacency matrix was generated according to the configuration model [113] with the scale factor $\gamma = 2.4$, average degree $\langle k \rangle = 6$ and minimal junction number $k_{\min} = 1$. The natural frequency of each oscillator was chosen equal to its degree, $\omega_j = k_j$. The observed hysteresis indicates the bistability of synchronization in the interval of the coupling strength $K \in (0.54, 0.65)$.

4.2 Eliminating synchronization via an act-and-wait algorithm

We verify the efficacy of the act-and-wait algorithm for eliminating synchronization in bistable networks described above (see Sec. 4.1). We present the results only for the first two models. The last model is omitted, since it turned out that this algorithm is inefficient for the scale-free networks. Nonetheless, in Sec. 4.3 we will show that the bistable scale-free networks can be effectively controlled by the MCR algorithm.

4.2.1 Kuramoto model with positive and negative couplings

In the presence of the act-and-wait control, the Kuramoto model Eqs. (4.3) transform to

$$\dot{\theta}_j = \omega_j + \mathrm{Im}\left[(K_j R - PG(t)R_\tau)\, e^{-i\theta_j}\right] \tag{4.9}$$

for $j = 1, \ldots, N$. Here the additional term $PG(t)R_\tau$ stands for the act-and-wait control force, where P is the feedback strength, $G(t)$ is the periodic function defined by Eq. (3.10) and the subscript τ in R_τ denotes the time-delayed value $R_\tau \equiv R(t-\tau)$. The form of the control term is derived from a model of coupled and stimulated Stuart-Landau oscillators in the assumption that only mean field is available for the measurement and the control perturbation is applied homogeneously.

The results of successful elimination of synchronization in system (4.9) consisting of $N_- = 1500$ contrarians and $N_+ = 3500$ conformists are presented in Fig. 4.4. The blue (dark) curve in panel (a) shows the dynamics of the order parameter (4.2). For $t < 100$, the control perturbation is off, P=0. The initial conditions are chosen such that the bistable system settles to the synchronized state. In this state, the order parameter fluctuates around the value $|R| = 0.31$. The contrarians and conformists crowd into two diametrically opposed clusters whose phases are separated by the angle π. This is evident from the dynamics of the phase distribution shown in panel (b). For $100 < t < 200$, the act-and-wait control algorithm with the strength $P = 2$ is activated. We see that the act-and-wait feedback perturbation destroys the coherent clustered state. However, the feedback perturbation is constructed in such a way that it does not destroy the incoherent state of the system, and moreover this state remains stable in the presence of control. The feedback seemingly makes the incoherent state the only attractor of the system and because of that it settles to this state after a short transient period. As a result the value of the order parameter falls to zero and the phase distribution becomes uniform. For $t > 200$, the control force is switched off, $P = 0$. Since the control-free system is bistable, it remains in its stable incoherent state in the absence of control.

The system (4.9) admits an analytical treatment and essential simplification in the thermodynamic limit of infinite number of oscillators, $N \to +\infty$. Using the Ott-Antonsen ansatz [106] with the assumption that the natural frequencies ω_j satisfy the Lorentz distribution (4.4), system (4.9) can be reduced to only two

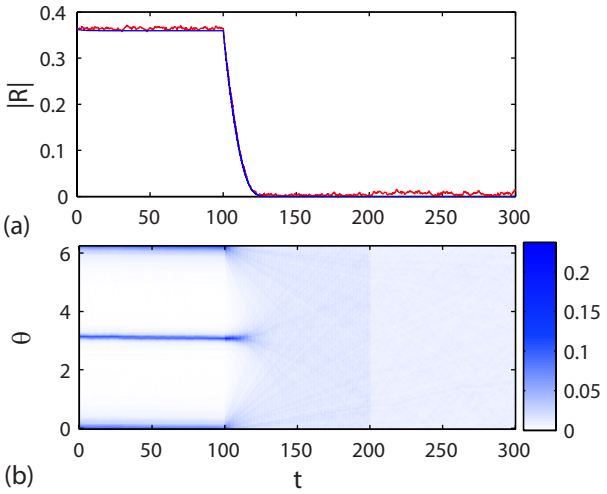

Figure 4.4: Eliminating the synchronization by act-and-wait control in the Kuramoto model (4.9) for $N = 5000$, $p = 0.7$, $\omega_0 = 0$, $\Delta = 0.05$, $\kappa_1 = -3$ and $\kappa_2 = 1$. For $t < 100$, the system is control-free ($P = 0$), in the interval $100 < t < 200$ the act-and-wait control is on with $P = 2$ and $\tau = 0.2$ and for $t > 200$, the system is again control-free. (a) Red (light) curve shows the absolute value of the order parameter computed from the system (4.9) while blue (dark) curve shows the same result obtained from the reduced system (4.10). (b) Dynamics of the phase distribution of Eqs. (4.9). The values of the phase density are encoded by colours.

differential equations (cf. [110] and Sec. 3.2):

$$\dot{r}_1 = \kappa_1(R^* - Rr_1^2)/2 - (i\omega_0 - \Delta)r_1 + F_1, \tag{4.10a}$$

$$\dot{r}_2 = \kappa_2(R^* - Rr_2^2)/2 - (i\omega_0 - \Delta)r_2 + F_2, \tag{4.10b}$$

where r_1 and r_2 are the complex order parameters of the contrarian and conformist subpopulations, respectively and

$$F_{1,2} = -PG(t)(R_\tau^* - R_\tau r_{1,2}^2)/2 \tag{4.11}$$

are the act-and-wait feedback forces. The total order parameter (4.2) is related to this parameters via a simple algebraic expression

$$R = (1-p)r_1^* + pr_2^*. \tag{4.12}$$

To verify the validity of the reduced system (4.10), we have computed the dynamics of the order parameter using Eqs. (4.10) with the same conditions as above. The result is depicted in Fig. 4.4 (a) by the red (light) curve. We see that this curve is close to the blue (dark) curve obtained by direct simulation of the original

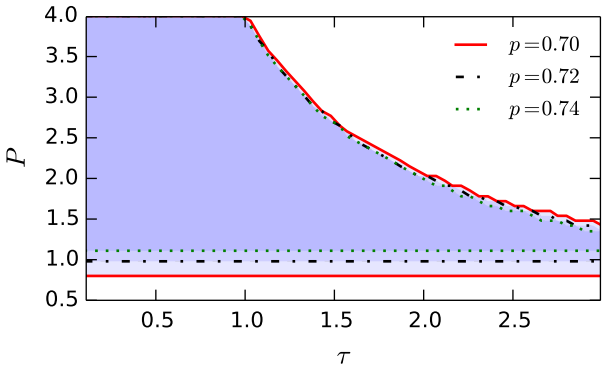

Figure 4.5: Domain of successful elimination of synchronization in the plane of parameters (P, τ) for the Kuramoto model with positive and negative couplings estimated from the reduced system (4.10). Different line styles represent regions of desynchronization for different conformists ratio p in the network. The other values of the parameters are the same as in Fig. 4.4.

system (4.9).

The reduced system (4.10) is computationally much more efficient than the original system (4.9) and can be used to investigate the performance of the act-and-wait algorithm in more details. In Fig. 4.5 we show how the control performance depends on the choice of the coupling strength P and the delay time τ for different values of the parameter p. For a given pair of the parameters (P, τ), we took the initial conditions at the synchronized state and applied for some period of time the act-and-wait control. Then we switched off the control and computed the mean absolute value of the order parameter in the post transient regime. The region of the parameters (P,τ) where system settles into the incoherent state is restricted by the coloured area between the same type of lines. We see that the increase of the delay τ narrows the range of the strength P where the act-and-wait control is effective. Also, the increase of the strength P narrows the range of τ where the elimination of synchronization is successful. The act-and-wait algorithm works for the various ratios p of conformists in the network. The variation of the parameter p changes only the bottom limit of feedback gain P in the domain of successful control, while the top limit remains almost the same.

4.2.2 Synaptically coupled FitzHugh-Nagumo neurons

The act-and-wait control algorithm works well for rather complicated systems. Here we show that it can eliminate synchronization in a noisy system of synaptically coupled FHN neurons introduced in Sec. 4.1.2. Assuming that only the mean field is available for the measurement and only homogeneous perturbations

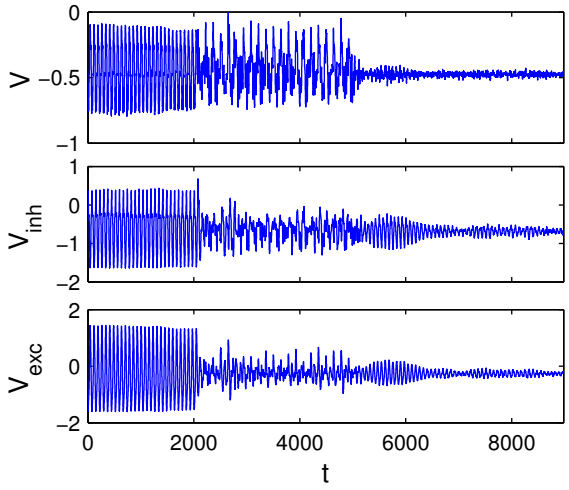

Figure 4.6: Eliminating the synchronization by act-and-wait control in the network of synaptically coupled FHN neurons (4.5) for $N = 5000$ and $p = 0.5$. V denotes the mean field of the whole population, while V_{inh} and V_{exc} are the mean fields of inhibitory and excitatory coupled subpopulations. For $t < 2000$, the system is control-free ($P = 0$), in the interval $2000 < t < 5000$, the act-and-wait control is on with $P = 0.2$ and $\tau = 71$ and for $t > 5000$, the system is again control-free

are allowed, the control current in the model (4.5) can be written as

$$I_{\text{con}}(t) = G(t)PV(t-\tau), \tag{4.13}$$

where $G(t)$ is the periodic function (3.10), P is the feedback strength and $V(t-\tau)$ is a time-delayed value of the mean field (4.7).

Figure 4.6 demonstrates the results of successful elimination of synchronization in the network (4.5) consisting of $N = 5000$ neurons, a half of which is coupled inhibitory and another half is coupled excitatory. We show the dynamics of the mean fields $V(t)$, $V_{\text{inh}}(t)$ and $V_{\text{exc}}(t)$. Without control ($t < 2000$), the network is in the synchronized state; here all mean fields exhibit almost periodic oscillations with large amplitude. In the time interval $2000 < t < 5000$, the act-and-wait control is activated with the strength $P = 0.2$ and the delay time $\tau = 71$, chosen close the period of oscillations of the mean field of control-free system. We see that the control decreases the amplitudes of variations of the mean fields. For $t > 5000$, the control is switched off and the system settles to the stable incoherent state. Note that the amplitudes of oscillations are higher during the control than after the control is turned off. This means that at the end of the control the system state does not reside exactly in the incoherent attractor, but it enters its basin of attraction.

4.3 Eliminating synchronization via a multisite coordinated reset stimulation

When controlling the bistable networks by MCR algorithm, we do not need to periodically switch on and off the stimulation. Below we show that synchronization can be eliminated by only single switched on and off cycle. Here we use a soft stimulation approach [65] where the stimulation frequency is close to the mean frequency of the network.

4.3.1 Kuramoto model with positive and negative couplings

First we verify the performance of the MCR stimulation algorithm for the Kuramoto model (4.3). In the presence of the MCR stimulation this model reads:

$$\dot{\theta}_j = \omega_j + \mathrm{Im}\left[\left(K_j R + a e^{i(\Omega t + \phi_j^{(m)})}\right) e^{-i\theta_j}\right] \tag{4.14}$$

for $j = 1, \ldots, N$. Here the amplitude a and the frequency Ω of the MCR stimulation are equal for all units of the network, while the phases $\phi_j^{(m)}$ are different. We assume that in the case of M electrodes, each of them stimulates independently N/M different units of the network. The phase shifts of periodic signals applied to the electrodes are chosen as $2\pi(m-1)/M$, where $m = 1, \ldots, M$ is the number of the electrode. In this way the whole population is split into M distinct clusters related to the different stimulation sites, respectively. For all oscillatory units with the index j belonging to the mth cluster, the stimulation phase is $\phi_j^{(m)} = 2\pi(m-1)/M$. In our numerical simulations, the units are randomly assigned to the different clusters.

We tested the MCR stimulation algorithm with $M = 4$ for the network (4.14) consisting of $N_- = 1500$ contrarians and $N_+ = 3500$ conformists. In Fig. 4.7, the panels (a) and (b) show the dynamics of the order parameter (4.2) and of the phase distribution, respectively. For $t < 200$, the control-free system is in the synchronized regime in which contrarians and conformists are crowded into two opposed clusters. For $200 < t < 300$, the MCR stimulation is switched on and the network resynchronizes according to the applied signals so that phases of the oscillators are spread into new four uniformly distributed clusters separated by the angle $\pi/2$ with equal proportion of the oscillators in each cluster. Note that the contrarian and conformist oscillators are now mixed in each of the clusters. The

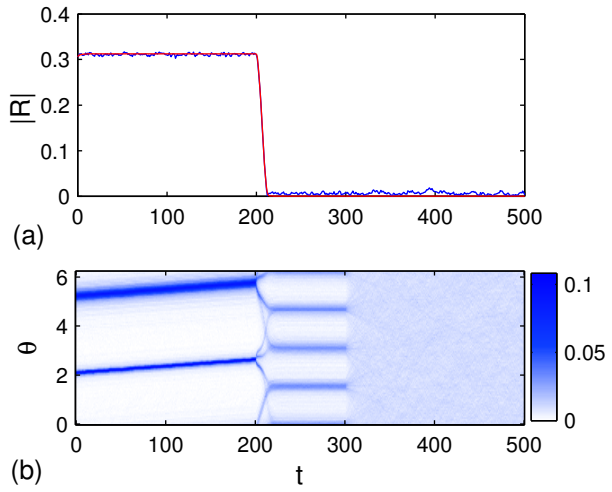

Figure 4.7: Eliminating the synchronization by MCR stimulation in the Kuramoto model (4.14) for $N = 5000$, $p = 0.7$, $\omega_0 = 0$, $\Delta = 0.05$, $\kappa_1 = -3$ and $\kappa_2 = 1$. For $t < 200$, the system is control-free ($a = 0$), in the interval $200 < t < 300$ the MCR stimulation is on with $M = 4$, $a = 0.3$ and $\Omega = 0$ and for $t > 300$, the system is again control-free. (a) Blue (dark) curve shows the absolute value of the order parameter computed from the system (4.14) while red (light) curve shows the same result obtained from the reduced system (4.15). (b) Dynamics of the phase distribution of Eqs. (4.14) .

state resulting from the MCR stimulation has more uniform phase distribution as compared to the initial synchronized state and thus it should be closer to the incoherent state in the phase space of the free system, since the latter is characterized by the uniform distribution of phases. This explains why the state resulting from the MCR stimulation appearers to lie in the basin of attraction of the incoherent attractor of the free system and why the system approaches this attractor when the stimulation is switched off ($t > 300$). We see that after a short transient period the phase distribution becomes totally uniform and the order parameter almost vanishes.

In the thermodynamic limit $N \to \infty$, the Kuramoto model (4.14) under MCR stimulation can be reduced by Ott–Antonsen ansatz [106] to only $2M$ differential equations:

$$\dot{r}_{1,m} = \frac{\kappa_1}{2}(R^* - Rr_{1,m}^2) - (i\omega_0 - \Delta)r_{1,m} + \bar{F}_1^{(m)}, \tag{4.15a}$$

$$\dot{r}_{2,m} = \frac{\kappa_2}{2}(R^* - Rr_{2,m}^2) - (i\omega_0 - \Delta)r_{2,m} + \bar{F}_2^{(m)} \tag{4.15b}$$

for $m = 1, \ldots, M$. Here $r_{1,m}$ and $r_{2,m}$ are the complex order parameters of the contrarian and conformist subpopulations, respectively, which are stimulated with

the periodic signal having phase shift $\phi^{(m)} = 2\pi(m-1)/M$. The stimulation force in system (4.15) reads:

$$\bar{F}_j^{(m)} = -\frac{a}{2}\left(e^{-i(\Omega t+\phi^{(m)})} r_{j,m}^2 - e^{i(\Omega t+\phi^{(m)})}\right) \tag{4.16}$$

for $j = 1, 2$ and $m = 1, \ldots, M$. The order parameter of the whole network can be computed as

$$R = \sum_{m=1}^{M} \{(1-p) r_{1,m}^* + p r_{2,m}^*\}. \tag{4.17}$$

In Fig. 4.7 (a), we compare the dynamics of the absolute value of the order parameter computed from the reduced system (4.15) (red/light curve) with that obtained by direct simulation of the original system (4.14) (blue/dark curve). The good coincidence of the above results means that the reduced system approximates well the dynamics of large networks of the Kuramoto oscillators in the presence of MCR stimulation.

4.3.2 Synaptically coupled FitzHugh-Nagumo neurons

The MCR stimulation current in the model (4.5) of synaptically coupled FHN neurons has the form

$$I_{\text{con}}(t) = a\cos(\Omega t + \phi_j^{(m)}), \tag{4.18}$$

where $\phi_j^{(m)} = 2\pi(m-1)/M$ is the phase of the stimulation signal coming from the mth electrode to the jth neuron. The results of successful elimination of synchronization in the network (4.5) consisting of $N = 5000$ neurons are presented in Fig. 4.8. The algorithm works well, although here we used only two ($M = 2$) stimulation electrodes.

4.3.3 Scale-free network of phase oscillators

The MCR stimulation approach goes beyond the model of globally coupled populations and admits some spatial structure of the network. Here we demonstrate its efficacy to eliminate synchronization in the scale-free network (4.8). To this end, we add to the Eqs. (4.8) the MCR stimulation term of the same form as for the Kuramoto model with positive and negative couplings (see Eqs. (4.14)):

$$\dot{\theta}_j = \omega_j + K\sum_{l=1}^{N} a_{jl}\sin(\theta_l - \theta_j) + a\sin(\Omega t + \phi_j^{(m)} - \theta_j) \tag{4.19}$$

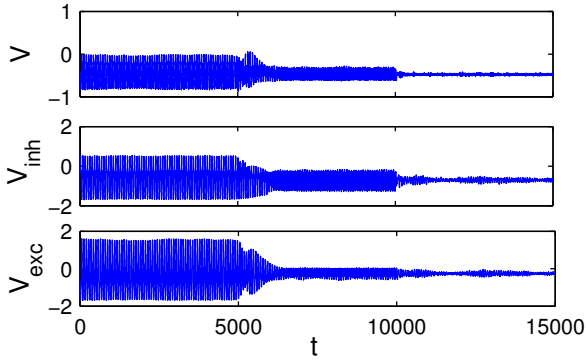

Figure 4.8: Eliminating the synchronization by MCR stimulation in the network of synaptically coupled FHN neurons (4.5). The parameters of the network are the same as in Fig. 4.6. For $t < 5000$, the system is control-free ($a = 0$), in the interval $5000 < t < 10000$ the MCR stimulation is on with $M = 2$, $a = 0.1$ and $\Omega = 2\pi/74$ and for $t > 10000$, the system is again control-free.

The results of numerical simulation of the network (4.19) are presented in Fig. 4.9. The coupling strength K is chosen equal to 6 and the other parameters of the network are the same as in Sec. 4.1.3. The panel (a) shows the dynamics of the order parameter, while the panel (b) displays an evolution of the phase distribution. For $t < 40$, the control-free network is in the synchronized state, then for $40 < t < 50$, the MCR stimulation with $M = 4$, $a = 10$ and $\Omega = 2\pi$ is switched on, and for $t > 50$ it is switched off. As a result the system settles to the stable incoherent state. The success of control can be again explained by the fact that the MCR stimulation produces the state with rather uniform phase distribution, which falls within the basin of attraction of the incoherent attractor of the free system.

4.4 Summary

In this chapter, the problem of controlling synchronization in bistable oscillatory networks has been considered. We have shown that the bistability effect is characteristic not only for the Kuramoto-type models, but also for a stochastic model of synaptically all-to-all coupled FitzHugh-Nagumo neurons with excitatory and inhibitory interaction. All these systems have coexisting stable coherent and incoherent states in a certain range of parameters. In order to switch a bistable network from the stable coherent state to the stable incoherent state, we have suggested and tested two different algorithms. Both of them take into account constraints typical for real-world neural networks; they satisfy the requirement that the control and measurements of the system are available only on a macroscopic level.

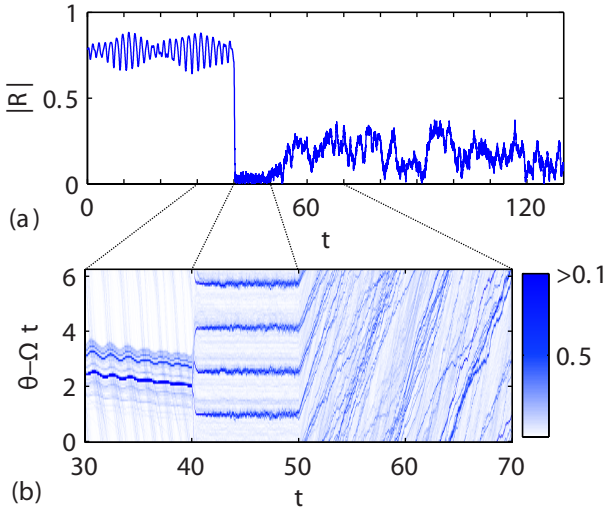

Figure 4.9: Eliminating the synchronization by MCR stimulation in the scale-free network (4.19) consisting of $N = 1000$ oscillators with coupling strength $K = 6$. Other parameters of the network are the same as in Fig. 4.3. For $t < 40$, the system is control-free ($a = 0$), in the interval $40 < t < 50$ the MCR stimulation is on with $M = 4$, $a = 10$ and $\Omega = 2\pi$, and for $t > 300$, the system is again control-free. (a) Dynamics of the absolute value of the order parameter. (b) Evolution of the phase distribution of Eqs. (4.19). Note different scales of time in panels (a) and (b).

The first, act-and-wait control algorithm, is constructed in such a way that it preserves the stable incoherent state of the system but destroys its coherent state. We have shown that this algorithm is efficient for networks with all-to-all coupling topology. The advantage of this algorithm is that it can be implemented in neural networks by a single electrode.

The second algorithm is based on multisite coordinated reset stimulation. This algorithm is a non-feedback and does not require online measurements of the system state. We have shown by examples that multicluster states, formed by the stimulation, lie in the basin of attraction of the incoherent attractor of the free system, so that after switching off the stimulation the network approaches the incoherent state. The main advantage of this approach is that it works well not only for networks with all-to-all coupling topology but is applicable for more complex networks as well. We have demonstrated its capability to eliminate synchronization in a bistable network with a nontrivial scale-free topology.

The results of this section are published in Ref. [114].

Main results and conclusions

1. The averaging method is adopted for a neurons under high-frequency stimulation (HFS). It is shown that the effect of the HFS on the neuron is determined by a stimulation parameter equal to the ratio of the amplitude to the frequency of the stimulation current.

2. A homogeneous HFS is an effective tool to control pulse propagation in the axon because the stimulation parameter regulates the pulse width and speed. It was established that high stimulation intensities can suppress pulse propagation. In myelinated axon, pulse enhancement is possible at a small stimulation intensity. The mechanism of this effect is related to the fact that threshold of neuron excitability parameter depends on the stimulation intensity.

3. An act-and-wait feedback algorithm was proposed for a synchronization control, where standard feedback algorithms can not be applied. Its efficacy and robustness were demonstrated analytically and numerically on various networks of oscillators.

4. The incoherent state stability domains of the act-and-wait algorithm in the parameter plane of the feedback delay time τ and gain P, have a resonance structure; they are located at the values of $\tau = mT/2$, where T is the characteristic period of oscillations of the mean field of synchronized oscillators in the absence of control and m is a non-negative integer number.

5. The act-and-wait algorithm satisfying the charge balance requirement was introduced. The charge balance requirement does not destroy the resonance structure of the incoherent state stability domains in the (τ, P) plane, but the algorithm stops to work for small values of τ.

6. The act-and-wait as well as the multisite coordinated reset stimulation (MCR) methods were suggested for switching bistable networks from the

stable coherent state to the stable incoherent state. The act-and-wait algorithm is efficient for the globally coupled populations of oscillators, while MCR is effective for global coupling and complex scale-free topology networks.

Bibliography

[1] A. C. Scott. *Neuroscience: A meathematical primer*. Springer, (2002).

[2] Th. Heimburg. The physics of nerves: Physical concepts help describing the propagation of nerve pulses. *Physik Journal*, **8**(3), 33–39, (2009).

[3] A. L. Hodgkin and A. F. Huxley. A quantitative description of membrane current and its application to conduction and excitation in nerve. *J. Physiol.*, **117**(4), 500–544, (1952).

[4] J. P. Keener and J. Sneyd. *Mathematical physiology*. Springer, New York, (1998).

[5] E. M. Izhikevich and R. FitzHugh. FitzHugh-Nagumo model. *Scholarpedia*, **1**(9), 1349, (2006).

[6] R. A. FitzHugh. Impulses and physiological states in theoretical models of nerve membrane. *Biophys. J.*, **1**, 445–466, (1961).

[7] J Nagumo, S. Arimoto, and S. Yoshizawa. An active pulse transmission line simulating nerve axon. *Proc IRE*, **50**, 2061–2070, (1962).

[8] D. A. Drachman. Do we have brain to spare? *Neurology*, **64**, 2004–2005, (2005).

[9] O.V. Popovych and P. A. Tass. Control of abnormal synchronization in neurological disorders. *Front. Neurol.*, **5**, 268, (2014).

[10] G. B. Ermentrout and D. H. Terman. *Mathematical Foundations of Neuroscience*. Springer-Verlag New York, (2010).

[11] Hollis Cline. Synaptogenesis: A balancing act between excitation and inhibition. *Current Biology*, **15**(6), R203 – R205, (2005).

[12] A. Balanov, N. Janson, D. Postnov, and O. Sosnovtseva. *Synchronization: from simple to complex*. Springer, (2009).

[13] A. Pikovsky, M. Rosenblum, and J. Kurths. *Synchronization. A universal concept in nonlinear sciences*. Cambridge university press, (2001).

[14] Y. Kuramoto. *Chemical oscillations, waves and turbulence*. Springer, Berlin, (1984).

[15] E. M. Izhikevich. *Dynamical systems in neuroscience. The geometry of excitability and bursting*. The MIT press, (2007).

[16] S. H. Strogatz. From Kuramoto to Crawford: exploring the onset of synchronization in populations of the coupled oscillators. *Physica D*, **143**, 1–20, (2000).

[17] E.M. Izhikevich. Which model to use for cortical spiking neurons? *Neural Networks, IEEE Transactions on*, **15**(5), 1063–1070, Sept 2004.

[18] F. Dörfler and F. Bullo. Synchronization in complex networks of phase oscillators: A survey. *Automatica*, **50**(6), 1539–1564, (2014).

[19] H. Daido. Order function and macroscopic mutual entrainment in uniformly coupled limit-cycle oscillators. *Progr. Theoret. Phys.*, **88**, 1213–1218, (1992).

[20] P. S. Skardal, E. Ott, and J. G. Restrepo. Cluster synchrony in systems of coupled phase oscillators with higher-order coupling. *Phys. Rev. E*, **84**, 036208, (2011).

[21] A. Schnitzler and J. Gross. Normal and pathological oscillatory communication in the barain. *Nat. Rev. Neurosci.*, **6**, 285–296, (2005).

[22] W. W. Alberts, E. W. Wright, and B. Feinstein. Cortical potentials and Parkinsonian tremor. *Nature*, **221**, 670–672, (1969).

[23] M. Magnin, A. Morel, and D. Jeanmond. Single-unit analysis of the palladum, thalamus and subthalamic nucleus in Parkinson patients. *Neuroscience*, **96**, 549–564, (2000).

[24] P. Brown, A. Olivero, P. Mazzone, A. Insola, P. Tonali, and V. Di Lazaro. Dopamine dependency of oscillations between subthalamic nucleus and pallidum in Parkinson's disease. *J. Neurosci.*, **21**, 1033–1038, (2001).

[25] P. Tass, M. G. Rosenblum, J. Weule, J. Kurths, A. Pikovsky, J. Volkmann, A. Schnitzler, and H.-J. Freund. Detection of $n : m$ phase locking from

noisy data: Application to magnetoencephalography. *Phys. Rev. Lett.*, **81**, 3291–3294, (1998).

[26] A. Nini, A. Feingold, H. Slovin, and H. Bergman. Neurons in the globus pallidus do not show correlated activity in the normal monkey, but phase-locked oscillations appear in the MPTP model of Parkinsonism. *J. Neurophysiol.*, **74**, 1800–1805, (1995).

[27] S. J. Schiff. Towards model-based control of Parkinson's disease. *Phil. Trans. R. Soc. A*, **368**, 2269–2308, (2010).

[28] A. Latteri, P. Arena, and P. Mazzone. Characterizing deep brain stimulation effects in computationally efficient neural network models. *Nonlinear Biomed. Phys.*, **5**, 2, (2011).

[29] R. Pahwa and K. E. Lyons, editors. *Handbook of Parkinson's disease*. Informa healthcare. New York, London, 4th edition, (2007).

[30] J. L. Vitek, R. A. E. Bakay, A. Freeman, M. Evatt, J. Green, W. McDonald, M. Haber, H. Barnhart, N. Wahlay, S. Triche, K. Mewes, V. Chockkan, J.-Y. Zhang, and M. R. DeLong. Randomized trial of pallidotomy versus medical therapy for Parkinson's disease. *Ann. Neurol.*, **53**, 558–569, (2003).

[31] A. L. Benabid, P. Pollak, A. Louveau, S. Henry, and J. de Rougemont. Combined (thalamotomy and stimulation) stereotactic surgery of the VIM thalamic nucleus for bilateral parkinson disease. *Appl. Neurophysiol.*, **50**, 344–346, (1987).

[32] A. L. Benabid, P. Pollak, C. Gervason, D. Hoffmann, D. M. Gao, M. Hommel, J.E. Perret, and J. de Rougemont. Long-term suppression of tremor by chronic stimulation of the ventral intermediate thalamic nucleus. *Lancet*, **337**, 403–406, (1991).

[33] M. S. Titcombe, L. Glass, D. Guehl, and A. Beuter. Dynamics of Parkinsonian tremor during deep brain stimulation. *Chaos*, **11**, 766–773, (2001).

[34] E. B. Montgomery Jr. *Deep brain stimulation programming. Principles and practice*. Oxford university press, (2010).

[35] J. Modolo, J. Henry, and A. Beuter. Dynamics of the subthalamo-pallidal complex in Parkinson's disease during deep brain stimulation. *J. Biol. Phys.*, **34**(3-4), 251–266, (2008).

[36] D. Terman, J. E. Rubin, A. C. Yew, and C. J. Wilson. Activity patterns in a model for the subthalamopallidal networks of the basal ganglia. *J. Neursoci.*, **22**, 2963–2976, (2002).

[37] D. Tarsy, J.L Vitek, A. S. Philip, and M.S. Okun, editors. *Deep brain stimulation in neurological and psychiatric diseases*. Humana Press, (2008).

[38] W. Meissner, A. Leblois, D. Hansel, B. Bioulac, Ch. E. Gross, A. Benazzouz, and Th. Boraud. Subthalamic high frequency stimulation resets subthalamic firing and reduces abnormal oscillations. *Brain*, **128**(10), 2372–2382, (2005).

[39] J. O. Dostrovsky, R. Levy, J. P. Wu, W. D. Hutchison, R. R. Tasker, and A. M. Lozano. Microstimulation-induced inhibition of neuronal firing in human globus pallidus. *Journal of Neurophysiology*, **84**(1), 570–574, (2000).

[40] Y.R. Wu, R. Levy, P. Ashby, R.R. Tasker, and J.O. Dostrovsky. Does stimulation of the gpi control dyskinesia by activating inhibitory axons? *Movement Disorders*, **16**(2), 208–216, (2001).

[41] Mohammed Filali, WilliamD. Hutchison, VanessaN. Palter, AndresM. Lozano, and JonathanO. Dostrovsky. Stimulation-induced inhibition of neuronal firing in human subthalamic nucleus. *Experimental Brain Research*, **156**(3), 274–281, (2004).

[42] K. Pyragas, V. Novičenko, and P. A. Tass. Mechanism of suppression of sustained neuronal spiking under high-frequency stimulation. *Biol. Cybern.*, **107**, 669–684, (2013).

[43] G. C. McConnell, R. Q. So, J. D. Hilliard, P. Lopomo, and W. M. Grill. Effective deep brain stimulation suppresses low-frequency network oscillations in the basal ganglia by regularizing neural firing patterns. *J. Neurosci.*, **32**, 15657–15668, (2012).

[44] J. Rubin and D. Terman. High frequency stimulation of the subthalamic nucleus eliminates pathological thalamic rhythmicity in a computational model. *J. Comput. Neurosci*, **16**, 211–235, (2004).

[45] W. M. Grill, A. N. Snyder, and S. Miocinovic. Deep brain stimulation creates an informational lesion of the stimulated nucleus. *Neuroreport*, **132**(1), 91–9, (2004).

[46] A. Benazzouz, D.M. Gao, Z.G. Ni, B. Piallat, and R. Bouali-Benazzouz. Effect of high-frequency stimulation of the subthalamic nucleus on the neuronal activities of the substantia nigra pars reticulata and ventrolateral nucleus of the thalamus in the rat. *Neuroscience*, **99**(2), 289 – 295, (2000).

[47] F. Windels, N. Bruet, A. Poupard, C. Feuerstein, A. Bertrand, and M. Savasta. Influence of the frequency parameter on extracellular glutamate and γ-aminobutyric acid in substantia nigra and globus pallidus during electrical stimulation of subthalamic nucleus in rats. *J. Neurosci. Research*, **72**(2), 259–267, (2003).

[48] W. Meissner, D. Harnack, R. Reese, G. Paul, T. Reum, M. Ansorge, H. Kusserow, Ch. Winter, R. Morgenstern, and A. Kupsch. High-frequency stimulation of the subthalamic nucleus enhances striatal dopamine release and metabolism in rats. *J. Neurochem.*, **85**(3), 601–609, (2003).

[49] N. Maurice, A.M. Thierry, J. Glowinski, and J.M. Deniau. Spontaneous and evoked activity of substantia nigra pars reticulata neurons during high-frequency stimulation of the subthalamic nucleus. *J. Neurosci.*, **23**(30), 9929–36, (2003).

[50] S. Galati, P. Mazzone, E. Fedele, A. Pisani, A. Peppe, M. Pierantozzi, L. Brusa, D. Tropepi, V. Moschella, M. Raiteri, P. Stanzione, G. Bernardi, and A. Stefani. Biochemical and electrophysiological changes of substantia nigra pars reticulata driven by subthalamic stimulation in patients with parkinson's disease. *Eur. J. Neurosci.*, **23**(11), 2923–2928, (2006).

[51] L. Bekar, W. Libionka, G. Tian, Q. Xu, A. Torres, X. Wang, D. Lovatt, E. Williams, T. Takano, J. Schnermann, R. Bakos, and M. Nedergaard. Adenosine is crucial for deep brain stimulation-mediated attenuation of tremor. *Nat. Med.*, **14**(1), 75–80, (2008).

[52] L. A. Freberg. *Discovering biological psychology.* Wadsworth Cengage Learning, 2 edition, (2009).

[53] M. Pirini, L. Rocchi, M. Sensi, and L. Chiari. A computational modelling approach to investigate different targets in deep brain stimulation for Parkinson's disease. *J. Comput. Neurosci.*, **26**, 91–107, (2009).

[54] J. Herzog, U. Fietzek, W. Hamel, A. Morsnowski, F. Steigerwald, B. Schrader, D. Weinert, G. Pfister, D. Müller, H.M. Mehdorn, G. Deuschl,

and J. Volkmann. Most effective stimulation site in subthalamic deep brain stimulation for parkinson's disease. *Mov. Disord.*, **19**(9), 1050–1054, (2004).

[55] T. Yokoyama, N. Ando, K. Sugiyama, S. Akamine, and H. Namba. Relationship of stimulation site location within the subthalamic nucleus region to clinical effects on parkinsonian symptoms. *Stereotact. Funct. Neurosurg.*, **84**, 170–175, (2006).

[56] J.A. Saint-Cyr, T. Hoque, L.C.M. Pereira, J.O. Dostrovsky, W.D. Hutchison, D.J. Mikulis, A. Abosch, E. Sime, A.E. Lang, and A.M. Lozano. Localization of clinically effective stimulating electrodes in the human subthalamic nucleus on magnetic resonance imaging. *Journal of Neurosurgery*, **97**(5), 1152–1166, (2002). PMID: 12450038.

[57] A.L. Benabid, B. Wallace, J. Mitrofanis, R. Xia, B. Piallat, S. Chabardes, and F. Berger. A putative generalized model of the effects and mechanism of action of high frequency electrical stimulation of the central nervous system. *Acta Neurol. Belg.*, **105**, 149–157, (2005).

[58] X. J. Feng, E. Shea-Brown, B. Greenwald, R. Kosut, and H. Rabitz. Optimal deep brain stimulation of the subthalamic nucleus – a computaional study. *J. Comput. Neurosci.*, **23**, 265–282, (2007).

[59] X. J. Feng, B. Greenwald, H. Rabitz, E. Shea-Brown, and R. Kosut. Toward closed-loop optimization of deep brain stimulation for Parkinson's disease: concepts and lessons from a computaional model. *J. Neural. Eng.*, **4**, L14–L21, (2007).

[60] P. Danzl, J. Hespanha, and J. Moehlis. Event-based minimum-time control of oscillatory neuron models. *Biol. Cybern.*, **101**, 387–399, (2009).

[61] P. A. Tass. Desynchronizing double-pulse phase resetting and application to deep brain stimulation. *Biol. Cybern.*, **85**, 434–354, (2001).

[62] P. A. Tass. Effective desynchronization by means of double-pulse phase resetting. *Europhys. Lett.*, **53**, 15–21, (2001).

[63] P. A. Tass. Effective desynchronization with bipolar double pulse stimulation. *Phys. Rev. E*, **66**, 036226, (2002).

[64] P. A. Tass. Effective desynchronization with a resetting pulse-train followed by a single pulse. *Europhys. Lett.*, **55**, 171–177, (2001).

[65] P. A. Tass. Desynchronization of brain rhythms with soft phase-resetting techniques. *Biol. Cybern.*, **87**, 102–115, (2002).

[66] P. A. Tass. Effective desynchronization with a stimulation technique based on soft phase resetting. *Europhys. Lett.*, **57**, 164–170, (2002).

[67] P. A. Tass. A model of desynchronizing deep brain stimulation with a demand-controlled coordinated reset of neural subpopulations. *Biol. Cybern.*, **89**, 81–88, (2003).

[68] P. A. Tass. Desynchronization by means of a coordinated reset of neural sub-populations. *Progr. Theoret. Phys. Suppl.*, **150**, 281–296, (2003).

[69] C. Hauptmann and P. A. Tass. Therapeutic rewiring by means of desynchronizing brain stimulation. *Biosystems*, **89**, 173–181, (2007).

[70] P. A. Tass, L. Qin, Ch. Hauptmann, S. Dovero, E. Bezard, Th. Boraud, and W. G. Meissner. Coordinated reset has sustained aftereffects in Parkinsonian monkeys. *Ann. of Neurol.*, **72**(5), 816–820, (2012).

[71] M. G. Rosenblum and A. S. Pikovsky. Controlling synchronization in an ensemble of globally coupled oscillators. *Phys. Rev. Lett.*, **92**, 114102, (2004).

[72] M. G. Rosenblum and A. S. Pikovsky. Delayed feedback control of collective synchrony: An approach to suppression of pathological brain rhythms. *Phys. Rev. E*, **70**, 041904, (2004).

[73] M. Rosenblum, N. Tukhlina, and A. Pikovsky. Delayed feedback suppression of collective rhythmic activity in a neuronal ensemble. *Int. J. Bifurcation Chaos*, **7**, 1989–1999, (2006).

[74] C. Hauptmann, O. Popovych, and P. A. Tass. Delayed feedback control of synchronization in locally coupled neuronal networks. *Neurocomputing*, **65-66**, 759–767, (2005).

[75] C. Hauptmann, O. Popovych, and P. A. Tass. Effectively desynchronizing deep brain stimulation based on a coordinated delayed feedback stimulation via several sites: a computational study. *Biol. Cybern.*, **93**, 463–470, (2005).

[76] O. E. Omel'chenko, C. Hauptmann, Yu L. Maistrenko, and P. A. Tass. Collective dynamics of globally coupled phase oscillators under multisite delayed feedback stimulation. *Physica D*, **237**, 365–384, (2008).

[77] C. A. S. Batista, S. R. Lopes, R. L. Viana, and A. M. Batista. Delayed feedback control of bursting synchronization in a scale-free neuronal network. *Neural Networks*, **23**, 114–124, (2010).

[78] O. V. Popovych, C. Hauptmann, and P. A. Tass. Effective desynchronization by nonlinear delayed feedback. *Phys. Rev. Lett.*, **94**, 164102, (2005).

[79] O. V. Popovych, Ch. Hauptmann, and P. A. Tass. Control of neuronal synchrony by nonlinear delayed feedback. *Biol. Cybern.*, **95**, 69–85, (2006).

[80] O. V. Popovych and P. A. Tass. Synchronization control of interacting oscillatory ensembles by mixed nonlinear delayed feedback. *Phys. Rev. E*, **82**, 026204, (2010).

[81] N. Tukhlina, M. Rosenblum, A. Pikovsky, and J. Kurths. Feedback suppression of neural synchrony by vanishing stimulation. *Phys. Rev. E*, **75**, 011918, (2007).

[82] L. Ming, W. Yongjun, and J. Peng. Washout filter aided mean field feedback desynchronization in an ensemble of globally coupled neural oscillators. *Biol. Cybern.*, **101**, 214–246, (2009).

[83] G. Montaseri, M. J. Yazdanpanah, A. Pikovsky, and M. Rosenblum. Synchrony suppression in ensembles of coupled oscillators via adaptive vanishing feedback. *Chaos*, **23**, 033122, (2013).

[84] B. Rosin, M. Slovik, R. Mitelman, M. Rivlin-Etzion, S. N. Haber, L. Israe, E. Vaadia, and H. Bergman. Closed-loop deep brain stimulation is superior in ameliorating parkinsonism. *Neuron*, **72**, 370–384, (2011).

[85] A. Berényi, M. Belluscio, D. Mao, and G. Buzsáki. Closed-loop control of epilepsy by transcranial electrical stimulation. *Science*, **337**, 735–737, (2012).

[86] V. H. P. Louzada, N. A. M. Araújo, J. S. Andrade Jr., and H. J. Herrmann. How to suppress undesired synchronization. *Sci. Rep.*, **2**, 658, (2012).

[87] K. Pyragas, O.V. Popovich, and P.A. Tass. Controlling synchrony in oscillatory networks with separate stimulation – registration setup. *Europhys. Lett.*, **80**, 40002, (2007).

[88] J. A. Sanders, F. Verhulst, and J. Murdock. *Averaging Methods in Nonlinear Dynamical Systems*. Springer, (2007).

[89] A. C. Scott. The electrophysics of a nerve fiber. *Rev. Mod. Phys.*, **47**, 487–533, (1975).

[90] J. P. Keener. Waves in excitable media. *SIAM J. Appl. Math.*, **39**, 528–548, (1980).

[91] G. Flores. Stability analysis for the slow traveling pulse of the FitzHugh-Nagumo system. *SIAM J. Math. Anal.*, **22**, 392–399, (1991).

[92] C. K. R. T. Jones. Stability of the travelling wave solution of the Fitzhugh-Nagumo system. *Trans. Amer. Math. Soc.*, **286**, 431–469, (1984).

[93] A. Dhooge, W. Govaerts, and Yu. A. Kuznetsov. MATCONT: A MATLAB package for numerical bifurcation analysis of ODEs. *ACM TOMS*, **29**, 141–164, (2003).

[94] R. M. Miura. Accurate computation of the stable solitary wave for the Fitzhugh-Nagumo equations. *J. Math. Biology*, **13**, 247–269, (1982).

[95] A. Carpio and L. L. Bonilla. Pulse propagation in discrete systems of coupled excitable cells. *SIAM Journal on Applied Mathematics*, **63**(2), 619–635, (2002).

[96] Th. Erneux and G. Nicolis. Propagating waves in discrete bistable reaction-diffusion systems. *Physica D*, **67**, 237–244, (1993).

[97] J. P. Keener. Propagation and its failure in coupled systems of discrete excitable cells. *SIAM J. Appl. Math.*, **47**(3), 556–572, (1987).

[98] J. Keener and J. Sneyd. *Mathematical physiology*. Springer, (2001).

[99] D. Barkley, M. Kness, and L. S. Tuckerman. Spiral-wave dynamics in a simple model of excitable media: The transition from simple to compound rotation. *Phys. Rev. A*, **42**, 2489–2492, (1990).

[100] E. Ullner, A. Zaikin, J. Garcia-Ojalvo, R. Báscones, and J. Kurths. Vibrational resonance and vibrational propagation in excitable systems. *Phys. Lett. A*, **312**, 348–354, (2003).

[101] I. Ratas and K. Pyragas. Effect of high-frequency stimulation on nerve pulse propagation in the FithzHugh-Nagumo model. *Nonlinear Dyn.*, **67**, 2899–2908, (2012).

[102] I. Ratas and K. Pyragas. Pulse propagation and failure in the discrete FitzHugh-Nagumo model subject to high-frequency stimulation. *Phys. Rev. E*, **86**, 046211, (2012).

[103] C. Beurrier, L. Garcia, B. Bioulac, and C. Hammond. Subthalamic nucleus: A clock inside basal ganglia? *Thalamus Relat. Syst.*, **2**, 1–8, (2002).

[104] T. Insperger. Act-and-wait concept for continuous-time control systems with feedback delay. *IEEE Trans. Control Syst. Technol.*, **14**, 974 – 977, (2006).

[105] G. Stépán and T. Insperger. Stability of time-periodic and delayed systems — a route to act-and-wait control. *Annu. Rev. Control*, **30**, 159–168, (2006).

[106] E. Ott and Th. M. Antonsen. Low dimensional behavior of large systems of globally coupled oscillators. *Chaos*, **18**, 037113, (2008).

[107] D. Harnack, Ch. Winter, W Meissner, T. Reum, A. Kupsch, and R. Morgenstern. The effects of electrode material, charge density and stimulation duration on the safety of high-frequency stimulation of the subthalamic nucleus in rats. *J. Neurosci. Meth.*, **138**, 207–216, (2004).

[108] B. Piallat, S. Chabardès, A. Devergnas, N. Torres, M. Allain, E. Barrat, and A. L. Benabid. Monophasic but not biphasic pulses induce brain tissue damage during monopolar high-frequency deep brain stimulation. *Neurosurgery*, **64**, 156–163, (2009).

[109] I. Ratas and K. Pyragas. Controlling synchrony in oscillatory networks via an act-and-wait algorithm. *Phys. Rev. E*, **90**, 032914, (2014).

[110] H. Hong and S. H. Stogatz. Kuramoto model of coupled oscillators with positive and negative coupling parameters: An example of conformist and contrarian oscillators. *Phys. Rev. Lett.*, **106**, 054102, (2011).

[111] J. Gómez-Gardeñes, S. Gómez, A. Arenas, and Y. Moreno. Explosive synchronization transitions in scale-free networks. *Phys. Rev. Lett.*, **106**, 128701, (2011).

[112] Th.K. Peron and Rodrigues F.A. Determination of the critical coupling of explosive synchronization transitions in scale-free networks by mean-field approximations. *Phys. Rev. E*, **86**(5), 056108, (2012).

[113] M. Newman. *Networks: An introduction*. Oxford university press, (2010).

[114] Irmantas Ratas and Kestutis Pyragas. Eliminating synchronization in bistable networks. *Nonlinear Dynamics*, **DOI:10.1007/s11071-015-2393-6**, 1–15, (2015).

Abbreviations

CR – coordinated reset stimulation
DBS – deep brain stimulation
FHN – FitzHugh-Nagumo (a simplified neuron model)
GPe – globus pallidus externa (a functional part of the brain)
GPi – globus pallidus pars interna (a functional part of the brain)
HF(S) – high frequency (stimulation)
HH – Hodgkin-Huxley neuron model
MCR – multisite coordinated reset stimulation
ODE – ordinary differential equation(s)
PD – Parkinson's disease
SL – Stuart-Landau model
STN – subthalamic nucleus (a functional part of the brain)

Index

T

Santrauka

Disertacijoje nagrinėjama sužadinamų ir virpesinių neuroninių sistemų dinamika ir valdymas. Aptariami tiek patys paprasčiausi, tiek sudėtingesni neuronų ir jų tinklų modeliai. Nors disertacijoje naudojami supaprastinti realių neuronų matematiniai modeliai, tikimasi, kad šis darbas neuromoksle padės plėtoti naujus valdymo metodus.

Disertaciją sudaro keturi skyriai, iš jų trijuose pateikiami orginalūs rezultatai. Pirmame skyriuje pristatoma darbo problematika, disertacijoje naudojamos sąvokos, modeliai, atliekama literatūros apžvalga. Antrame disertacijos skyriuje nagrinėjamas aukšto dažnio poveikis impulso sklidimui aksonu. Tiriami mielinuoto ir nemielinuoto aksono atvejai. Aksonas modeliuojamas naudojant FitzHugh-Nagumo modelį. Siekdami analitinių rezultatų pirmiausia sistemoms pritaikome vidurkinimo teoremą, taip atskirdami lėtąją ir greitąją neurono dinamikas. Tokiu būdu išvedame suvidurkintas lygtis, lėtajai neurono dinamikos daliai. Toliau taikome asimptotinį impulso konstravimo metodą. Ribiniu, mažo parametro atveju, nustatome impulso parametrų priklausomybę nuo aukštadažnės stimuliacijos intensyvumo. Parodyta, kad homogeninė aukštadažnė stimuliacija efektyviai valdo impulso plotį ir greitį, o didelio intensyvumo stimuliacija gali ir sustabdyti impulso sklidimą. Tačiau mielinuoto aksono atveju, mažo intensyvumo aukštadažnė stimuliacija gali pagerinti aksono pralaidumą impulsams. Toks sistemos elgesys nulemtas neurono sužadinimo priklausomybės nuo stimuliacijos parametro.

Trečiame disertacijos skyriuoje yra nagrinėjamas sujungtų osciliatorių sinchronizacijos valdymas. Pasiūlytas registracijos-stimuliacijos algoritmas, kurio veikimo principas pagrįstas trūkiu grįžtamuoju ryšiu. Šis algoritmas gali veikti sudėtingose situacijose, kai registruojamas signalas yra žymiai silpnesnis už signalą, kuriuo veikiama sistema. Šis atvejis yra būdingas neuroninėms sitemoms. Algoritmo veikimas paremtas periodiniu dviejų etapų kartojimu. Pirmame (registracijos) etape, sistema neveikiama, o jos generuojamas vidutinis laukas yra įrašomas į atminties elementą. Antro etapo (stimuliacijos) metu sistema veikiama signalu

proporcingu įrašytajam. Šių dviejų etapų periodinis kartojimas efektyviai panaikina sinchronizaciją. Nustatyta, kad registracijos-stimuliacijos algoritmo nekoherentinės būsenos stabilumo zonos grįžtamojo ryšio delsos τ ir stiprio P plokštumoje turi rezonansinę struktūrą. Šios zonos yra ties vertėmis $\tau = mT/2$, kur T yra charakteringas sistemos vidutinio lauko periodas, kai sistemos neveikia išorinė stimuliacija, o m yra neneigiamas sveikasis skaičius. Pristatytas patobulintas registracijos-stimuliacijos algoritmas, kuriuo įgyvendinama krūvio balanso sąlyga. Ši sąlyga nepanaikina stabilumo zonų rezonansinės struktūros (τ, P) plokštumoje, tačiau nustoja veikti mažų delsų riboje $\tau \to 0$. Algoritmo efektyvumas pademonstruotas analiziškai ir skaitmeniškai su globaliai sujungtais Stuart-Landau osciliatoriais, sinaptiškai sujungtais FitzHugh-Nagumo, o taip pat ir su Hodgkin-Huxley neuronais.

Ketvirtame skyriuje aptartas sinchronizacijos valdymas bistabiliuose tinkluose, kur esant tam tikriems parametrų rinkiniams egzistuoja stabili koherentinė ir nekoherentinė būsenos. Problema formuluojama tokiu būdu: tariame, kad sistema yra koherentinėje būsenoje, naudojant išorinę homogeninę perturbaciją reikia šią sistemą pervesti į stabilią nekoherentinę būseną. Spėjame, kad sinchronizacijos bistabilumas gali būti būdingas ir neuronų tinklams, kas paaiškintų tinklų elgseną esant normaliai žmogaus būsenai (nekoherentinė) ir epilepsijos priepuolio metu (koherentinė). Šiam tikslui buvo pritaikyti registacijos-stimuliacijos ir koordinuoto fazės postūmio metodai. Nustatyta, kad registracijos-stimuliacijos algoritmas efektyviai išveda globaliai sujungtų osciliatorių sistemą iš koherentinės į nekoherentinę būseną, o koordinuoto fazės postūmio metodas veikia ir bemastelinio tinklo topologijos atvejais.